2.14 Nanostructured Inorganic–Organic Hybrid Semiconductor Materials

J Li and R Zhang, Rutgers, The State University of New Jersey, Piscataway, NJ, USA

Abbreviations

aa	Amylamine
ba	*n*-Butylamine
bda	1,4-Butanediamine
CB	Conduction band
cha	Cyclohexylamine
DFT	Density functional theory
dien	Diethylenetriamine
ea	Ethylamine
en	Ethylenediamine
ha	*n*-Hexylamine
hda	1,6-Hexanediamine
hpda	1,7-Heptanediamine
LD	Laser diode
LDA	Local density-functional approximation
LED	Light-emitting diode
LT	Low temperature
ma	Methylamine
mxda	*m*-Xylylenediamine
NLO	Nonlinear optical
NTE	Negative thermal expansion
OD	Outside diameter
otda	1,8-Octanediamine
pa	*n*-Propylamine
pda	1,3-Propanediamine
PL	Photoluminescence
ptda	1,5-Pentanediamine
PTE	Positive thermal expansion
PXRD	Powder x-ray diffraction
QCE	Quantum confinement effect
QD	Quantum dot
RT	Room temperature
SXRD	Single-crystal x-ray diffraction
TEM	Transmission electron microscope
TGA	Thermogravimetric analyses
trien	Triethylenetetramine
VB	Valence band
W	Würtzite
ZB	Zinc blende
ZTE	Zero thermal expansion

2.14.1 Background and Introduction

Motivated by both fundamental science and the long-term technological applications, semiconductor materials and their devices have been the subjects of chemistry, physics, materials science, and industrial technology for decades. (see Chapter 4.04)[1–9] The birth of the modern microelectronics can be traced to the invention of the first transistor based on the germanium semiconductor by Shockley, Brattain, and Bardeen at Bell Laboratories in 1948.[10,11] This discovery led to a Nobel prize in physics awarded to them in 1956. The next major breakthrough is the integrated circuit (integrated monolithic silicon chip),[12] for which Jack Kilby, who invented it at Texas Instruments in 1958, received the Nobel prize in physics in 2000.

During the latter half of the twentieth century, numerous significant advances in information processing, energy exploitation, communication, manufacture, and consumer goods were made as a direct result of semiconductor-based digital electronics.[2,13–18] Today, semiconductor devices and technologies are penetrating every aspect of our lives. From telegram to cell phones, from Nintendo to personal computers, semiconductors contribute ubiquitously to the human world and achieve a status that perhaps no other materials have ever reached. To enhance functionality and reduce energy consumption, the recent development of semiconductor devices focuses extensively on the miniaturization of the device scale.[19–23] During the past decades, millimeter- or micrometer-sized semiconductor devices have evolved into the nanometer scale. For example, transistor gate lengths can reach as low as 25 nm on a nominally 32-nm process (an advanced lithographic node used in volume complementary metal–oxide–semiconductor (CMOS) fabrication) by 2010.[24,25] As the demands for high-efficiency and low-cost devices continue to grow, semiconductor materials will have to meet more stringent requirements such as suitable particle size and morpho-logy, high crystallinity and phase purity, good processability, and better performance. A potentially far greater market in the areas of information technology, biotech, green energy, and environmental protection industries awaits the new generation of semiconductor materials that are capable of overcoming existing challenges.[26–29] Therefore, the development of new and high-performance semiconductor materials is one of the most important aspects for future generations of advanced electronic and optoelectronic devices.

2.14.1.1 Binary Semiconductor Compounds of Group VI Elements

Binary semiconductor compounds based on elements from groups II (group 12) and VI (group 16), III (group 13) and VI, IV (group 14) and VI, as well as V (group 15) and VI have received considerable attention since the 1950s (see Chapters 1.32; 2.10; 5.09; 4.09).[30] These materials have found a wide variety of applications in optical devices (II–VI), solar cells (II–VI and III–VI), infrared detectors (IV–VI), and room-temperature thermoelectric generators (V–VI), to name a few. Further, they make a significant impact on our everyday lives, such as optical fiber communications, compact disk players, satellite TV receivers, barcode readers, and full-color advertising displays.

The II–VI binary compounds belong to one of the most important classes of semiconductor materials. They are formed between the elements of group IIB (Zn, Cd, and Hg) and group VIA (O, S, Se, and Te). Sometimes, group IIA elements and the transition element Mn are also considered as group II metals. There are two crystal structure types dominating in II–VI semiconductors: zinc blende and würtzite. Apart from these two, other structures such as rock salt, orthorhombic, and trigonal types are also found in several II–VI compounds (Table 1). Since most II–VI binary compounds are direct bandgap semiconductors, the transition probabilities for optical absorption and emission are relatively large for these materials.

As wide bandgap II–VI semiconductors, ZnO, ZnS, and CdS are suitable for use in photonic, optical, and optoelectronic devices.[8,31–41] For example, ZnO, ZnS, and their composite structures are unique candidates for ultraviolet (UV) light lasers and detectors working in the wavelength range of 320–400 nm,[42] which is naturally accessible at the Earth's surface. In addition, ZnO has been assembled into nanometer-scale field emitters with a remarkably high performance.[43–45] Other II–VI semiconductors such as CdSe, CdTe, and ZnTe have been used in photovoltaic (PV) devices.[7,46–48] For example, CdTe, with a direct bandgap of 1.5 eV, possesses high absorption coefficient and energy radiation resistance.[49,50] These exceptional properties make CdTe an excellent candidate for solar cells. Narrow bandgap II–VI semiconductors HgSe and HgTe are classified as semi-metals as their conduction and valence bands overlap. They are utilized in a range of applications, including high-efficiency infrared sensing and gamma-ray detection.[51–53]

The binary combinations of a group III element (Ga, In, and Tl) and a group VI chalcogen (S, Se, and Te) exhibit great diversity, and many different stoichiometries have been observed (Table 1). Because the trivalent group III element is overstoichiometric, III–VI compounds contain ordered or disordered vacancies and thus can be considered as ternary structures (III-□-VI) in which the vacancies (□) are regarded as virtual atoms with zero valence. Structural types found for III–VI binary compounds (with the stoichiometry of M_2Q_3) include: (1) defect würtzite structure (with ordered or disordered vacancies); (2) defect zinc blende structure (with ordered or disordered vacancies); (3) defect spinel structure; and (4) layered structure.[30,54] For III_2–VI_3 structures with the ordered vacancies, every atom is located at the würtzite or the zinc blende site and one-third of the cation sites are occupied by the vacancies.

III–VI semiconductors are direct-gap semiconductors similar to the II–VI compounds; however, their polytypism and variety of stoichiometry are not found in the II–VI binaries. During the past decades, III–VI semiconductors have attracted a great deal of research attention because of their unique structural, optical, and electrical properties, which result in applications including lithium ion batteries,[55,56] photovoltaics,[57,58] phase-change memory,[59,60] and optoelectronic devices.[61,62]

For example, as an n-type semiconductor material, In_2S_3 meets the requirement as window material or buffer layer for PV structures,[63–66] and its bandgap can be tuned between 2.0 and 2.45 eV by varying the material composition. In addition, the In defects inherent in In_2S_3 allow it to serve as a host for metal ions to form III–VI diluted magnetic materials.[67] In_2Se_3

Table 1 Crystal structures of selected group VI binary semiconductors

II–VI		*III–VI*		*IV–VI*		*V–VI*	
Compound	*Structure*	*Compound*	*Structure*	*Compound*	*Structure*	*Compound*	*Structure*
ZnO	Würtzite	α-Ga_2S_3	Ordered vacancies, würtzite type	GeO_2	Rutile	As_2O_3	Cubic arsenolite, claudetite I/II
ZnS	Würtzite/zinc blende	β-Ga_2S_3	Disordered vacancies, würtzite type	GeS GeS2	GeS type monoclinic	As_2S_3	Orpiment
ZnSe	Zinc blende	γ-Ga_2S_3	Disordered vacancies, zinc blende type	GeSe $GeSe_2$	GeS type orthorhombic	As_2Se_3	Orpiment
ZnTe	Würtzite/zinc blende	α-Ga_2Se_3	Disordered vacancies, zinc blende type	GeTe	Rock salt (slightly distorted)	As_2Te_3	Monoclinic
CdO	Rock salt	β-Ga_2Se_3	Ordered vacancies, zinc blende type	SnO_2	Rutile	Sb_2S_3	Orthorhombic
CdS	Würtzite	Ga_2Te_3	Disordered vacancies, zinc blende type	SnS SnS_2	GeS type CdI_2 type	Sb_2Se_3	Orthorhombic
CdSe	Würtzite/zinc blende	α-In_2S_3	Disordered defect spinel	SnSe $SnSe_2$	GeS type CdI_2 type	Sb_2Te_3	Tetradymite
CdTe	Zinc blende	β-In_2S_3	Ordered defect spinel	SnTe	Rock salt (slightly distorted)	α-Bi_2O_3	Monoclinic
HgO	Orthorhombic	γ-In_2S_3	Layered structure	PbO PbO_2	Tetragonal rutile	β-Bi_2O_3	Tetragonal
HgS	Trigonal/zinc blende	α-In_2Te_3	Ordered vacancies, zinc blende type	PbS	Rock salt	Bi_2S_3	Orthorhombic
HgSe	Zinc blende	β-In_2Te_3	Disordered vacancies, zinc blende type	PbSe	Rock salt	Bi_2Se_3	Tetradymite
HgTe	Zinc blende			PbTe	Rock salt	Bi_2Te_3	Tetradymite

is another important member of this family. It is particularly suitable for photovoltaic applications because of its appropriate bandgap (1.3 eV) and good transport properties.[68,69] Cui et al. have observed an interesting metal-to-insulator transition in In_2Se_3 nanowires, which correlates with a fourfold superlattice-to-normal-lattice transition induced by additional In vacancies.[70] Among all the III–VI compounds, In_2Te_3 possesses the smallest direct bandgap ($\sim$1.0 eV).[54] It has been investigated for potential applications in thermoelectric power generators, gas sensors, strain gauges, and switching memory elements.[71–76] In_2Te_3 has two crystalline phases. The high-temperature phase (above 523 K) is disordered β-In_2Te_3, a defect zinc blende structure with a lattice parameter of 6.16 Å. The low-temperature phase (α-In_2Te_3) has ordered vacancies (zinc blende type) with a lattice parameter of 18.54 Å.

The III–VI semiconductors with the stoichiometry of MQ (such as GaSe, InSe, GaTe, and GaS) have also received considerable interest because of their remarkable nonlinear optical properties.[77–80]

Among group IV elements, Si and Ge represent the two most technologically relevant elemental semiconductors, while Sn and Pb form a wide range of binary semiconductor materials when combined with group VI chalcogens (Table 1).[30] The chemistry and crystal structures of IV–VI binary semiconductors have an added complexity as group IV elements may all be found in either the +2 or the +4 oxidation state. SnS, SnSe, GeS, and GeSe possess an orthorhombic layered crystal structure (so-called GeS-type structure), which may be considered as a distorted rock-salt structure. The lead salts (PbS, PbSe, and PbTe) crystallize in the rock-salt structure with Pb atoms occupying the cation sites and chalcogens forming the anionic lattice. The structure of GeTe and SnTe is similar to rock salt, with slight deformations due to the phase transitions. The IV–VI compounds with the stoichiometry of MQ_2 (i.e., +4 oxidation state for group IV elements) also exhibit a variety of structural types (see Table 1 for details).

The IV–VI semiconductors have long been of interest primarily for two reasons. One is that these materials are narrow bandgap semiconductors or semimetals with excellent thermoelectric and bolometric properties.[81,82] The second is that their heats of formation are small, reflecting the weak ionicity. Therefore, the IV–VI semiconductors are easily transformed between crystalline and glassy states.[83,84] Because the small and reversible structure changes will significantly influence the conductivity, these materials can be used as phase-transition memory[85,86]: the crystal state is metallic while the glass is semiconducting.

As an exemplar of IV–VI semiconductors, SnS possesses both an indirect and a direct bandgap (1.09 and 1.3 eV, respectively).[87] The direct bandgap, being very close to that of silicon, is located in the desired spectral region of materials with high efficiency for the collection of solar radiation. The absorption coefficient of SnS is $\sim 10^4$ cm^{-1}, sufficiently high to allow light absorption occurring at very thin layer of the absorber.[88] Moreover, the component elements of SnS are earth-abundant and low cost, chemically stable, and nontoxic. Therefore, SnS meets almost all the requirements for an efficient photovoltaic (PV) absorber, which makes it a unique candidate for PV and other optoelectronic applications.[89–91]

Binary lead chalcogenides (PbS, PbSe, and PbTe) have a great potential for their utility in opto devices as optically active components in the near-infrared (NIR) and IR spectral regions.[92–94] These materials are therefore beneficial to IR applications such as long-wavelength sensors, IR communication

relays, etc. Notably, the bandgaps of lead chalcogenides have negative pressure coefficients[95]; that is, they decrease with increase in pressure, in contrast to what is observed in III–V and II–VI semiconductors. PbSe and PbTe also serve as examples where the minimum energy gap increases as the atomic number of the anion increases. In addition, PbTe is a premier thermoelectric material for midrange temperature (600–800 K) applications.[96–98] A bandgap of 0.32 eV makes it suitable for power-generation applications and for either n- or p-type doping with appropriate dopants. The maximum *ZT* value for PbTe has been reported to be 0.8–1.0 (~650 K).[99]

As another important group of semiconductor materials, the V–VI binary system is formed between the elements of group V (As, Sb, and Bi) and group VI (O, S, Se, and Te) from the periodic table. As shown in **Table 1**, V–VI binary semiconductors crystallize in a great diversity of structure types.[30,54] For As_2O_3, a low-temperature phase (i.e., cubic arsenolite) and two high-temperature phases (i.e., claudetite I and II) have been found. Bi_2O_3 exists in several polymorphic forms at room temperature; two representative phases are monoclinic α-phase and tetragonal β-phase. Both As_2S_3 and As_2Se_3 possess orpiment structure, while As_2Te_3 crystallizes in a distinct monoclinic structure. The compounds of Sb_2S_3, Sb_2Se_3, and Bi_2S_3 are nearly isomorphous and their lattices adopt an orthorhombic space group. In addition, Sb_2Te_3, Bi_2Se_3, and Bi_2Te_3 structures are tetradymite type with a space group of R-3*m*, and the term 'tetradymite' refers to the mineral of Bi_2Te_2S.

The V–VI materials (especially for Sb_2Te_3 and Bi_2Te_3) as well as their alloys are well known for their low-temperature thermoelectric properties.[100–105] They have been used in conventional thermoelectric generators and coolers. As a prototypical thermoelectric system, Bi_2Te_3 has a narrow and indirect bandgap of ~0.15 eV. The state-of-the-art thermoelectric materials based on Bi_2Te_3 are synthesized by alloying with Sb for p-type and Se for n-type materials.[106] The highest *ZT* value for a bulk p-type Bi_2Te_3 material was reported in 2008. The material with $ZT = \sim 1.4$ at 100 °C was prepared by ball milling followed by direct-current hot pressing.[107]

Very recently, research interest in V–VI semiconductors has led to an additional impetus from a totally different direction. It has been proposed and then discovered that stacks of quasi-2D layers of Bi_2Te_3 are members of a new type of materials referred to as topological insulators.[108–110] The surface state of quasi-2D layers of Bi_2Te_3 is predicted to consist of a single Dirac cone. Besides Bi_2Te_3, it has been shown that other V–VI structures such as Bi_2Se_3 and Sb_2Te_3 are also topological insulators.[111] The particles in topological insulators coated with thin ferromagnetic layers have manifested exotic physic phenomena and were proposed for possible applications in the magnetic memory where read and write operations are achieved by purely electric means.[110]

2.14.1.2 Semiconductor Quantum Dots and Quantum Size Confinement

The bandgap, which separates the conduction and valence band, is an important property of semiconductor materials (see **Chapter 4.08**). The width of the bandgap is fixed in a bulk semiconductor, namely, it is only determined by the inherent properties of the material itself. In such a case, an electron–hole pair in the semiconductor is typically bound within a characteristic length, called the Bohr radius of the electron–hole pair or exciton.[30] As the particle size of the semiconductor material decreases below the Bohr radius (e.g., <10 nm), atomic-like discrete energy levels are formed and the electrons or holes are confined in one, two, or three spatial dimension(s). This is because there are no sufficient atoms to form the continuous energy levels that are characteristic of the filled and empty bands in bulk semiconductors. Therefore, the bandwidth as well as energy difference between the conduction and valence band will vary, and the extent of such variation will be determined by the number of atoms. As the particle size decreases, the bandgap will increase accordingly. This peculiar phenomenon is called the 'quantum confinement effect' (QCE) or 'quantum size effect,' which gives rise to a broad bandgap tunability and allows modification of semiconductor properties on a large scale.[112–114] Nanoscale materials that exhibit QCE are often referred to as quantum wells (confined in one dimension), quantum wires (confined in two dimensions), or quantum dots (QDs, confined in all three dimensions). QDs can be modeled as a particle-in-a-box system, where the QD is the 3D box and the excited electron with its hole counterpart is confined within the dot (sphere of radius *R*). This 3D-box model predicts that the size-dependent contribution to the bandgap of QDs is simply proportional to $1/R^2$.[115] Being zero dimensional, QDs have a sharper density of states than higher-dimensional structures, and thus possess narrow emission profiles and broad absorption bands, which give rise to superior physical properties that could potentially revolutionize the existing optical and optoelectronic technologies. Semiconductor QDs bridge the gap between molecules and bulk materials; however, the boundaries among molecules, quantum dots, and bulk regimes are not well defined and are material dependent.

Over the past decades, considerable research efforts have been devoted to develop semiconductor QDs due to their great potential for applications in solar cells,[116–124] quantum computation,[125–129] light-emitting diodes (LEDs),[130–135] lasers,[136–139] nonlinear optical devices,[140–146] and biological imaging.[117,147–150] The II–VI-based QDs exhibit some extraordinary optical properties such as size-dependent emission tunability, sharp and strong emission profile, high quantum yield, and good photostability.[151] The emission wavelength of II–VI QDs can be finely tuned from the UV to the NIR region through systematic control of particle size during the synthesis. This enables II–VI QDs to be potentially useful as a new type of fluorescent tag for biomedical research, clinical diagnostics, drug delivery, and photodynamic therapy.[147,152,153] Notably, a recent discovery showed that ultra-small CdSe colloidal QDs can emit white light directly,[154] which makes it possible to avoid unfavorable drawbacks associated with the current white light-generation processes (e.g., use of multiple phosphors and complex mixing and doping procedures). The broad emission profile of the CdSe QDs can be attributed to the large number of midgap surface sites generated by their high surface-to-volume ratio.[155] Furthermore, ZnSe QDs are considered to be a leading candidate for the blue LED,[156] which is a basic component of full-color electroluminescent displays and one of the three prime components for white-light LEDs. ZnSe QDs are also promising for the application as laser

diodes (LDs),[156,157] which emit blue light at 405 nm and allow a considerable increase of the storage density of compact disks.

2.14.1.3 Crystalline Inorganic–Organic Hybrid Semiconductor Materials

The earliest development of 'primitive' inorganic–organic hybrid materials can be traced back to centuries. In order to make colorful and bright paints, ancient people put tremendous effort into producing new admixtures of dyes, inorganic pigments, and other inorganic–organic natural materials. This kind of crude admixtures is virtually the origin of the inorganic–organic hybrid materials.[158] It was not until the last century when the refined analytical techniques replaced the 'trial and error' tradition and the modern science allowed the deep understanding of the true nature of matter; research on inorganic–organic hybrid materials becomes a quickly expanding frontier for both fundamental science and practical utility. Because the combination of inorganic and organic components may lead to unique properties that are impossible by either component alone, successful production of such hybrid materials by either a 'top-down' or a 'bottom-up' approach will bring to reality the development of new generations of functional materials at the molecular level.

As a broadly defined and interpreted term, 'inorganic–organic hybrid materials' can refer to a vast variety of different material systems. Therefore, we herein limit our discussions to the family of crystalline inorganic–organic hybrid semiconductor materials. These hybrid semiconductors possess a perfectly ordered crystal lattice and consist of standalone inorganic and organic modules blended at the atomic or the molecular level. Based on the interactions between inorganic and organic moieties, crystalline hybrid semiconductors can be classified into two categories: (1) those with strong chemical interactions (e.g., covalent and coordinative bonds) and (2) those with weak interactions (e.g., van der Waals interactions, hydrogen bonds, and weak electrostatic force).

Crystalline hybrid semiconductors are materials of both fundamental and technological importance. This is because they integrate the diverse functionality of inorganic semiconductors (such as optical, electronic, magnetic, thermal, and mechanical properties) and the advantages of organic species (such as structural flexibility, lightweight, easy processability, and low cost) into a single-crystal lattice.[159–168] One of the major advantages of such a combination/incorporation is the high tunability of material properties. Therefore, it is possible to include more than one function into a semiconductor by simply incorporating the appropriate module with the desired property into its crystal lattice. However, though the crystalline hybrids are highly desirable, only a limited number of systems have been reported up to now. Perovskite-based inorganic–organic hybrid semiconductors serve as a good example.[159,169–172] The interactions between inorganic and organic components in perovskite hybrids are primarily ionic, accompanied also with relatively weak H-bonds or van der Waals forces in some cases. Some interesting optical, electrical, and magnetic properties have been discovered in these materials.[159,173–189] Particularly, the perovskite hybrids with layered structures afford a good platform for the investigation of 2D quantum well systems.[180,190–192]

2.14.1.4 Nanostructured Crystals and Structure-Induced QCE

Despite great success in the development of nanoscale materials, synthesis of strongly correlated and single-sized nanomaterials with periodically ordered lattices remains an enormous challenge. The need for fabricating such nanomaterials becomes especially apparent when taking a close look at semiconductor colloidal QDs.[193–198] These remarkable tiny particles exhibit a very strong size-induced QCE because they can be made very small ($\sim$1 nm). Therefore, they are highly capable of tuning bandgaps and other related semiconductor properties. However, there are some major problems that limit their use in optoelectronic devices. One of them is the size control issue; even for the best-grown dots there is always a size distribution. Another difficulty is to arrange them uniformly because correlations among these dots are very weak. These issues are very undesirable for optical applications that require high intensity and a sharp line width. In addition, passivation by organic molecules to prevent them from aggregation further reduces the correlation among the dots and severely limits their applications in optoelectronic devices that require high transport properties (e.g., conductivity and carrier mobility) such as solar cells, LEDs, thermoelectrics, and transistors.

To address the specific problems of colloidal QDs, while maintaining excellent bandgap tunability, an unprecedented family of crystalline nanostructured inorganic–organic hybrid semiconductors based on II–VI binary compounds has been developed in the last decade.[199–206] This family of materials possesses perfectly ordered crystalline lattices, and the inorganic and organic components are interconnected via strong coordinative/covalent bonds. In these hybrid structures, the inorganic moieties are virtually the sub-nanometer-sized building units of II–VI binary semiconductors, while the organic linkers or spacers (e.g., mono/di-amine molecules) serve as structure-directing and passivating agents. Through the rational control of the composition and the dimensionality of inorganic modules, as well as variation of organic spacers, more than 100 members for this family with a variety of different crystal structures such as 1D chains, 2D layers, and 3D networks are synthesized.

Remarkably, most members of this hybrid family exhibit a very strong structure-induced QCE, which is a unique property pertinent to their special structural characteristics. This kind of structure-induced QCE is originated from the modular nature of perfectly ordered inorganic and organic moieties at nanometer or sub-nanometer scale, quite different from the aforementioned size-induced QCE found in colloidal QDs. As in the case of colloidal QDs, insulating organic amine molecules in nanostructured crystalline hybrids also serve as passivating agents to prevent interactions between the neighboring inorganic motifs. The main difference is that in the hybrid structures the organic molecules direct the inorganic motifs into a perfectly ordered (periodical) array in the form of macroscopic crystals. Such nanostructured arrays can well be considered as perfectly ordered crystalline quantum well (the crystal structure containing 2D MQ layers), quantum wire (the crystal structure containing 1D MQ chains), or QD (the crystal structure containing 0D MQ clusters). As a result, the strong QCE observed in these hybrids must be attributed to their structure, rather

than the physical dimension of the particles. It is noted that such QCE leads to a large blue shift (i.e., shifting to higher energy) in their absorption spectra and, consequently, a huge increase in their bandgaps. The extent of such increase (~2 eV) is significantly greater than what has been achieved by the smallest colloidal QDs reported to date (~1 eV).[154,207–210]

The nanostructured crystalline hybrids are free of several critical issues haunting in the synthesis of the colloidal QDs such as post-synthesis purification, particle size and morphology control, particle dispersity, lattice stoichiometry (i.e., problems with lattices altered by the defects such as excess atoms, alloying additions, or vacancies), local oxygen concentrations, etc. A more daunting issue for the colloidal QDs is the weak correlation between the dots, which will lead, inevitably, to low conductivity and poor carrier mobility, severely limiting their potential applications for optoelectronic devices. Conversely, because the nanostructured crystalline hybrids comprise perfectly ordered and extended inorganic networks (e.g., infinite 1D chains, and 2D layers) very similar to their parent semiconductors, the strong carrier correlations in one or two directions will be ensured in these materials. More importantly, the bandgap and other physical properties can be readily tuned by varying the composition and dimensionality of inorganic motifs as well as modifying the overall crystal structure. In addition, the incorporation of inorganic motifs and organic molecules into a single-crystal lattice also gives rise to an enhancement of material functionality, due to the combination of multiple properties originated from individual constituent, as well as new features and phenomena that are not possible with the individual component alone.

2.14.2 II–VI-Based Inorganic–Organic Hybrid Semiconductor Nanostructures

2.14.2.1 Design, Synthesis, and Crystal Growth

Conceptually different from the common way to tune the semiconductor properties (i.e., reducing the size of bulk particles), the design strategy applied here is to build semiconductor nanostructures within macroscopic crystals. In doing so, the quantum confinement will occur within the internal crystal structure, rather than by varying the physical dimension of the particles. This is accomplished by incorporating neutral amine molecules into the II–VI crystal lattice, and the resultant structure will be periodically ordered arrays consisting of sub-nanometer-sized II–VI fragments either interconnected or separated by amine molecules. These sub-nanometer-sized II–VI fragments (i.e., infinite 2D layers or 1D chains of thickness <10 Å) can be virtually regarded as building units (like 'slice' or 'wire') cut from the II–VI parent crystal lattices with very little perturbation in their structure, composition, bonding, and charge. In such a way, the semiconductor properties of inorganic II–VI compounds are expected to be preserved in the resultant hybrid materials, with inorganic II–VI components serving as the source of semiconductor properties and organic molecules as confining agents and structure-directing species. As a general formula, $[MQ(L)_x]$ (M = Zn, Cd, Mn; Q = S, Se, Te; L = amine molecules; $x = 0.5$, 1, 2) is used to designate the family of II–VI based inorganic–organic hybrid semiconductors.

The first attempt at making inorganic–organic hybrid materials built on II/VI elements was made by Rao et al. in 1998.[211] In their work, nanoscaled cadmium chalcogenides were synthesized via solution routes by employing long-chain amines as amphiphiles. However, the crystal structures of these composite materials were unable to be determined and only the compositions were identified by energy-dispersive x-ray spectroscopy, thermogravimetric analysis (TGA), and transmission electron microscope (TEM) techniques.

In 2000, the first three ZnTe-based inorganic–organic hybrid semiconductors in single-crystal form were successfully synthesized by us.[199] The formulae of these three compounds are 3D-α-$[ZnTe(en)_{0.5}]$, 3D-β-$[ZnTe(en)_{0.5}]$, and 3D-α-$[ZnTe(pda)_{0.5}]$, and their crystal structures were fully solved. Since then, we have synthesized and structurally characterized a large number of members of this unique family.

As one of the most effective crystal growth techniques, the solvothermal (or hydrothermal) synthesis has found tremendously broad usage in both synthetic chemistry and industrial engineering (see **Chapter 4.01**).[212–227] By employing this technique, a large number of solids such as metal chalcogenides,[217,227–230] metal nitrides,[227,231–234] metal phosphides,[235–243] and metastable phases[234,244–250] have been produced to date. The utility of solvothermal (or hydrothermal) reactions in a variety of areas has been described in a number of reviews.[212,216,220,240,244,245,251–257] Under solvothermal conditions, the reaction takes place in a closed system at elevated temperature and pressure (often in the vicinity of its critical point). The properties of the solvent, such as solubility, viscosity, density, and polarity, will behave very differently from how they act under ambient conditions.[220,258] These changes can enhance the solubility and chemical reactivity of reactants and, consequently, enable the reactions to take place under much milder conditions.

The solvothermal synthesis is proven to be the most effective approach for the preparation and crystal growth of II–VI hybrid materials. Most reactions are carried out in sealed acid-digestion bombs or Pyrex tubes of different volumes. In most cases, metal salts and elemental chalcogens are used as M^{2+} and Q^{2-} source. Elemental metal powders and alkali metal chalcogenides compounds (A_2Q, A = Li, Na, K; Q = S, Se, Te) are also employed in some cases. The difference in metal and chalcogen sources has an essential impact on the purity, crystallinity, and morphology of the hybrid products, and in some cases, they can affect the structure type of the material. A representative example is the crystal growth of 3D-α-$[ZnTe(en)_{0.5}]$ and 3D-β-$[ZnTe(en)_{0.5}]$; by using different zinc salts (i.e., $ZnCl_2$ and $Zn(NO_3)_2 \cdot 6H_2O$), two types of ZnTe-based 3D structures (i.e., α and β phases) can be selectively synthesized under the same solvothermal conditions.

Organic amine molecules of low melting points are employed as solvents in the synthesis of the II–VI hybrids. These include alkyl monoamines (with number of carbon atoms ranging from 1 to 6), alkyl-diamines (with number of carbon atoms ranging from 0 to 9), and several cyclic amines (such as cyclohexylamine,[259,260] *m*-xylylenediamine,[261] and piperazine[262]). The physical properties of selected amine molecules are summarized in **Table 2**. All organic amines have dual functionality in the synthesis of these hybrid compounds. They serve not only as solvents but also as reactants (spacers). They

Table 2 Physical properties of selected amine molecules[263]

Amine molecule	*Formula*	*F.W. (g mol^{-1})*	*Density (g cm^{-3})*	*mp (°C)*	*bp (°C)*	*Abbrev.*
Hydrazine anhydrous	H_2NNH_2	32.05	1.021	1.4	113.5	N_2H_4
Hydrazine monohydrate	$H_2NNH_2 \cdot H_2O$	50.06	1.027	−52	120–121	$N_2H_4 \cdot H_2O$
Methylamine (40% aq.)	CH_3NH_2	31.06	0.904	−38	48	ma
Ethylamine (70% aq.)	$CH_3CH_2NH_2$	45.08	0.803	−81	38	ea
n-Propylamine	$CH_3(CH_2)_2NH_2$	59.11	0.719	−83	48–49	pa
n-Butylamine	$CH_3(CH_2)_3NH_2$	73.14	0.738	−50	76–78	ba
Amylamine	$CH_3(CH_2)_4NH_2$	87.17	0.752	−50	104	aa
n-Hexylamine	$CH_3(CH_2)_5NH_2$	101.19	0.766	−19	130–131	ha
Octylamine	$CH_3(CH_2)_7NH_2$	129.25	0.780	−1	178–179	oa
Decylamine	$CH_3(CH_2)_9NH_2$	157.29	0.787	12–15	216–218	da
Dodecylamine	$CH_3(CH_2)_{11}NH_2$	185.36	0.802	27–31	247–249	dda
Cetylamine	$CH_3(CH_2)_{15}NH_2$	241.46	0.813	42–44	330	cta
Stearylamine	$CH_3(CH_2)_{17}NH_2$	269.52	0.862	53–55	349	sa
Cyclohexylamine	$(CH_2)_5CHNH_2$	99.18	0.868	−18	133–134	cha
Ethylenediamine	$H_2N(CH_2)_2NH_2$	60.10	0.899	8–11	117–118	en
1,3-Propanediamine	$H_2N(CH_2)_3NH_2$	74.13	0.888	−12	140	pda
1,4-Butanediamine	$H_2N(CH_2)_4NH_2$	88.15	0.877	27–28	158–160	bda
1,5-Pentanediamine	$H_2N(CH_2)_5NH_2$	102.18	0.873	9	178-180	ptda
1,6-Hexanediamine	$H_2N(CH_2)_6NH_2$	116.21	0.840	39–43	204–205	hda
1,7-Heptanediamine	$H_2N(CH_2)_7NH_2$	130.23	0.860	27–29	223–225	hpda
1,8-Octanediamine	$H_2N(CH_2)_8NH_2$	144.26	0.858	50–54	225–226	octa
m-Xylylenediamine	$C_6H_4(CH_3NH_2)_2$	136.19	1.03	14	274	mxda
Diethylenetriamine	$(NH_2CH_2CH_2)_2NH$	103.17	0.952	−40	200–204	dien

are thus referred to as 'reactive' solvents. In some cases, mixed solvents are also employed to facilitate the formation of targeted II–VI hybrids. For instance, 3D-[CdTe(en)$_{0.5}$] was obtained in a mixture solvent of en and hydrazine; 3D-α-[ZnTe(N_2H_4)$_{0.5}$] was formed in the solvent containing hydrazine and ma.

In some cases, desired hybrid materials in pure phase can only be prepared within a certain range of temperature. For example, 3D-[ZnTe(L)$_{0.5}$] hybrids can be prepared at relatively high temperatures (190–200 °C) while 3D-[ZnSe(L)$_{0.5}$] are obtained at 100–200°C. In addition, by adjusting the reaction temperature, 2D-[MQ(L)] and 2D-[M_2Q_2(L)] could be selectively synthesized. Another noticeable trend is that higher temperatures are required as the chalcogen element changes from S, Se, to Te. These results show that reaction temperature plays a critical role in the formation of final products.

By appropriate control of solvothermal conditions, single-phased II–VI hybrids can be successfully synthesized, and their crystal structures can be tuned systematically (e.g., from 1D, 2D, to 3D structures). Typical solvothermal reaction conditions for II–VI hybrids are listed in Table 3, which shows that hybrid structures of most of the II–VI binary compounds (e.g., ZnS, ZnSe, ZnTe, CdS, CdSe, CdTe, and MnSe) have been obtained. Among them, ZnTe- and MnSe-based hybrids can be grown into single crystals with fairly large sizes; additionally, the single crystals of [CdSe(en)$_{0.5}$] are also obtained. The remaining hybrid compounds are all generated in powder form and the Cd-based hybrid phases exhibit lower crystallinity than Zn-based phases.

In addition to a vast majority of II–VI hybrid compounds synthesized and structurally characterized by us, several 1D and 3D structures are recently reported by others adopting similar synthesis routes. These include 3D-α-[ZnS(en)$_{0.5}$],[229,264] 3D-[CdSe(en)$_{0.5}$],[265] 3D-[CdSe(hda)$_{0.5}$],[266] 1D-α(β)-[ZnTe(N_2H_4)$_2$],[267] and 3D-α-[ZnSe(mxda)$_{0.5}$].[261] A number of II–VI hybrid compounds, such as 1D-α-[ZnTe(N_2H_4)$_2$], 1D-[ZnSe(pda)], and 3D-[CdS(pda)$_{0.5}$], can also be prepared by solution reactions under ambient conditions. These hybrids as well as the synthetic conditions are summarized in Table 4. From this table, we see that all solution reactions involve hydrazine, which acts both as a solvent and a structure-directing agent. Some hybrid compounds (e.g., 3D-[CdSe(pda)$_{0.5}$]) can be prepared by both the solvothermal and the solution growth method. Another type of reaction to produce hybrid phases is via exchange of organic components. A good example is the solvothermal reaction of 2D-[ZnSe(pa)] with ba, which yielded 2D-[ZnSe(ba)] in pure polycrystalline form.

2.14.2.2 Crystal Structures

All crystal structures of the II–VI hybrid compounds that can be grown into suitable single crystals are determined by the single crystal x-ray diffraction (SXRD) method. ZnTe- and MnSe-based hybrid compounds as well as 3D-[CdSe(en)$_{0.5}$] are included in this category. All other II–VI hybrid compounds are in polycrystalline (powder) form, and their structures are characterized by the powder x-ray diffraction (PXRD). Based on the PXRD data, crystal structures of some selected compounds, that is, 3D-α-[ZnSe(L)$_{0.5}$] (L = en, pda, bda, hda, dien, mxda), 3D-[CdSe(L)$_{0.5}$] (L = pda, hda), 3D-α-[ZnS(en)$_{0.5}$], 2D-α-[ZnSe(ba)], and 2D-[Zn_2Se_2(ba)], are also refined and solved by the Rietveld method. Crystal structures of the remaining hybrids are identified by comparing their PXRD patterns with those of the known structures, and their unit-cell parameters are obtained by indexing of PXRD patterns. Crystal data of these II–VI hybrid compounds are listed in Table 5.

Table 3 Solvothermal synthesis of II–VI hybrid semiconductors

Compound	*Starting materials*[a]	*Solvents*	*Temp (°C)*	*Time (day)*
1D-[ZnTe(pda)]	$ZnCl_2 + Te$ (2:1)	$pda + N_2H_4$	70	10
2D-[$ZnSe(N_2H_4)$]	Zn + Se (1:1)	N_2H_4	110	1
2D-[$ZnTe(N_2H_4)$]	$Zn(NO_3)_2{\cdot}6H_2O + Te$ (1:1)	N_2H_4	110	2
2D-[ZnS(ma)]	$ZnCl_2 + S$ (2:1)	ma	65	7
2D-[ZnS(pa)]	$ZnCl_2 + S$ (3:1)	pa	60	3
2D-[ZnS(ba)]	$ZnCl_2 + S$ (2:1)	ba	65	7
2D-[ZnS(ha)]	$ZnCl_2 + S$ (2:1)	ma	65	7
2D-[ZnSe(ma)]	$ZnCl_2 + Se$ (2:1)	ma	130	7
2D-[ZnSe(ea)]	$ZnCl_2 + Se$ (2:1)	ea	120	8
2D-[ZnSe(pa)]	$ZnCl_2 + Se$ (2:1)	pa	150	2
2D-[ZnSe(ba)]	$ZnCl_2 + Se$ (2:1)	ba	140	7
2D-[ZnSe(ha)]	$Zn(ClO_4)_2{\cdot}6H_2O + Se$ (2:1)	ha	140	3
2D-[ZnTe(ma)]	$ZnCl_2 + Te$ (2:1)	ma	160	7
2D-[Zn_2S_2(ea)]	$ZnCl_2 + CS_2$ (2:1)	ea	60	5
2D-[Zn_2S_2(pa)]	$Zn(NO_3)_2{\cdot}6H_2O + S$ (2:1)	pa	110	5
2D-[Zn_2S_2(ba)]	$ZnCl_2 + S$ (2:1)	ba	120	6
2D-[Zn_2S_2(ha)]	$ZnCl_2 + S$ (2:1)	ha	120	2
2D-[Zn_2Se_2(ea)]	$Zn(NO_3)_2{\cdot}6H_2O + Se$ (4:1)	ea	150	6
2D-[Zn_2Se_2(pa)]	$Zn(NO_3)_2{\cdot}6H_2O + Se$ (2:1)	pa	140	5
2D-[Zn_2Se_2(ba)]	$ZnF_2 + Se$ (2:1)	ba	150	7
2D-[Zn_2Se_2(aa)]	$ZnCl_2 + Se$ (2:1)	aa	120	7
2D-[Zn_2Se_2(ha)]	$ZnCl_2 + Se$ (2:1)	ha	140	5
2D-[Cd_2S_2(pa)]	$CdCl_2 + S$ (2:1)	pa	80	3
2D-[Cd_2S_2(ba)]	$CdCl_2 + S$ (2:1)	ba	80	4
2D-[Cd_2S_2(ha)]	$CdCl_2 + S$ (2:1)	ha	50	3
2D-[Cd_2Se_2(pa)]	$Cd(NO_3)_2.4H_2O + Se$ (2:1)	pa	110	5
2D-[Cd_2Se_2(ba)]	$Cd(NO_3)_2.4H_2O + Se$ (1:1)	ba	110	5
2D-[Cd_2Se_2(ha)]	$Cd(NO_3)_2.4H_2O + Se$ (2:1)	ha	120	6
3D-α-[$ZnS(en)_{1/2}$]	$ZnCl_2 + S$ (2:1)	en	180	6
3D-[$ZnS(pda)_{1/2}$]	$ZnCl_2 + S$ (2:1)	pda	140	5
3D-[$ZnS(bda)_{1/2}$]	$ZnCO_3 + S$ (1.5:1)	bda	120	7
3D-[$ZnS(ptda)_{1/2}$]	$ZnCl_2 + S$ (2:1)	ptda	90	4
3D-[$ZnS(hda)_{1/2}$]	$ZnSO_4{\cdot}7H_2O + S$ (1:1)	hda	150	9
3D-[$ZnS(hpda)_{1/2}$]	$ZnCl_2 + S$ (2:1)	hpda	120	7
3D-[$ZnS(otda)_{1/2}$]	$ZnCl_2 + S$ (2:1)	otda	100	7
3D-[$ZnS(dien)_{1/2}$]	$ZnCl_2 + S$ (2:1)	dien	120	2
3D-α-[$ZnSe(en)_{1/2}$]	$ZnCl_2 + Se$ (2:1)	en	140	8
3D-α-[$ZnSe(pda)_{1/2}$]	$ZnCl_2 + Se$ (2:1)	pda	140	8
3D-α-[$ZnSe(bda)_{1/2}$]	$ZnCO_3 + Se$ (1:1)	bda	160	10
3D-α-[$ZnSe(ptda)_{1/2}$]	$ZnCl_2 + Se$ (2:1)	ptda	140	7
3D-α-[$ZnSe(hda)_{1/2}$]	$ZnSO_4{\cdot}7H_2O + Se$ (1:1)	hda	150	9
3D-α-[$ZnSe(hpda)_{1/2}$]	$ZnCl_2 + Se$ (2:1)	hpda	140	7
3D-α-[$ZnSe(dien)_{1/2}$]	$ZnCl_2 + Se$ (2:1)	dien	135	6
3D-α-[$ZnTe(N_2H_4)_{1/2}$]	$ZnO + Te$ (1:1)	$N_2H_4 + ma$	180	8
3D-α-[$ZnTe(en)_{1/2}$]	$ZnCl_2 + Te$ (2:1)	en	200	3
3D-β-[$ZnTe(en)_{1/2}$]	$Zn(NO_3)_2{\cdot}6H_2O + Te$ (2:1)	en	200	3
3D-α-[$ZnTe(pda)_{1/2}$]	$Zn(NO_3)_2{\cdot}6H_2O + Te$ (2:1)	pda	200	3
3D-α-[$ZnTe(bda)_{1/2}$]	$ZnF_2 + Te$ (2:1)	bda	200	4
3D-α-[$ZnTe(ptda)_{1/2}$]	$Zn(NO_3)_2{\cdot}6H_2O + Te$ (2:1)	ptda	210	7
3D-α-[$ZnTe(hda)_{1/2}$]	$ZnF_2 + Te$ (2:1)	hda	200	7
3D-δ-[$ZnTe(hda)_{1/2}$]	$ZnF_2 + Te$ (2:1)	hda	200	4
3D-[$CdS(en)_{1/2}$]	$CdCl_2 + S$ (1.5:1)	en	50	3
3D-[$CdS(bda)_{1/2}$]	$CdCl_2 + S$ (1:1)	bda	70	7
3D-[$CdS(ptda)_{1/2}$]	$CdCl_2 + S$ (2:1)	ptda	60	7
3D-[$CdS(hda)_{1/2}$]	$CdCl_2 + S$ (1:1)	ptda	60	7
3D-[$CdSe(en)_{1/2}$]	$CdCl_2 + Se$ (2:1)	en	130	8
3D-[$CdSe(pda)_{1/2}$]	$CdCl_2 + Se$ (2:1)	pda	130	8
3D-[$CdSe(bda)_{1/2}$]	$CdCl_2 + Se$ (2:1)	bda	120	7
3D-[$CdSe(ptda)_{1/2}$]	$CdCl_2 + Se$ (4:1)	ptda	120	7
3D-[$CdTe(en)_{1/2}$]	$Cd(NO_3)_2{\cdot}4H_2O + Te$ (2:1)	$N_2H_4 + en$	70	7

(*Continued*)

Table 3 (Continued)

Compound	*Starting materials*[a]	*Solvents*	*Temp (°C)*	*Time (day)*
3D-[CdTe(pda)$_{1/2}$]	$Cd(NO_3)_2{\cdot}4H_2O + Te$ (2:1)	N_2H_4 + pda	80	7
3D-[MnSe(en)$_{1/2}$]	$MnCl_2$ + Se (2:1)	en	160	7
3D-[MnSe(pda)$_{1/2}$]	$MnCl_2$ + Se (1:1)	pda	125	12
3D-[MnSe(bda)$_{1/2}$]	$(CH_3CO_2)_2Mn{\cdot}4H_2O$ + Se (1:1)	bda	160	10

[a]Molar ratio shown in parentheses.

Table 4 Solution-based sythesis of II–VI hybrid semiconductors

Compound	*Starting materials*	*Solvents*
1D-[ZnSe(pda)]	$Zn(NO_3)_2{\cdot}6H_2O$ + Se	N_2H_4 + pda
2D-[ZnSe(ma)]	$ZnCl_2$ + Se	$N_2H_4.H_2O$ + ma
2D-[ZnSe(ea)]	$Zn(NO_3)_2{\cdot}6H_2O$ + Se	N_2H_4 + ea
2D-[ZnSe(pa)]	$ZnCl_2$ + Se	$N_2H_4.H_2O$ + pa
2D-[ZnSe(ba)]	$ZnCl_2$ + Se	$N_2H_4.H_2O$ + ba
2D-[ZnSe(ha)]	$ZnCl_2$ + Se	$N_2H_4.H_2O$ + ha
3D-[ZnS(pda)$_{1/2}$]	$Zn(NO_3)_2{\cdot}6H_2O$ + Se	N_2H_4 + pda
3D-[ZnSe(pda)$_{1/2}$]	$ZnCl_2$ + Se	N_2H_4 + pda
3D-[CdS(en)$_{1/2}$]	$CdCl_2$ + Se	N_2H_4 + en
3D-[CdS(pda)$_{1/2}$]	Cd + S	N_2H_4 + pda
3D-[CdSe(pda)$_{1/2}$]	$CdCl_2$ + Se	N_2H_4 + pda

The bond lengths, inter-layer distances, layer thicknesses, and amine lengths of selected II–VI hybrids are listed in Tables 6 and 7, respectively.

According to the overall dimensionality as well as structural features of the inorganic components, the II–VI hybrid structures can be categorized into four types: the one-dimensional chain 1D-[MQ(L)], the two-dimensional single-layered 2D-[MQ(L)], the three-dimensional single-layered 3D-[MQ(L)$_{0.5}$] (containing acyclic or cyclic diamine molecules), and the two-dimensional double-layered 2D-[M_2Q_2(L)]. More detailed descriptions of these structures are provided in Sections 2.14.2.2.1–2.14.2.2.4.

2.14.2.2.1 The one-dimensional chain 1D-MQ(L) structures

The first 1D-MQ(L) structure 1D-[ZnTe(pda)] was reported by us in 2003.[204] In this compound, each Zn atom is tetrahedrally coordinated by two N atoms (from a chelating pda molecule) and two μ_2-Te atoms. Such a linkage affords a zigzag 1D $\{ZnTe\}_n$ chain propagated along the *b* axis (Figure 1) and it can be considered as a 'wire' cut from its parent structure (würtzite ZnTe) along the [0 0 1] direction. The overall packing structure of 1D-[ZnTe(pda)] is illustrated in Figure 1(b) viewing down the *b*-axis. As the 1D-[ZnSe(pda)] was made in powder form, only the unit cell parameters (Table 5) were indexed through its PXRD pattern, which is similar to that of 1D-[ZnTe(pda)] (Figure 2).

In 2005, Mitzi et al. reported two hydrazine-based 1D-[MQ(L)$_2$] structures, 1D-α-[ZnTe(N_2H_4)$_2$] and β-[ZnTe(N_2H_4)$_2$].[267] In these compounds, the tetrahedral geometry of each Zn site is defined by two N atoms (respectively from two monodentate hydrazine molecules) and two μ_2-Te atoms. The 1D chains in α-phase extend along the *a*-axis while in β-phase they run along the [1 0 −1] direction. These two phases are also differentiated by the Zn–Te bond lengths, chain conformation and packing style.

The 1D ZnS/CdS chain-like fragments reported by Rosseinsky et al.[268] are embedded in 3D chiral compounds and can also be regarded as 'wires' cut from the bulk ZnS (würtzite) or CdS (rock-salt) structure. The theoretical calculations verified that the VB and CB bands of these compounds are contributed mainly by their inorganic II–VI components, placing them in the same category of II–VI based hybrid materials.

2.14.2.2.2 The two-dimensional single-layered 2D-MQ(L) structures

The 2D-[ZnTe(N_2H_4)] layered structure is shown in Figure 3. The single-atomic slab of ZnTe is parallel to the *ab* plane within which each zinc metal center adopts a distorted tetrahedral geometry defined by one N atom (from a monodentate hydrazine) and three μ_3-Te atoms. The $\{ZnTe\}_n$ layer (6^3 net) is a puckered honeycomb net that closely resembles the (1 1 0) face of zinc blende ZnTe. Therefore, the $\{ZnTe\}_n$ layer can be regarded as a 'slice' cut from its parent structure. The 2D-[ZnTe(ma)] also has a layered structure with the inorganic layers parallel to the *ab* plane (Figure 4); each Zn atom is tetrahedrally coordinated by one N atom (from a monodentate ma) and three μ_3-Te atoms, which is similar to 2D-[ZnTe(N_2H_4)]. However, the $\{ZnTe\}_n$ layer in 2D-[ZnTe(ma)] is analogous to the (1 1 0) crystal face of würtzite ZnTe and hence can be described as a 'slice' cut from the würtzite ZnTe (Figure 4). The Zn–Te distances, $\{ZnTe\}_n$ layer thickness, and interlayer spacing of these two structures, are included in Tables 6 and 7.

The 2D-[ZnSe(L)] (L = ma, ea, pa, ba and ha) layered structures are all obtained in polycrystalline (powder) form, and thus their unit cell parameters are indexed by use of the PXRD data (Table 5). The PXRD patterns of this series of compounds exhibit obvious structural similarity (Figure 5), and the first PXRD peak moves to the lower diffraction angle as the length of the amine molecule increases (i.e., from ma to ha).

2.14.2.2.3 The three-dimensional single-layered 3D-MQ(L)$_{0.5}$ structures

2.14.2.2.3.1 The 3D single-layered structures containing acyclic diamines

The 3D-α-[ZnTe(en)$_{0.5}$] structure adopts an extended 3D framework (Figure 6). In this structure, each zinc atom is tetrahedrally coordinated by one N atom (from an en molecule) and three μ_4-Te atoms. Through alternate connections between Zn and Te atoms, puckered $\{ZnTe\}_n$ layers (6^3 nets) are formed parallel to the *ab* plane and interconnected by

Table 5 Crystal data of II–VI hybrid semiconductors

Compound	a (*Å*)	b (*Å*)/β (°)	c (*Å*)	*S.G.*[a]	Z	$D_{calc.}$	*Method*	*References*
1D-[ZnSe(pda)]	9.9949	6.5324	9.9242	*Pbcm*			PXRD[b]	
1D-α-[ZnTe(N_2H_4)$_2$]	7.2157(4)	11.5439(6)/101.296(1)	7.3909(4)	$P2_1$	4	2.828	SXRD	267
1D-β-[ZnTe(N_2H_4)$_2$]	8.1301(1)	6.9580(5)/91.703(1)	10.7380(7)	*Pn*	4	2.812	SXRD	267
1D-[ZnTe(pda)]	9.997(2)	6.997(1)	10.332(2)	*Pbcm*	4	2.455	SXRD	204
2D-[ZnS(ma)]	6.415(3)	6.194(4)	20.296(11)	*Pbca*			PXRD[b]	
2D-[ZnSe(ma)]	6.7099(17)	6.4786(17)	19.6134(5)	*Pbca*			PXRD[b]	
2D-[ZnSe(ea)]	6.7312(13)	6.4952(9)	24.242(4)	*Pbca*			PXRD[b]	
2D-[ZnSe(pa)]	6.687(2)	6.492(3)	30.289(10)	*Pbca*			PXRD[b]	
2D-α-[ZnSe(ba)]	6.6746(17)	6.4642(10)	34.217(5)	*Pbca*	8	1.957	Rietveld	203
2D-[ZnSe(ha)]	6.686(2)	6.4724(19)	44.161(11)	*Pbca*			PXRD[b]	
2D-[ZnTe(N_2H_4)]	4.2222(6)	6.9057(9)/98.928(3)	7.3031(10)	$P2_1$	2	3.553	SXRD	204
2D-α-[ZnTe(ma)]	7.179(1)	6.946(1)	18.913(4)	*Pbca*	8	3.156	SXRD	204
2D-[Zn_2Se_2(ba)]	6.8035(9)	6.5194(6)	41.894(6)	*Pbca*	8	2.587	Rietveld	203
3D-α-[ZnS(en)$_{1/2}$]	6.393(1)	6.205(1)	17.263(1)	*Pbca*	8		Rietveld	264
3D-[ZnS(pda)$_{1/2}$]	19.907	6.383	6.219	$Cmc2_1$			PXRD[b]	
3D-[ZnS(bda)$_{1/2}$]	6.402	6.183	22.099	*Pbca*			PXRD[b]	
3D-[ZnS(hda) $_{1/2}$]	6.393	6.188	27.314	*Pbca*			PXRD[b]	
3D-α-[ZnSe(en)$_{1/2}$]	6.6374(3)	6.4681(3)	17.3699(7)	*Pbca*	8	3.117	Rietveld	201
3D-α-[ZnSe(pda)$_{1/2}$]	20.0028(8)	6.6356(3)	6.4488(3)	$Cmc2_1$	8	2.825	Rietveld	201
3D-α-[ZnSe(bda)$_{1/2}$]	6.636(3)	6.462(2)	22.275(8)	*Pbca*	8	2.608	Rietveld	202
3D-α-[ZnSe(ptda)$_{1/2}$]	25.124	6.6305	6.4465	$Cmc2_1$			PXRD[a]	
3D-α-[ZnSe(hda)$_{1/2}$]	6.628(2)	6.453(2)	27.152(9)	*Pbca*	8	2.319	Rietveld	202
3D-[ZnSe(hpda)$_{1/2}$]	30.161	6.6251	6.4322	$Cmc2_1$			PXRD[b]	
3D-[ZnSe(dien)$_{1/2}$]	24.720(2)	6.6239(6)	6.4426(6)	$Cmc2_1$	8		Rietveld	324
3D-α-[ZnSe(mxda)$_{1/2}$]	24.991(3)	6.7350(9)	6.4425(5)	$Cmc2_1$	8		Rietveld	261
3D-[ZnTe(N_2H_4)$_{1/2}$]	6.9167(5)	6.8033(5)	13.2853(10)	*Pbca*	8	4.441	SXRD	168
3D-α-[ZnTe(en)$_{1/2}$]	7.061(1)	6.927(1)	17.524(4)	*Pbca*	8	3.457	SXRD	199
3D-β-[ZnTe(en)$_{1/2}$]	5.660(1)	17.156(3)	4.336(1)	*Pnnm*	4	3.518	SXRD	199
3D-[ZnTe(pda)$_{1/2}$]	20.169(4)	7.038(1)	6.882(1)	$Cmc2_1$	8	3.128	SXRD	199
3D-α-[ZnTe(bda)$_{1/2}$]	7.0723(4)	6.9258(4)	22.3497(13)	*Pbca*	8	2.877	SXRD	206
3D-γ-[ZnTe(bda)$_{1/2}$]	7.0996(4)	6.9439(4)	20.4912(11)	*Pbca*	8	3.117	SXRD	206
3D-[ZnTe(ptda)$_{1/2}$]	25.263(5)	7.056(1)	6.903(1)	$Cmc2_1$	8	2.635	SXRD	206
3D-α-[ZnTe(hda)$_{1/2}$]	7.036(1)	6.866(1)	27.008(5)	*Pbca*	8	2.556	SXRD	206
3D-γ-[ZnTe(hda)$_{1/2}$]	7.1353(5)	6.9616(5)	23.7318(18)	*Pbca*	8	2.829	SXRD	206
3D-δ-[ZnTe(hda)$_{1/2}$]	7.1091(14)	34.612(7)	25.091(5)	$P2_12_12_1$	40	2.701	SXRD	206
3D-[CdS(en)$_{1/2}$]	6.841	6.548	16.659	*Pbca*			PXRD[b]	
3D-[CdSe(en)$_{1/2}$][a]	7.0911(5)	6.7628(5)	16.6093(11)	*Pbca*	8	3.693	SXRD	204
3D-[CdSe(pda)$_{1/2}$]	20.6671(12)	6.8904(4)	6.7517(4)	$Cmc2_1$	8	3.156	Rietveld	204
3D-[CdSe(ptda)$_{1/2}$]	25.771	6.852	6.735	$Cmc2_1$			PXRD[b]	
3D-[CdSe(hda)$_{1/2}$]	6.8852	6.7894	27.4113	*Pbca*	8	2.586	Rietveld	266
3D-[CdTe(en)$_{1/2}$]	7.484	7.204	16.821	*Pbca*			PXRD[b]	
3D-α-[MnSe(en)$_{1/2}$]	6.711(1)	6.614(1)	17.720(4)	*Pbca*	8	2.769	SXRD	201
3D-α-[MnSe(pda)$_{1/2}$]	20.383(4)	6.719(1)	6.565(1)	$Cmc2_1$	8	2.526	SXRD	201
3D-α-[MnSe(bda)$_{1/2}$]	6.732(1)	6.590(1)	22.638(5)	*Pbca*	8	2.354	SXRD	168

[a]Space group.
[b]Only unit cells were indexed by the PXRD method.

bidentate en molecules, completing its overall 3D network. As shown in Figure 7, 3D-β-[ZnTe(en)$_{0.5}$] is isomorphous to the α-phase. These two compounds have the same composition, similar coordination mode and 3D structure, but distinctly different configurations in their $\{ZnTe\}_n$ layers. The $\{ZnTe\}_n$ layers in α-phase can be described as 'slices' cut from the würtzite ZnTe (i.e., (1 1 0) crystal faces) while in β-phase as 'slices' cut from the zinc-blende ZnTe. Such a difference results in a different connectivity between the inorganic layers and organic linkers in the two structures.

3D-[ZnTe(pda)$_{0.5}$] also crystallizes in a 3D structure (Figure 8) that belongs to the noncentrosymmetric space group $Cmc2_1$. Both the coordination environment and the overall 3D framework of this compound are analogous to those of 3D-α-[ZnTe(en)$_{0.5}$]; however, the organic diamines dictate the overall symmetry of the framework. Diamine molecules made of even number of carbon atoms have an inversion center (*i*) and they possess a mirror symmetry (*m*) if containing an odd number of carbons. As a result, the corresponding hybrid structures will crystallize in centrosymmetric space group *Pbca* and noncentrosymmetric space group $Cmc2_1$, respectively. Other minor differences for these two groups of structures are found in the connectivity between inorganic and organic components and orientation of their $\{ZnTe\}_n$ layers. As a general rule, all 3D-α-[ZnTe(L)$_{0.5}$] structures with all-*trans* diamines of even numbered carbons such as 3D-α-[ZnTe

Table 6 Selected bond lengths of II–VI hybrid semiconductors and II–VI binaries

Compound	*M-Q (Å)*	*M-N (Å)*	*References*
3D-α-[ZnS(en)$_{1/2}$]	2.336, 2.343, 2.349	2.171	264
ZnS(würtzite)	2.336, 2.341 × 3		30
2D-[Zn_2Se_2(ba)]	2.4464, 2.4540, 2.4505, 2.4550, 2.4501, 2.4535	2.0489	203
3D-α-[ZnSe(en)$_{1/2}$]	2.4353, 2.4433, 2.4703	2.137	201
3D-α-[ZnSe(pda)$_{1/2}$]	2.4350, 2.4572, 2.4753	2.102	201
3D-α-[ZnSe(bda)$_{1/2}$]	2.460, 2.470, 2.491	2.100	202
3D-α-[ZnSe(hda)$_{1/2}$]	2.424, 2.444, 2.489	2.1041	202
3D-α-[ZnSe(dien)$_{1/2}$]	2.437, 2.442, 2.482	1.933	324
2D-α-[ZnSe(ba)]	2.383, 2.4252, 2.464	2.158	203
ZnSe (würtzite)	2.440, 2.434 × 3		30
1D-α-[ZnTe(N_2H_4)$_2$]	2.5839, 2.6197, 2.5798, 2.5836	2.097, 2.115, 2.089, 2.103	267
1D-β-[ZnTe(N_2H_4)$_2$]	2.5902, 2.5914, 2.5752, 2.5905	2.083, 2.107, 2.089, 2.115	267
1D-[ZnTe(pda)]	2.5711, 2.5890	2.102 × 2	204
2D-[ZnTe(N_2H_4)]	2.6147, 2.6294, 2.6339	2.080	204
2D-α-[ZnTe(ma)]	2.6358, 2.6454, 2.6454	2.083	204
3D-α-[ZnTe(N_2H_4)$_{1/2}$]	2.5999, 2.6273, 2.6295	2.125	168
3D-α-[ZnTe(en)$_{1/2}$]	2.6139, 2.6431 × 2	2.111	199
3D-β-[ZnTe(en)$_{1/2}$]	2.632, 2.6389 × 2	2.054	199
3D-[ZnTe(pda)$_{1/2}$]	2.618, 2.634, 2.640	2.059	199
3D-α-[ZnTe(bda)$_{1/2}$]	2.6246, 2.6393, 2.6463	2.095	206
3D-γ-[ZnTe(bda)$_{1/2}$]	2.6141, 2.6431, 2.6547	2.103	206
3D-[ZnTe(ptda)$_{1/2}$]	2.6129, 2.6395, 2.6589	2.070	206
3D-α-[ZnTe(hda)$_{1/2}$]	2.611, 2.617, 2.634	2.075	206
ZnTe (zinc blende)	2.641 × 4		30
ZnTe (würtzite)	2.617 × 3, 2.621		30
3D-[CdSe(en)$_{1/2}$]	2.6177, 2.6247 × 2	2.339	204
3D-α-[CdSe(pda)$_{1/2}$]	2.623, 2.6142, 2.6504	2.354	204
3D-α-[CdSe(hda)$_{1/2}$]	2.594, 2.611, 2.628	2.356	266
CdSe (würtzite)	2.629, 2.632 × 3		30
3D-α-[MnSe(en)$_{1/2}$]	2.5288, 2.5460 × 2	2.179	201
3D-α-[MnSe(pda)$_{1/2}$]	2.5237, 2.5465, 2.5475	2.190	201
3D-α-[MnSe(bda)$_{1/2}$]	2.529, 2.542, 2.559	2.22	201
MnSe (würtzite)	2.520 × 4		30

(bda)$_{0.5}$] and 3D-α-[ZnTe(hda)$_{0.5}$] are all isotypic to 3D-α-[ZnTe(en)$_{0.5}$] and crystallize in *Pbca* (**Figures 9(a) and 9(c)**), and all 3D-[ZnTe(L)$_{0.5}$] structures having all-*trans* diamines of odd numbered carbons (e.g., ptda and hpda) belong to $Cmc2_1$ and are isotypic to 3D-[ZnTe(pda)$_{0.5}$] (**Figure 9(b)**). For longer chain diamine molecules, several conformations exist and they lead to a number of different hybrid structures. For example, hda molecules adopt both *trans* and *gauche* conformations in 3D-δ-[ZnTe(hda)$_{0.5}$] (rather than all *trans* in the α-phase) (**Figure 10**); this structure possesses a chiral space group $P2_12_12_1$ and its interlayer distances (between {ZnTe}$_n$ layers) are much shorter than those in 3D-α-[ZnTe(hda)$_{0.5}$] (**Table 7**).

3D-[ZnSe(L)$_{0.5}$] (L = en, pda, bda, ptda, hda, hpda, and dien) compounds are all obtained in polycrystalline (powder) form. Crystal structures of selected phases, such as 3D-[ZnSe(en)$_{0.5}$], 3D-[ZnSe(pda)$_{0.5}$], 3D-[ZnSe(bda)$_{0.5}$], and 3D-[ZnSe(hda)$_{0.5}$], are refined and determined by the Rietveld method based on their PXRD patterns. Among them, 3D-[ZnSe(en)$_{0.5}$], 3D-[ZnSe(bda)$_{0.5}$], and 3D-[ZnSe(hda)$_{0.5}$] are isotypic to their corresponding 3D-α-[ZnTe(L)$_{0.5}$] counterparts, while 3D-[ZnSe(pda)$_{0.5}$] is isostructural to 3D-[ZnTe(pda)$_{0.5}$]. Analogous to the 3D-α-[ZnTe(L)$_{0.5}$] family, 3D-[ZnSe(L)$_{0.5}$] structures comprise {ZnSe}$_n$ layers that can be described as 'slices' cut from the würtzite ZnSe (i.e., (1 1 0) crystal faces). Paralleled {ZnSe}$_n$ layers are interconnected by bidentate diamine linkers, forming 3D inorganic–organic hybrid structures. The PXRD patterns for this series of compounds are shown in **Figure 11**. From **Table 7**, we can see that as the length of the amine spacer increases (from L = en to hda), the distance between the adjacent {ZnQ}$_n$ (Q = Se, Te) layers for 3D-[ZnQ(L)$_{0.5}$] series increases correspondingly. However, the thickness of the {ZnQ}$_n$ layers experiences very little change. The PXRD patterns of 3D-[ZnS(L)$_{0.5}$] (L = en, pda, bda, ptda, hda) compounds are shown in **Figure 12**. This group of hybrids is also obtained only in polycrystalline form, and the crystal structure of a representative member 3D-[ZnS(en)$_{0.5}$] is solved by Rietveld refinement. The results show that 3D-[ZnS(en)$_{0.5}$] is isostructural to 3D-α-[ZnTe(en)$_{0.5}$]. Based on this analysis as well as the similarity of their PXRD patterns, other 3D-[ZnS(L)$_{0.5}$] structures are assigned the same space groups as 3D-[ZnTe(L)$_{0.5}$].

The single-crystal structure of 3D-[CdSe(en)$_{0.5}$] was obtained by Deng et al.[265] and us independently. It is isostructural to 3D-[ZnSe(en)$_{0.5}$]. The 3D network of 3D-[CdSe(en)$_{0.5}$] consists of inorganic {CdSe}$_n$ layers interconnected by en molecules (**Figure 13**), and these {CdSe}$_n$ layers can also be considered as 'slices' cutting from the (1 1 0) crystal faces of

Table 7 Interlayer distance, layer thickness, and amine length for selected II–VI hybrid semiconductors

Compound	*Interlayer distance (Å)*[a]	*MQ layer thickness (Å)*[b]	*Amine length (Å)*[c]	*References*
2D-α-[ZnSe(ba)]	12.78	4.34	6.575	203
2D-[ZnTe(N_2H_4)]	2.64	4.58	2.925	204
2D-α-[ZnTe(ma)]	4.04	5.41	2.945	204
2D-[Zn_2Se_2(ba)]	12.58	8.48	6.297	203
3D-α-[ZnS(en)$_{1/2}$]	4.24	4.39	5.247	264
3D-α-[ZnSe(en)$_{1/2}$]	3.92	4.76	5.335	201
3D-α-[ZnSe(pda)$_{1/2}$]	5.20	4.80	6.628	201
3D-α-[ZnSe(bda)$_{1/2}$]	6.28	4.86	7.949	202
3D-α-[ZnSe(hda)$_{1/2}$]	8.84	4.74	10.374	202
3D-α-[ZnSe(dien)$_{1/2}$]	7.58	4.78	9.136	324
3D-α-[ZnSe(mxda)$_{1/2}$]	7.92	4.58	8.683	261
3D-α-[ZnTe(N_2H_4)$_{1/2}$]	1.28	5.36	2.840	168
3D-α-[ZnTe(en)$_{1/2}$]	3.36	5.40	5.292	199
3D-β-[ZnTe(en)$_{1/2}$]	3.14	5.44	5.322	199
3D-[ZnTe(pda)$_{1/2}$]	4.68	5.40	6.518	199
3D-α-ZnTe(bda)$_{1/2}$	5.78	5.39	7.793	206
3D-γ-ZnTe(bda)$_{1/2}$	4.86	5.39	7.028	206
3D-ZnTe(ptda)$_{1/2}$	7.22	5.41	9.084	206
3D-α-ZnTe(hda)$_{1/2}$	8.12	5.39	10.355	206
3D-γ-ZnTe(hda)$_{1/2}$	6.48	5.39	9.265	206
3D-δ-ZnTe(hda)$_{1/2}$	6.25	5.32	9.178, 9.220, 9.545, 10.274, 10.304	206
3D-[CdSe(en)$_{1/2}$]	3.16	5.09	5.227	204
3D-α-[CdSe(pda)$_{1/2}$]	5.14	5.19	6.663	204
3D-α-[CdSe(hda)$_{1/2}$]	8.66	5.05	10.24	266
3D-α-[MnSe(en)$_{1/2}$]	3.88	4.98	5.29	201
3D-α-[MnSe(pda)$_{1/2}$]	5.20	4.99	6.506	201
3D-α-[MnSe(bda)$_{1/2}$]	6.34	4.98	7.758	168

[a]Interlayer distance: perpendicular distance between the centers of two Q atoms from adjacent layers minus 2*r* (*r* = covalent radius of Q atoms: Q = Te, 1.37 Å; Q = Se, 1.17 Å; Q = S, 1.04 Å).
[b]Layer thickness: perpendicular distance between the centers of two Q atoms at the opposite sides of an inorganic layer plus 2*r*.
[c]Amine length: distance between two N atoms plus 1.48 Å (i.e., covalent diameter of N).

würtzite CdSe. Other 3D-[CdSe(L)$_{0.5}$] compounds such as 3D-[CdSe(pda)$_{0.5}$], 3D-[CdSe(bda)$_{0.5}$], and 3D-[CdSe(ptda)$_{0.5}$] are in polycrystalline form. PXRD patterns of these hybrids are similar (Figure 14), implying that they all adopt analogous structures.

The 3D-[CdS(L)$_{0.5}$] (L = en, pda, bda, ptda, hda) and 3D-[CdTe(L)$_{0.5}$] (L = en, pda,) hybrids are also obtained in polycrystalline form, and their PXRD patterns are shown in Figures 15 and 16, respectively. In addition, the unit-cell parameters of 3D-[CdTe(en)$_{0.5}$] can be generated by indexing its PXRD pattern (Table 5).

The crystal structures of MnSe-based hybrid materials 3D-[MnSe(L)$_{0.5}$] (L = en, pda, and bda) are determined by SXRD. The results show that all of them are isostructural to their ZnSe analogues 3D-[ZnTe(L)$_{0.5}$]. The selected bond lengths of these compounds are listed in Table 5.

2.14.2.2.3.2 The 3D single-layered structures containing cyclic diamines

3D-α-[ZnSe(mxda)$_{0.5}$] was synthesized in powder form and its crystal structure has been characterized by PXRD and refined by the Rietveld method.[261] This 3D structure crystallizes in a orthorhombic space group $Ccm2_1$ and also contains single-layered $\{ZnSe\}_n$ slabs interconnected by mxda molecules (Figure 17). The infinite $\{ZnSe\}_n$ slabs can be regarded as 'slices' cut from the würtzite ZnSe (i.e., (1 1 0) crystal faces); hence, this material possesses the same structure type as 3D-α-[ZnSe(en)$_{0.5}$].

Song et al.[259,260] reported other two examples of II–VI hybrid semiconductors containing cyclic diamines, that is, [ZnS(cha)$_x$] and [CdS(cha)$_x$]. The samples were prepared in the form of nanofibers in which periodic layered structures with thickness of ~2–3 nm were identified by a high-resolution transmission electron microscope (HRTEM). The HRTEM images further indicate that their layered structures are formed by interlaced arrangement of the amorphous cha and crystalline würtzite ZnS. Another similar case is [Zn(pz)$_{0.5}$],[262] which is a metastable nanomaterial and can be described as the layered structure where würtzite ZnS layers are connected to each other through bidentate piperazine molecules. Interestingly, at sufficiently high temperature, the piperazine molecules can be removed from the layers and residue nitrogen atoms left in the structure then act as dopants to afford N-doped ZnS.

2.14.2.2.4 The two-dimensional double-layered 2D-M_2Q_2(L) structures

All the double-layered compounds 2D-[M_2Q_2(L)] (M = Zn, Cd; Q = S, Se; L = ea, pa, ba and ha) are in powder form, and their structures are characterized by the PXRD method. From Figures 18–21, we see that the PXRD patterns of these hybrids

are analogous, indicating that they are all isostructures. As the length of the amine molecules increases from ea to ha, the first peak of each PXRD pattern shifts to a lower 2θ diffraction angle. Moreover, the PXRD peaks of this series of compounds are relatively broad and have low intensities, implying relatively poorer crystallinity and smaller particle sizes.

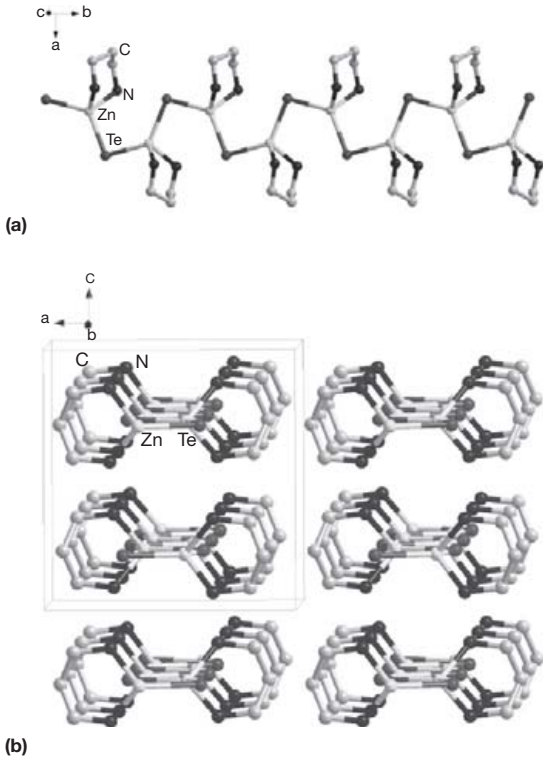

Figure 1 Crystal structure of 1D-[ZnTe(pda)]: (a) 1D $\{ZnTe(pda)\}_n$ chain along the *b*-axis. (b) The overall structure viewing down the *b*-axis. Hydrogen atoms are omitted for clarity.

To study the detailed crystal structure of double-layered hybrids, 2D-[Zn_2Se_2(ba)] was selected as the representative model. The unit cell parameters of this compound were obtained by fully indexing synchrotron PXRD data and the Rietveld method was used to refine the crystal structure. It has been found that 2D-[Zn_2Se_2(ba)] crystallizes in an orthorhombic space group Pbca, and consists of double-layered 2D $\{Zn_2Se_2\}_n$ motifs coordinated by ba molecules projecting outward from $\{Zn_2Se_2\}_n$ layers (Figure 22). In this compound, two crystallographically distinct Zn sites are observed, one coordinated by two μ_3-Se atoms, one μ_4-Se atom, and one N atom from the ba molecule, and the other coordinated by three μ_4-Se atoms and one μ_3-Se atom. Compared to the single-layer structure 2D-[ZnSe(ba)], the only difference between the two is the length of the *c* axis. In addition, the double-layered $\{Zn_2Se_2\}_n$ moieties in 2D-[Zn_2Se_2(ba)] can also be considered as a 'slab' cut from the (1 1 0) crystal face of würtzite ZnSe.

2.14.2.3 Selected Properties

2.14.2.3.1 Optical absorption and bandgaps

Optical absorption behaviors of II–VI hybrid semiconductors are investigated by measuring their diffuse reflectance at room temperature using solid polycrystalline/powder samples. The phase purity of samples is usually identified by the PXRD analysis prior to the optical absorption studies. The bandgaps of these materials are obtained by converting the diffuse reflectance data into a Kubelka–Munk function[199,204] that is directly proportional to the absorption coefficient.

The optical absorption spectra of selected II–VI hybrids as well as their parent II–VI binaries are shown in

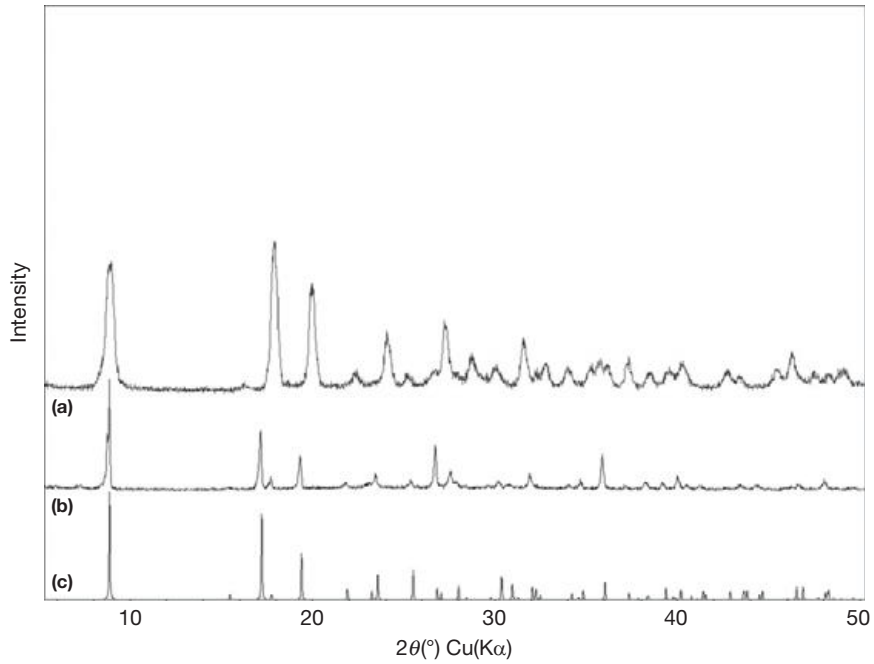

Figure 2 PXRD patterns of (a) 1D-[ZnSe(pda)], (b) 1D-[ZnTe(pda)], and (c) the simulated pattern of 1D-[ZnTe(pda)] (using the single-crystal data).

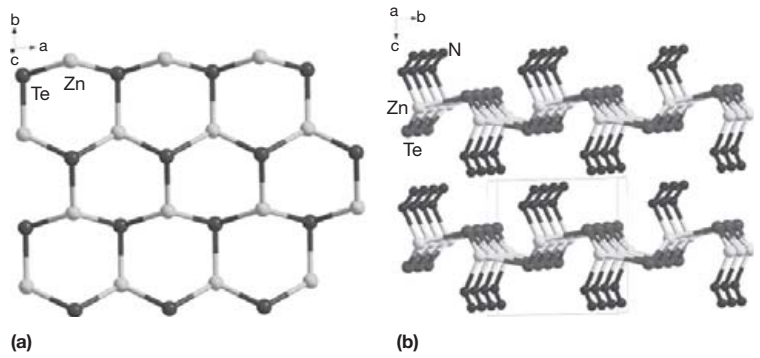

Figure 3 Crystal structure of 2D-[ZnTe(N_2H_4)]: (a) 2D $\{ZnTe\}_n$ single layer. (b) The overall structure viewing down the *a*-axis. Hydrogen atoms are omitted for clarity.

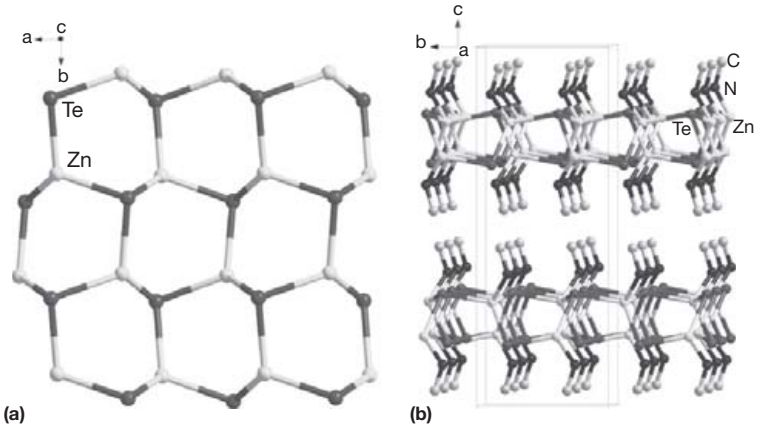

Figure 4 Crystal structure of 2D-[ZnTe(ma)]: (a) 2D $\{ZnTe\}_n$ single layer in this structure. (b) The overall structure viewing down the *a*-axis. Hydrogen atoms are omitted for clarity.

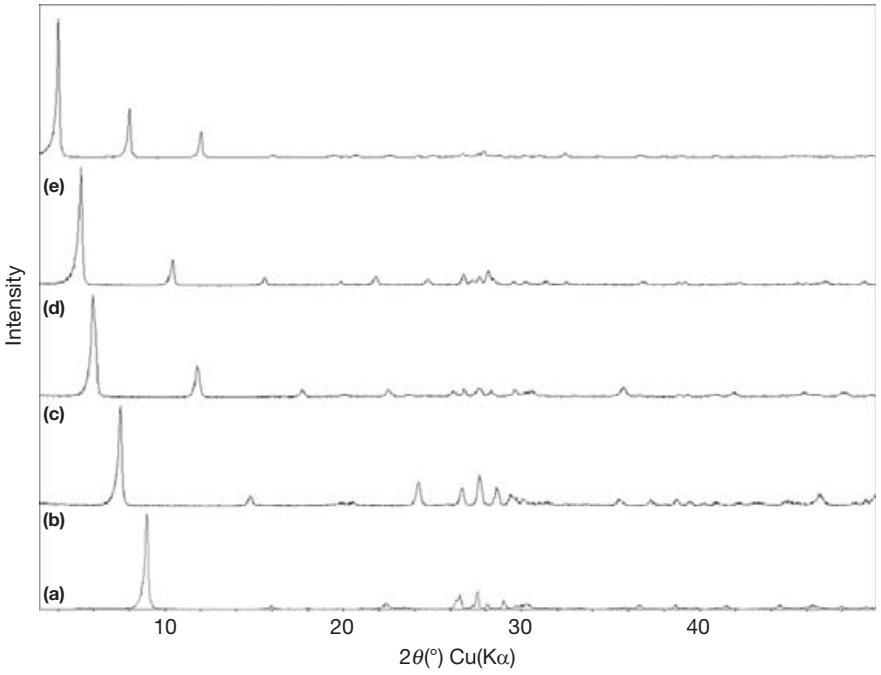

Figure 5 PXRD patterns of (a) 2D-[ZnSe(ma)], (b) 2D-[ZnSe(ea)], (c) 2D-[ZnSe(pa)], (d) 2D-[ZnSe(ba)], and (e) 2D-[ZnSe(ha)].

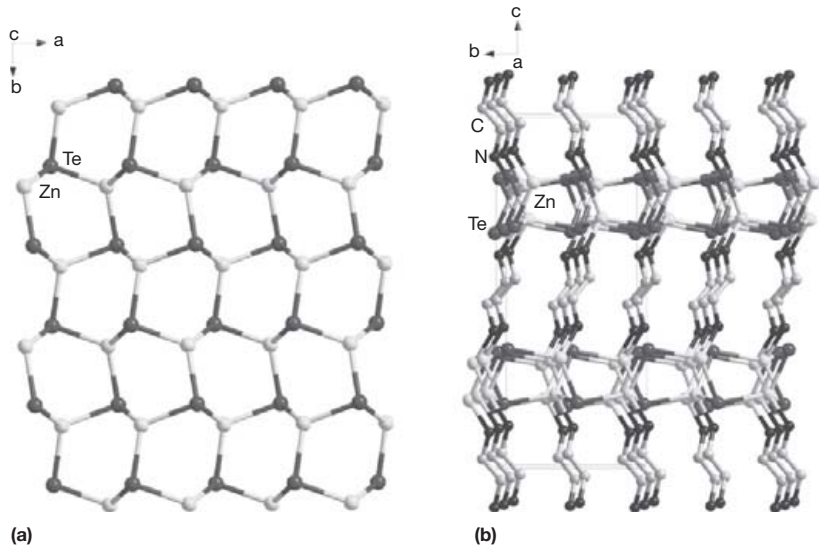

Figure 6 Crystal structure of 3D-α-[ZnTe(en)$_{0.5}$]: (a) 2D {ZnTe}$_n$ single layer. (b) The overall structure viewing down the *a*-axis. Hydrogen atoms are omitted for clarity.

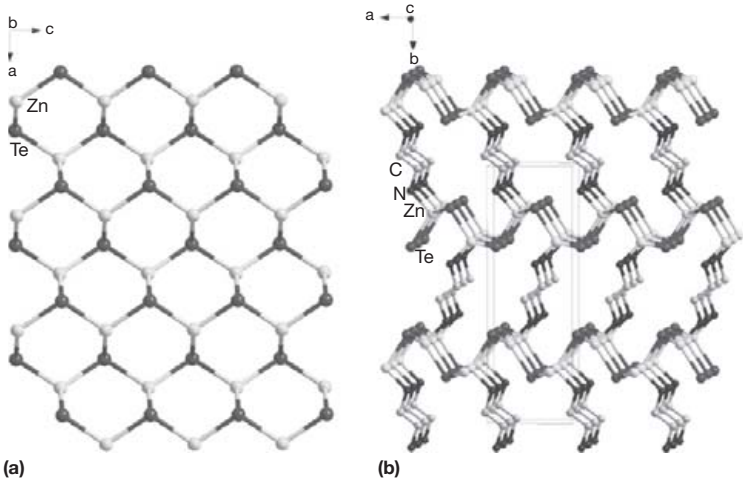

Figure 7 Crystal structure of 3D-β-[ZnTe(en)$_{0.5}$]: (a) 2D {ZnTe}$_n$ single layer. (b) The overall structure viewing down the *c*-axis. Hydrogen atoms are omitted for clarity.

Figures 23 and 24. These spectra clearly illustrate that all the hybrid compounds exhibit very large blue shifts (i.e., shifting to higher energy) in their absorption edges, comparing with their parent inorganic phases. The absorption intensity is also enhanced to a large extent. The experimental bandgap values and estimated blue shifts are included in Table 8 for selected II–VI hybrid compounds.

Some interesting trends may be extracted by comparing data listed in Table 8: (a) except for Mn-based phases, all other II–VI hybrids exhibit large bandgap increase (~0.7–2.0 eV) with respect to their parent II–VI binary compounds; (b) varying the length of organic linkers has negligible effect on both the blue shift and bandgap values of the hybrids; (c) single-atomic 1D hybrid compounds 1D-[(MQ)(L)] exhibit greater blue shift than their 2D and 3D analogues, while the bandgap and blue shift values are very similar among single-layered 2D and 3D hybrid structures 2D-[(MQ)(L)] and 3D-[(MQ)(L)$_{0.5}$], respectively; and (d) the blue shifts of double-layered 2D-[(M_2Q_2)(L)] hybrids are significantly smaller than single-layered 2D-[(MQ)(L)] compounds.

These observed trends can be well explained based on the unique nature of this unprecedented series of nanostructured hybrid materials. First, the large blue shift is due to the strong QCE that occurred in these materials. Notably, the extent of such QCE is much stronger than what was found in colloidal QDs. This is because the thickness of the layers or the diameter of the chains being confined in the hybrid structures is at a significantly smaller scale compared to the physical dimensions of the colloidal QDs. Generally, the thickness of a single MQ layer is in the range of 0.43–0.55 nm (Table 7). Consequently, the QCE extent of most II–VI hybrids is much stronger than what has been achieved for the smallest colloidal QDs reported to date.[154,207–210] As an exception of this observation, MnSe-based hybrid compounds only show a negligible blue

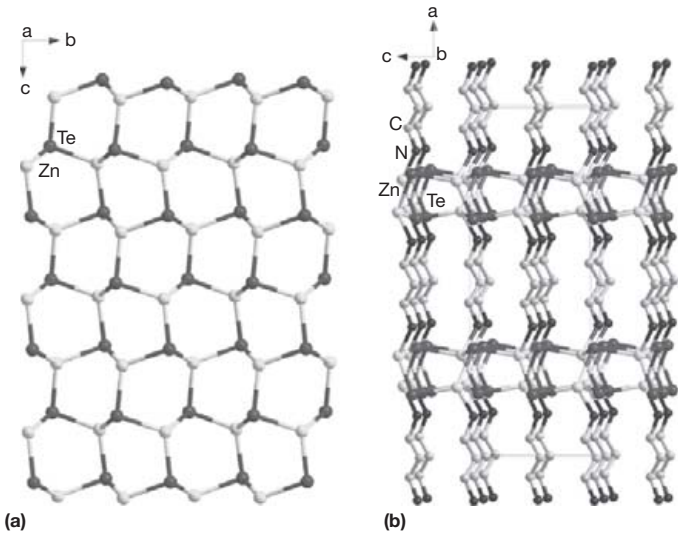

Figure 8 Crystal structure of 3D-α-[ZnTe(pda)$_{0.5}$]: (a) 2D {ZnTe}$_n$ single layer. (b) The overall structure viewing down the *b*-axis. Hydrogen atoms are omitted for clarity.

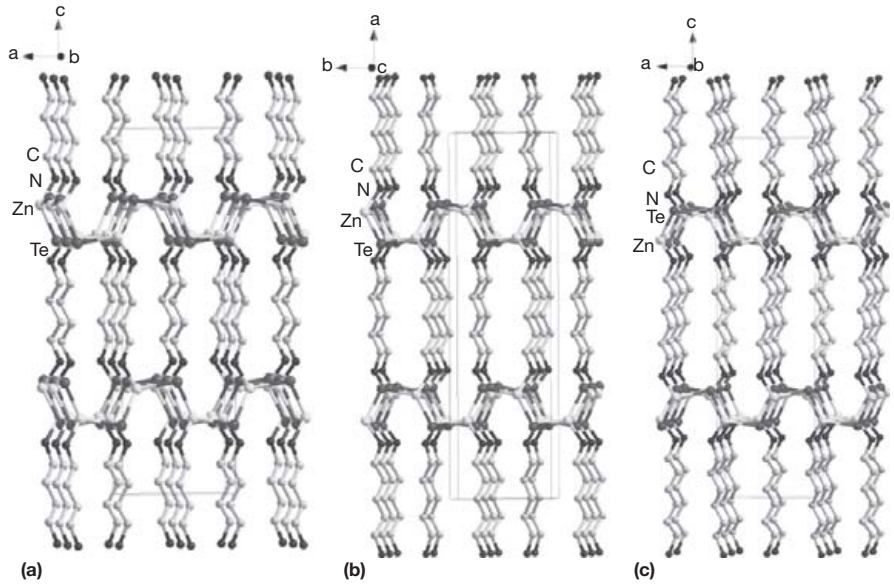

Figure 9 Crystal structures of (a) 3D-α-[ZnTe(bda)$_{0.5}$], (b) 3D-[ZnTe(ptda)$_{0.5}$], and (c) 3D-α-[ZnTe(hda)$_{0.5}$]. Hydrogen atoms are omitted for clarity.

shift of 0.1–0.2 eV compared to the parent phase. This very small QCE is attributed to the highly localized 3d bands of Mn.

Second, because the hybrid structures are modular, the semiconductor moieties (2D layer or 1D chain) are largely stand-alone in nature, where the composition, bonds, charge balance, coordination environment, and structure are very little perturbed from the parent binary phases. Therefore, the semiconductor properties originated from the parent bulk materials are inheritably preserved in the hybrid structures. As long as the inorganic components remain the same, the variation in the length of organic amines (spacers) will have very little effect on the bandgap and other associated properties. This elucidation is further verified by the theoretical calculations which reveal that the valence and conduction bands of the hybrids are overwhelmingly dominated by the inorganic II and VI atomic states (see **Section** 2.14.2.3.2). Furthermore, it is well understood that because the 1D hybrid structures are confined to two dimensions (similar to quantum wires), they exhibit larger blue shift than their 2D and 3D counterparts that are made of II–VI atomic layers confined only to one dimension (similar to quantum wells).

Finally, the bandgap of the hybrid materials containing II–VI layers can be systematically tuned by simply varying a single structural parameter, the number of single atomic slabs (n) within a layer. Comparing to the analogous method used to control the size of colloidal QDs, this structure-based tuning approach is far more efficient and precise. As shown in **Figure 25(a)**, the parent bulk materials (MQ) can be considered as made of 'infinite' number of single atomic MQ slab ($n=\infty$), while the hybrid structures comprised of single

atomic MQ layers (such as 3D-[MQ(L)$_{0.5}$]) have $n=1$. These two extreme cases correspond to the largest ($n=1$) and zero ($n=\infty$) structure-induced QCE, respectively. By making the hybrid structures with various n values between 1 and ∞, the bandgap and other related properties can thus be tuned precisely and rationally. Two intermediate cases with $n=2$ (double-layer) and $n=3$ (triple-layer) are illustrated in Figure 25(a). As an example, the absorption spectra of double-layered 2D-[(Zn_2Se_2)(ba)] and single-layered 2D-[(ZnSe)(ba)] are compared in Figure 25(b). Because the thickness of the $\{Zn_2Se_2\}_n$ layer is approximately twice that of the $\{ZnSe\}_n$ layer, the QCE (exhibiting as the blue shift in the bandgap) in the double-layered phase ($n=2$) is significantly smaller than that in the single-layered phase ($n=1$).

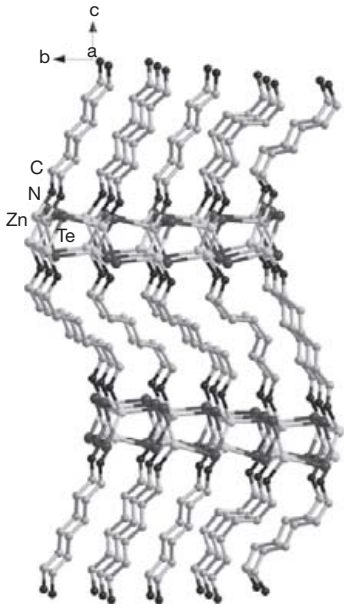

Figure 10 Crystal structure of 3D-δ-[ZnTe(hda)$_{0.5}$]. Hydrogen atoms are omitted for clarity.

2.14.2.3.2 The band structures

Calculations of band structure (BS) and density of states (DOS) have been carried out for selected II–VI hybrids using their single crystal structures as starting models. A planewave code CASTEP is used in these calculations.[269–271] The total energy is calculated by density functional theory (DFT) within the framework of a nonlocal generalized gradient approximation (i.e., Perdew–Burke–Ernzerhof (PBE) functional).[272] The interactions between the ionic cores and electrons are described by the ultrasoft pseudopotential.[269,273] The following electrons are treated as valence electrons: Zn: $3d^{10}4s^2$, Cd: $4d^{10}5s^2$, Se: $4s^24p^4$, Te: $5s^25p^4$, C: $2s^22p^2$, N: $2s^22p^3$, and H:$1s^1$. Pseudopotentials are used for all atoms. The number of plane waves included in the basis is determined by a cutoff energy and the numerical integration of the Brillouin zone is performed using different Monkhorst–Pack k-point setting (see Table 9). The other calculation parameters and convergent criteria are taken from default values of the CASTEP code.

The calculated results are tabulated in Table 9, from which we can see that the calculated blue shifts of II–VI hybrids are in excellent agreement with the experimental values. Also, it is observed that the calculated bandgaps are smaller than the experimental ones. This is not surprising because it is well-known that the DFT-GGA (generalized gradient approximation) does not accurately describe the eigenvalues of the electronic states, which causes quantitative underestimation of bandgaps.[274–276] Remarkably, this systematic error (~0.8–0.9 eV) is demonstrated to be transferable from bulk II–VI to hybrid compounds (Table 9).

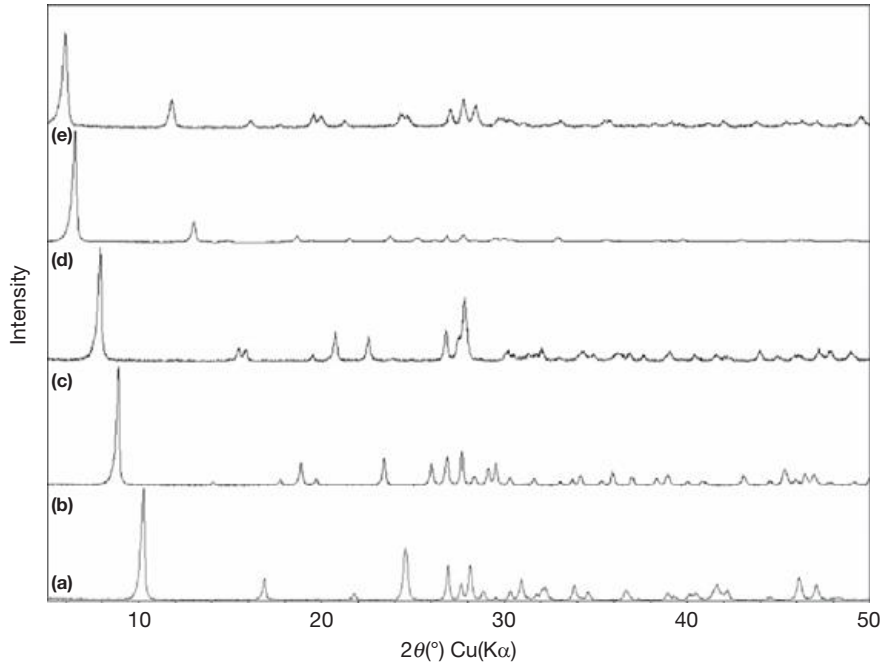

Figure 11 PXRD patterns of (a) 3D-[ZnSe(en)$_{0.5}$], (b) 3D-[ZnSe(pda)$_{0.5}$], (c) 3D-[ZnSe(bda)$_{0.5}$], (d) 3D-[ZnSe(hda)$_{0.5}$], and (e) 3D-[ZnSe(hpda)$_{0.5}$].

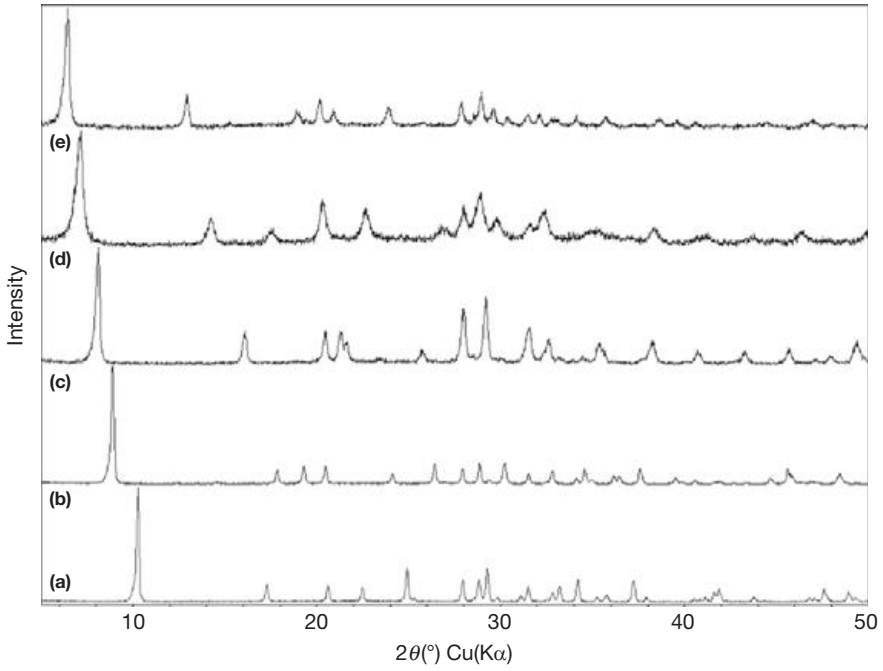

Figure 12 PXRD patterns of (a) 3D-[ZnS(en)$_{0.5}$], (b) 3D-[ZnS(pda)$_{0.5}$], (c) 3D-[ZnS(bda)$_{0.5}$], (d) 3D-[ZnSe(ptda)$_{0.5}$], and (e) 3D-[ZnSe(hda)$_{0.5}$].

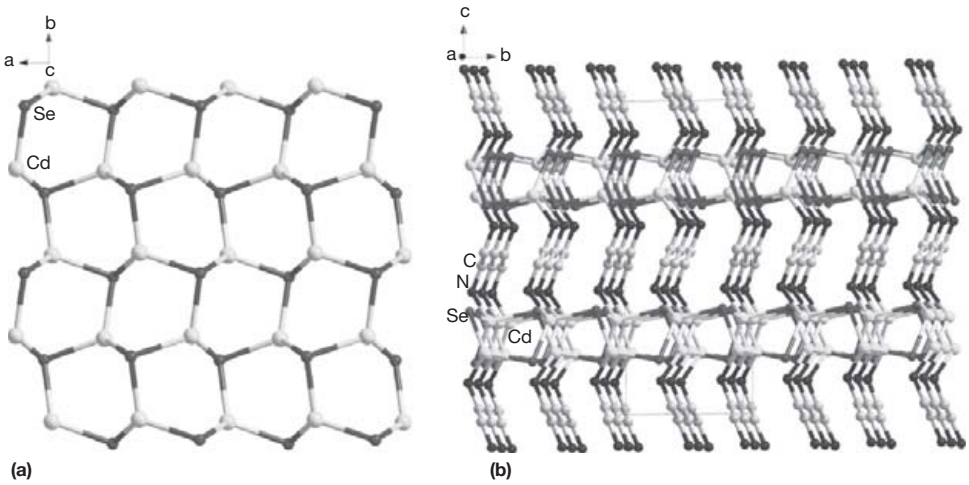

Figure 13 Views of the 3D-[CdSe(en)$_{0.5}$] structure: (a) a {CdSe}$_n$ single layer in the structure. (b) The overall structure viewing down the *a*-axis. Hydrogen atoms are omitted for clarity.

The band structures as well as the total and partial DOS of 3D-α-[ZnTe(en)$_{1/2}$], 3D-β-[ZnTe(en)$_{1/2}$], 3D-[ZnTe(pda)$_{1/2}$], 3D-[CdSe(en)$_{1/2}$], and 2D-α-[ZnTe(ma)] are plotted in Figures 26–30, respectively. Based on the calculated bands, it is clear that all compounds possess direct bandgaps. The DOS plots of all hybrid structures show very similar features, as evident from Figures 26–30. In the case of 3D-α-[ZnTe(en)$_{1/2}$] (Figure 26), the conduction bands are predominately contributed from the inorganic elements. The major contributions are from the Zn-4s atomic orbitals, along with lesser contributions from Zn-4p, Te-5s, and Te-5p states. The valence bands from −2.6 eV to the Fermi level are largely made of Te-5p atomic orbitals, with partial contributions of Zn-4s, Zn-4p, and Te-5s states. The occupied bands at lower energies (between −22 and −11.5 eV) are primarily the C-2s, C-2p, N-2s, and N-2p atomic states. The sharp and narrow d-band from −7.5 to −5 eV is exclusively from the Zn-3d orbitals.

A comparison of the density of states of 3D-α-[ZnTe(en)$_{1/2}$] with those of the würtzite ZnTe (Figure 26(d)) reveals that: (a) There is a clear bandgap increase in the hybrid phase, and its electronic band structure resembles the parent structure with similar distributions of atomic states in the VB and CB energy states. This verifies that the electronic states and semiconductor properties of the binary species are well preserved going from a parent bulk to a hybrid structure. (b) The atomic orbitals contributed to the VB and CB are almost exclusively from the inorganic component, with negligible involvement of the

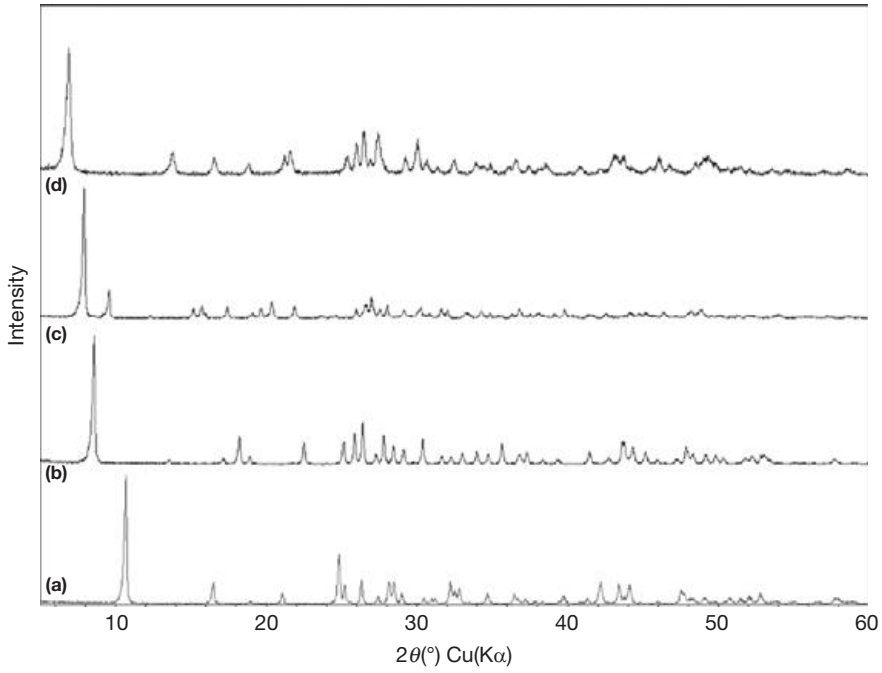

Figure 14 PXRD patterns of (a) 3D-[CdSe(en)$_{0.5}$], (b) 3D-[CdSe(pda)$_{0.5}$], (c) 3D-[CdSe(bda)$_{0.5}$], and (d) 3D-[CdSe(ptda)$_{0.5}$].

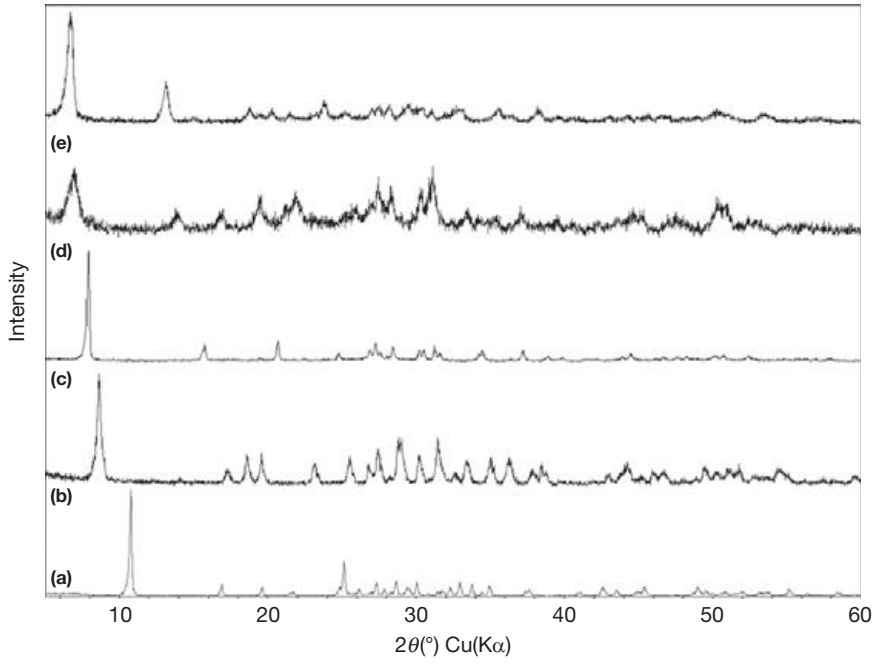

Figure 15 PXRD patterns of (a) 3D-[CdS(en)$_{0.5}$], (b) 3D-[CdS(pda)$_{0.5}$], (c) 3D-[CdS(bda)$_{0.5}$], (d) 3D-[CdS(ptda)$_{0.5}$], and (e) 3D-[CdS(hda)$_{0.5}$].

organic component. This result confirms that any electronic and optical properties related to the electronic states in the frontier region (VB + CB) will be predominantly determined by the inorganic II–VI modules, and the role of organic spacers is largely passivation. Consequently, the observed large blue shifts in the band-edge optical absorption spectra of the II–VI hybrids are due to the strong QCE induced by the organic spacers. These findings are further verified by calculations on other hybrid systems (Figures 27–30). Furthermore, band structure and transition probability of selected II–VI hybrids have also been calculated by the DFT-LDA method.[199,277,278] The results from different computational methods are fully consistent.

2.14.2.3.3 Thermal stability

Thermal stability of II–VI hybrid semiconductors has been studied by the TGA performed on polycrystalline/powder

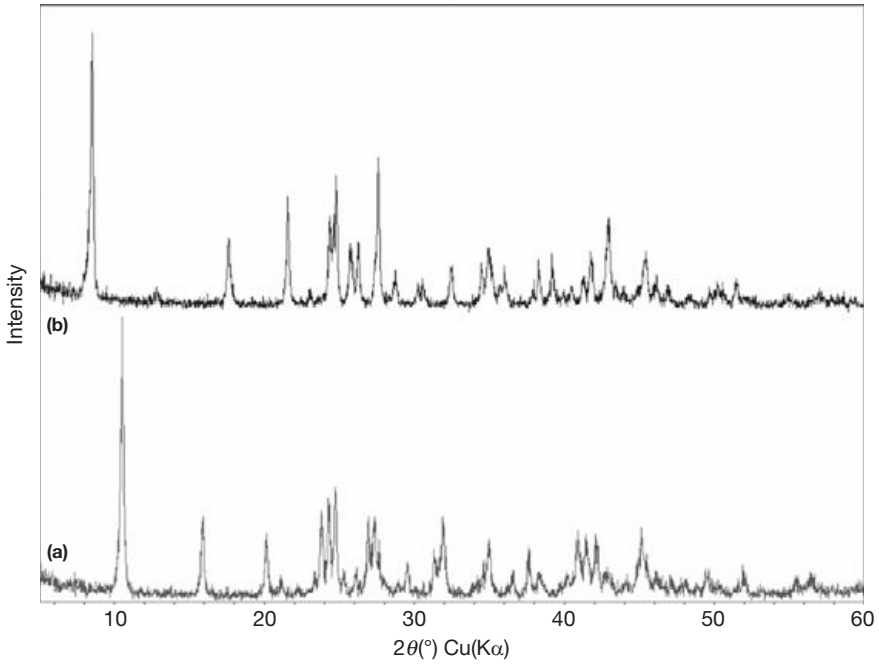

Figure 16 PXRD patterns of (a) 3D-[CdTe(en)$_{0.5}$] and (b) 3D-[CdTe(pda)$_{0.5}$].

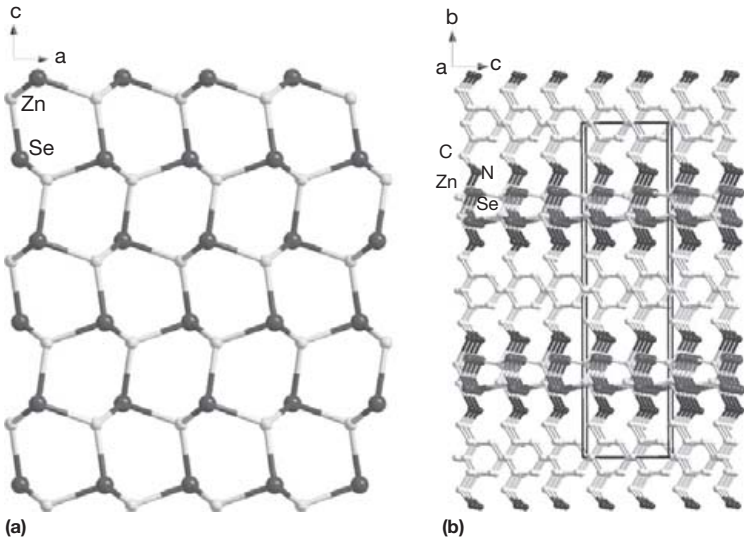

Figure 17 Views of the 3D-α-[ZnSe(mxda)$_{0.5}$] structure: (a) a {ZnSe}$_n$ single layer. (b) The overall structure viewing down the *a*-axis. Hydrogen atoms are omitted for clarity.

samples. Some other thermally related properties, such as contents of the organic components, thermolysis behavior, as well as the phase-transition process, are also investigated by TGA experiments. Relevant results are included in Table 10; TGA profiles of selected compounds (e.g., 2D-[ZnSe(L)]) are illustrated in Figure 31 as representative examples.

The TGA data shown in Table 10 illustrate that most of the II–VI hybrid compounds are thermally stable between 100 and 200 °C. Above this temperature, they start to lose their organic components in a single-step weight-loss process. A few of them undergo multistep weight loss. As shown in Table 10, the experimental weight loss is generally in good agreement with the theoretical value calculated from the molecular formula.

The post-TGA residual materials are characterized by PXRD and the phases are identified as inorganic II–VI binaries. For most ZnTe-based hybrids, the residue is zinc blende ZnTe. One exception is 3D-α-[ZnTe(en)$_{0.5}$], for which both the zinc blende (major) and the würtzite (minor) phase are found at higher temperatures (e.g., >420 °C). For ZnS, ZnSe, CdS, and CdSe-based hybrids; however, the post-TGA residuals are würtzite phase. As illustrated examples, post-TGA PXRD patterns of 3D-[ZnSe(L)$_{0.5}$] phases are shown in Figure 32.

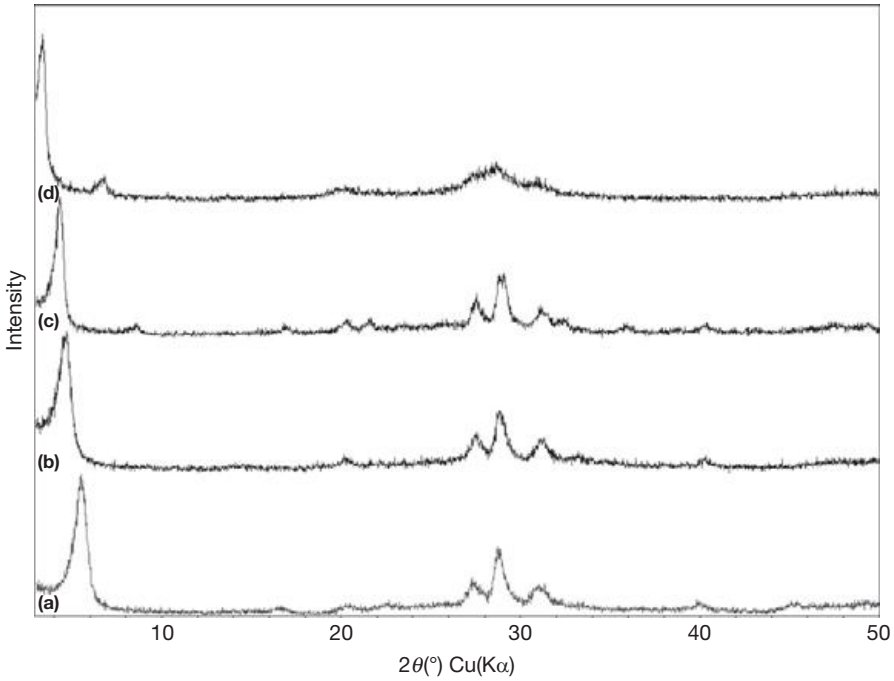

Figure 18 PXRD patterns of (a) 2D-[Zn_2S_2(ea)], (b) 2D-[Zn_2S_2(pa)], (c) 2D-[Zn_2S_2(ba)], and (d) 2D-[Zn_2S_2(ha)].

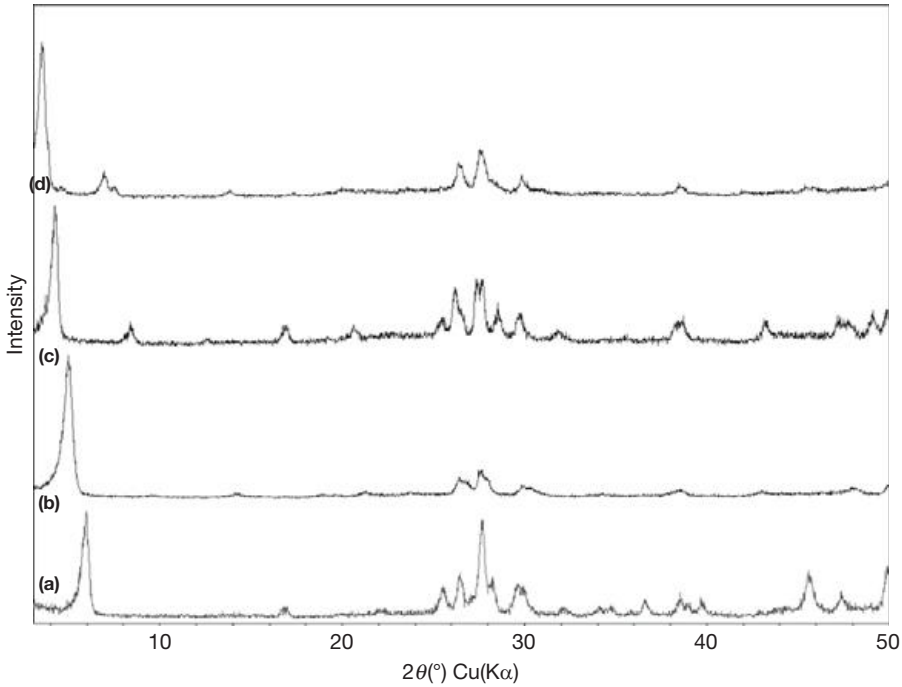

Figure 19 PXRD patterns of (a) 2D-[Zn_2Se_2(ea)], (b) 2D-[Zn_2Se_2(pa)], (c) 2D-[Zn_2Se_2(ba)], and (d) 2D-[Zn_2Se_2(ha)].

Generally, the thermal stability of the II–VI hybrids depends on the type of inorganic component, nature of organic linker, as well as the overall structural dimensionality. Within the group of 3D hybrid structures, the Cd-based compounds are less thermally stable than Zn-based phases (Table 10). As the structural dimensionality lowers (e.g., from 3D to 1D), the thermal stability of the II–VI hybrids decreases accordingly. For example, 3D-[$ZnS(L)_{0.5}$], 3D-[$ZnSe(L)_{0.5}$], and 3D-[$ZnTe(L)_{0.5}$] decompose in the temperature ranges of 314–359, 312–353, and 290–318 °C, respectively; however, the decomposition temperatures for 2D-[ZnS(L)] and 2D-[ZnSe(L)] are within 173–182 and 194–215 °C, respectively.

The post-TGA residuals of some II–VI hybrid compounds are virtually nanoparticles with a variety of morphologies,

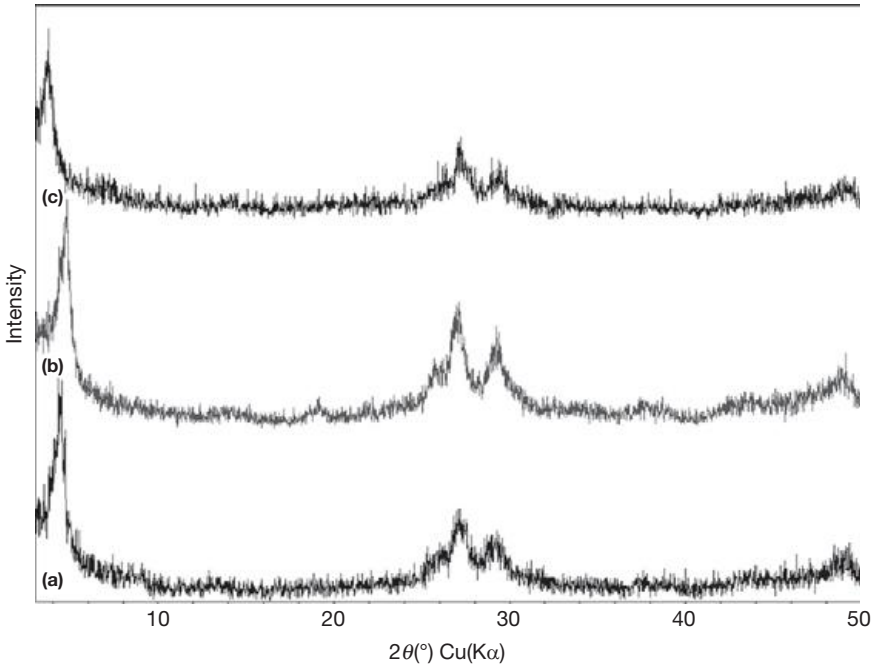

Figure 20 PXRD patterns of (a) 2D-[Cd_2S_2(pa)], (b) 2D-[Cd_2S_2(ba)], and (c) 2D-[Cd_2S_2(ha)].

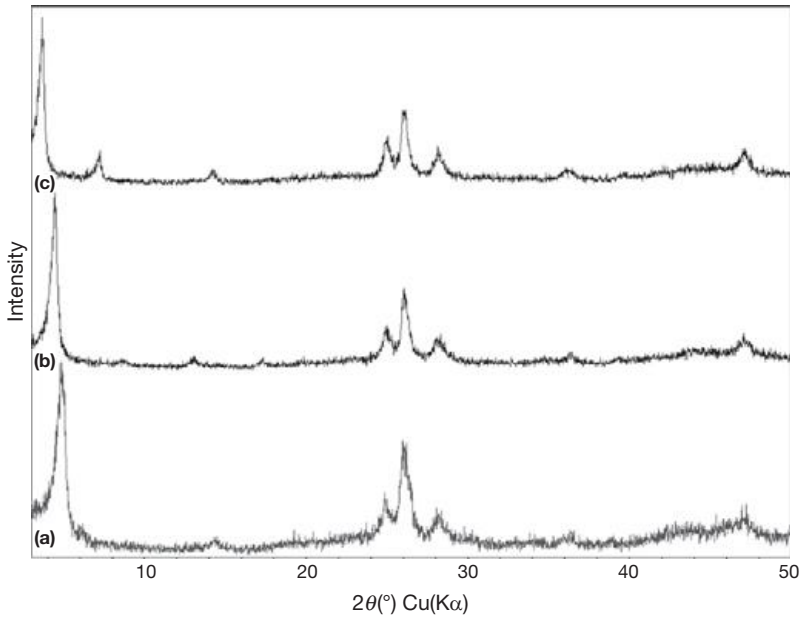

Figure 21 PXRD patterns of (a) 2D-[Cd_2Se_2(pa)], (b) 2D-[Cd_2Se_2(ba)], and (c) 2D-[Cd_2Se_2(ha)].

which have been verified by both SEM and PXRD methods. Because both würtzite ZnS and ZnSe are thermally metastable, the thermolysis of suitable hybrid compounds may be a promising approach of producing metastable II–VI semiconductor nanomaterials.

2.14.2.3.4 Phase transitions

Some II–VI hybrid semiconductors made of long organic amine molecules exhibit interesting phase-transition phenomena. Two representative examples are 3D-[ZnTe$(bda)_{0.5}$] and 3D-[ZnTe$(hda)_{0.5}$].[206] For both compounds, as the temperature decreases below a certain value, so-called the phase transition temperature, their original α- or δ-phases (observed at room or higher temperature) will change to another phase, namely the γ-phase. The transition temperatures of 3D-[ZnTe$(bda)_{0.5}$] and 3D-[ZnTe$(hda)_{0.5}$] are ∼130 and ∼220 K, respectively. As shown in Figure 33, the organic molecules in both 3D-γ-[ZnTe$(bda)_{0.5}$] and 3D-γ-[ZnTe$(hda)_{0.5}$] possess a peculiar conformation that is quite different from that of the α-phases (Figure 9). Organic molecules in the γ-phase adopt

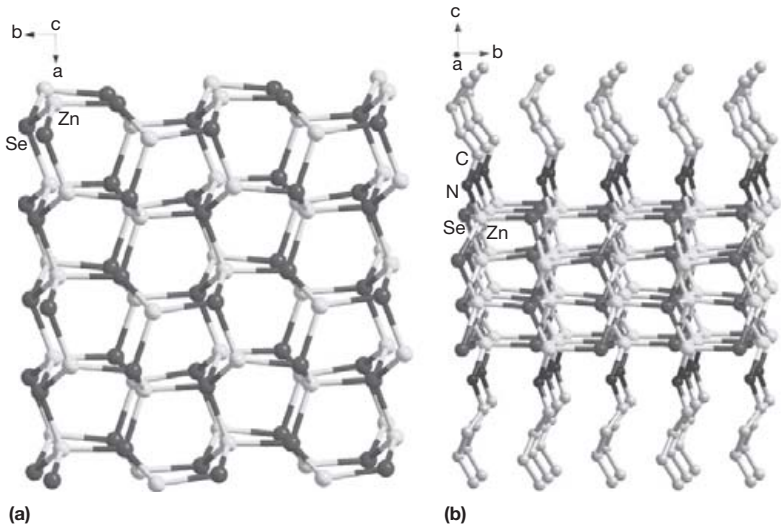

Figure 22 Crystal structure of 2D-[Zn_2Se_2(ba)]: (a) $\{Zn_2Se_2\}_n$ double layer. (b) The overall structure viewing along the *a*-axis. Hydrogen atoms are omitted for clarity.

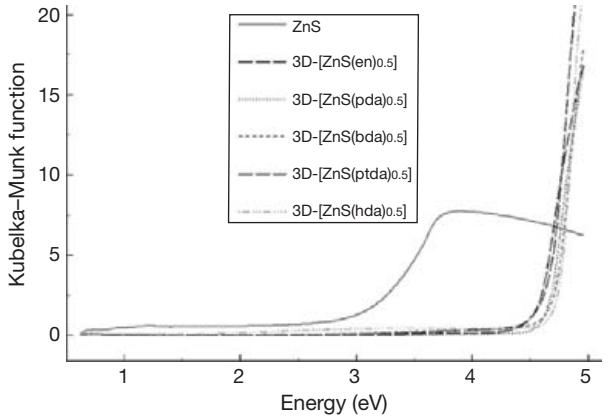

Figure 23 Optical absorption spectra of selected hybrids (i.e., 3D-[ZnS$(L)_{0.5}$], L = en, pda, bda, ptda, hda).

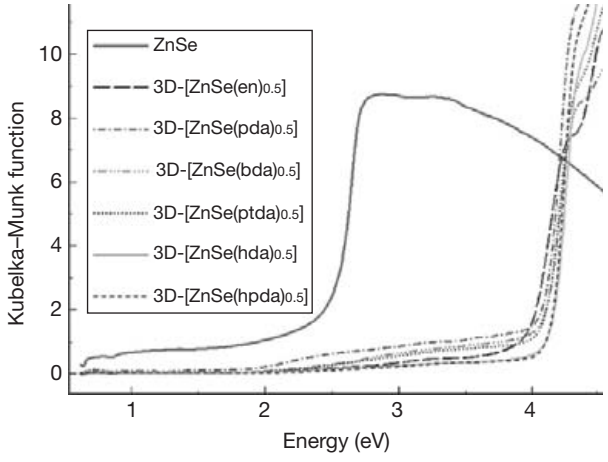

Figure 24 Optical absorption spectra of selected hybrids (i.e., 3D-[ZnSe$(L)_{0.5}$], L = en, pda, bda, ptda, hda, hpda).

the GTG and GTTTG forms (mixture of *trans* (T) and *gauche* (G)) while in the α-phases only *trans* conformers are observed. As a result, the spatial stretching length of the organic molecules as well as the interlayer distance in the α-phase are longer than those in the γ-phase (Table 7). These phase transitions are reversible through an *in situ* lattice-constant measurement of a single crystal undergoing cooling and heating cycles below and above the transition temperature.[206] In addition, Mitzi[267] also reported that 1D-α-[ZnTe(N_2H_4)] can be converted to 2D-[ZnTe(N_2H_4)] via a solid-to-solid phase transition at ~100 °C.

2.14.2.3.5 Thermal expansion

The II–VI hybrid materials also exhibit interesting thermal expansion properties. As is well known, different materials respond to the change of temperature in different ways. Most materials undergo a volume expansion as temperature increases, and such a behavior is characteristic of positive thermal expansion (PTE). Conversely, materials that experience a volume contraction as temperature increases are referred to have negative thermal expansion (NTE), and they are much less common in comparison with the vast majority of PTE materials. Particularly, when a substance does not respond to temperature change (i.e., neither expanding nor contracting in heating or cooling), it is classified as a material of zero (or nearly zero) thermal expansion (ZTE). ZTE materials are of great demand for a variety of applications[279] where constant volume or size is required. However, such materials are extremely rare and only several examples have been reported to date.[280–283] To achieve overall ZTE effect, a great deal of research effort has been focused on making composite materials (e.g., alloys) by mixing PTE and NTE phases.[279,284–287] Nevertheless, such composite materials will unavoidably involve a large number of grain boundaries, which can lead to severe cracks in the materials and impede the ZTE performance.

The modular nature of crystalline II–VI hybrid materials makes them attractive for improved ZTE performance.[205]

Table 8 Bandgap (BG) and blue shift (BS)[a] of selected II–VI hybrids

Compound	*BG (eV)*	*BS (eV)*	*Compound*	*BG (eV)*	*BS (eV)*
3D-[ZnS(en)$_{0.5}$]	4.5	1.3	3D-[MnSe(en)$_{0.5}$]	1.8	0.2
3D-[ZnS(pda)$_{0.5}$]	4.5	1.3	3D-[MnSe(pda)$_{0.5}$]	1.7	0.1
3D-[ZnS(bda)$_{0.5}$]	4.5	1.3	3D-[MnSe(bda)$_{0.5}$]	1.8	0.2
3D-[ZnS(hda)$_{0.5}$]	4.6	1.4			
3D-[ZnS(hpda)$_{0.5}$]	4.6	1.4	2D-[ZnS(N_2H_4)]	4.3	1.2
3D-[ZnS(otda)$_{0.5}$]	4.6	1.4	2D-[ZnS(ma)]	4.5	1.3
3D-[ZnS(dien)$_{0.5}$]	4.6	1.4	2D-[ZnS(pa)]	4.5	1.3
3D-[ZnSe(N_2H_4)$_{0.5}$]	3.7	1.2	2D-[ZnS(ba)]	4.6	1.4
3D-[ZnSe(en)$_{0.5}$]	4.0	1.5	2D-[ZnSe(N_2H_4)]	3.7	1.2
3D-[ZnSe(pda)$_{0.5}$]	3.9	1.4	2D-[ZnSe(ma)]	4.0	1.5
3D-[ZnSe(bda)$_{0.5}$]	4.0	1.5	2D-[ZnSe(ea)]	3.9	1.4
3D-[ZnSe(ptda)$_{0.5}$]	4.0	1.5	2D-[ZnSe(pa)]	4.1	1.6
3D-[ZnSe(hda)$_{0.5}$]	4.1	1.6	2D-[ZnSe(ba)]	4.1	1.6
3D-[ZnSe(hpda)$_{0.5}$]	4.1	1.6	2D-[ZnSe(ha)]	4.1	1.6
3D-[ZnSe(dien)$_{0.5}$]	4.0	1.5	2D-[ZnTe(N_2H_4)]	3.2	1.1
3D-[ZnSe(mxda)$_{0.5}$]	4.0	1.5	2D-[ZnTe(ma)]	3.5	1.4
3D-[ZnTe(N_2H_4)$_{0.5}$]	3.2	1.1			
3D-α-[ZnTe(en)$_{0.5}$]	3.5	1.4	2D-[Zn_2S_2(pa)]	3.9	0.7
3D-β-[ZnTe(en)$_{0.5}$]	3.3	1.2	2D-[Zn_2S_2(ba)]	3.9	0.7
3D-[ZnTe(pda)$_{0.5}$]	3.4	1.3	2D-[Zn_2S_2(aa)]	4.0	0.8
3D-α-[ZnTe(bda)$_{0.5}$]	3.5	1.4	2D-[Zn_2S_2(ha)]	4.0	0.8
3D-α-[ZnTe(hda)$_{0.5}$]	3.5	1.4	2D-[Zn_2Se_2(ea)]	3.5	1.0
			2D-[Zn_2Se_2(pa)]	3.5	1.0
3D-[CdS(en)$_{0.5}$]	3.9	1.6	2D-[Zn_2Se_2(ba)]	3.5	1.0
3D-[CdS(pda)$_{0.5}$]	3.9	1.6	2D-[Zn_2Se_2(aa)]	3.5	1.0
3D-[CdS(bda)$_{0.5}$]	4.0	1.7	2D-[Zn_2Se_2(ha)]	3.5	1.0
3D-[CdS(ptda)$_{0.5}$]	3.9	1.6			
3D-[CdS(hda)$_{0.5}$]	3.9	1.6	2D-[Cd_2S_2(pa)]	2.9	0.6
3D-[CdSe(en)$_{0.5}$]	3.5	2.0	2D-[Cd_2S_2(ba)]	2.9	0.6
3D-[CdSe(pda)$_{0.5}$]	3.5	2.0	2D-[Cd_2S_2(ha)]	2.9	0.6
3D-[CdSe(bda)$_{0.5}$]	3.5	2.0	2D-[Cd_2Se_2(pa)]	2.6	1.1
3D-[CdSe(ptda)$_{0.5}$]	3.5	2.0	2D-[Cd_2Se_2(ba)]	2.6	1.1
3D-[CdSe(hda)$_{0.5}$]	3.5	2.0	2D-[Cd_2Se_2(ha)]	2.6	1.1
3D-[CdTe(en)$_{0.5}$]	3.1	1.7			
3D-[CdTe(pda)$_{0.5}$]	3.1	1.7	1D-[ZnTe(pda)]	3.8	1.7
3D-[CdTe(ptda)$_{0.5}$]	3.1	1.7	1D-[ZnSe(pda)]	4.3	1.8

[a]Estimated bandgaps of II–VI inorganic semiconductors: würtzite CdS 2.3 eV, würtzite CdSe 1.5 eV, CdTe (zinc blende structure) 1.4 eV, ZnS (zinc blende structure) 3.2 eV, ZnSe (zinc blende structure) 2.5 eV, ZnTe (zinc blende structure) 2.1 eV. As an approximation, data for zinc blende structure were used when bandgap values of würtzite structure were not available.

Specifically, the inorganic and organic modules may show different thermal expansion behavior. The II–VI binary compounds are typical PTE materials while the NTE effect has been reported for some amine molecules.[288,289] The incorporation of these two modules into a single-crystalline structure allows the compensation of PTE and NTE generated by the two components. In doing so, the grain boundary problem associated with the composite materials is entirely eliminated. It is interesting to note that as freestanding molecules, a number of amine molecules display the PTE effect, while all of them show NTE behavior when embedded in the hybrid structures. The extent of NTE increases as the length of the organic molecule increases. As a result, the thermal expansion of the hybrid structures can be readily tuned by appropriate combination of inorganic and organic components with suitable length and composition.

The thermal expansion behaviors of five selected hybrid materials are illustrated in Figure 34. These hybrids are 3D-α-[ZnTe(N_2H_4)$_{0.5}$] (**a**), 3D-α-[ZnTe(en)$_{0.5}$] (**b**), 3D-α-[ZnTe(pda)$_{0.5}$] (**c**), 3D-α-[ZnTe(bda)$_{0.5}$] (**d**), and 3D-α-[ZnTe(ptda)$_{0.5}$] (**e**), respectively. All five structures contain $\{ZnTe\}_n$ single atomic layers, which are interconnected by diamine molecules via coordination bonds between Zn and N atoms. The changes in lattice parameters of compound **b** are plotted in Figure 34(a). The two short axes (L_1 and L_2, parallel to $\{ZnTe\}_n$ layers) increase as temperature rises. This PTE behavior is also observed for other four hybrid compounds. The thermal expansion coefficients (α) of **a**–**b** are in the range of $0.9–1.5 \times 10^{-5}\,K^{-1}$ (for L_1), and $1.4–2.9 \times 10^{-5}\,K^{-1}$ (for L_2), respectively. From Figure 34(b) one sees that the PTE effect (represented by the changes in L_2) generally decreases as the number of amine carbon atoms (n) increases from **a** to **b**. The long axis L_3, which is perpendicular to the $\{ZnTe\}_n$ layers, shows a much smaller PTE for compound **a** (with the shortest diamine, $n=0$), whereas for other compounds, L_3 exhibits an increasing NTE effect as diamine molecules get longer (Figure 34(c)). Individual contributions of inorganic and organic components to L_3 are plotted in Figure 34(d) for

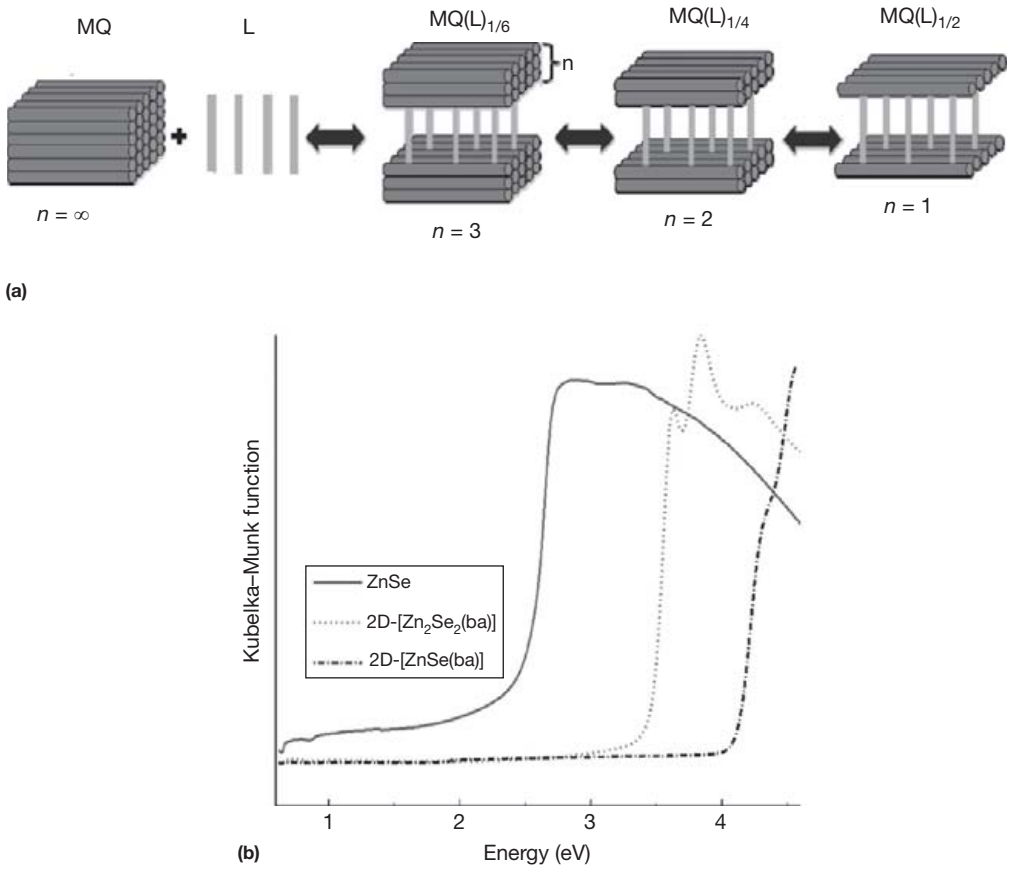

Figure 25 (a) The schematic plot illustrating the correlation between the layer thickness (n) and bandgap for 3D hybrid structures (i.e., 3D-[$MQ(L)_{0.5}$]). (b) Optical absorption spectra of ZnSe (zinc blende type), single-layered 2D-[(ZnSe)(ba)], and double-layered 2D-[((Zn_2Se_2)(ba)].

Table 9 Calculation parameters and results of selected II–VI hybrids

Compound	*Parameters*			*Results*				
	Monkhorst–Pack k-point set	*Cutoff energy (eV)*	*Empty bands*	*BG (eV) cal.*	*BG (eV) exp.*	*BS (eV) cal.*	*BS (eV) exp.*	*BG type*
3D-α-[$ZnTe(en)_{0.5}$]	$4\times4\times1$	310	12	2.707	3.5	1.252	1.32	Direct
3D-β-[$ZnTe(en)_{0.5}$]	$4\times4\times6$	310	12	2.345	3.3	1.226	1.2	Direct
3D-[$ZnTe(pda)_{0.5}$]	$4\times4\times4$	310	12	2.737	3.4	1.282	1.22	Direct
3D-[$CdSe(en)_{0.5}$]	$4\times4\times2$	280	12	2.600	3.5	1.849	2	Direct
2D-β -[$ZnTe(N_2H_4)$]	$4\times4\times3$	310	12	2.329	3.2	1.21	1.1	Direct
2D-α-[ZnTe(ma)]	$3\times4\times1$	310	12	2.791	3.5	1.336	1.32	Direct
1D-[ZnTe(pda)]	$3\times4\times2$	310	12	2.951	3.8	1.496	1.62	Indirect/direct
1D-α-[$ZnTe(N_2H_4)_2$]	$4\times2\times3$	310	12	2.974	3.8	1.519	1.62	Indirect/direct
ZnTe-W	$7\times7\times4$	310	12	1.455	2.18	N/A	N/A	Direct
ZnTe-ZB	$7\times7\times7$	310	12	1.119	2.1	N/A	N/A	Direct
CdSe-W	$7\times7\times4$	260	12	0.751	1.5	N/A	N/A	Direct

a ($n=0$) and **c** ($n=3$). The inorganic motifs in both compounds exhibit a comparable PTE effect, while the organic components in **c** exhibit a significantly more prominent NTE than those in **a**, giving rise to an overall PTE and NTE for **a** and **c**, respectively.

The thermal expansion behavior of 3D-β-[$ZnTe(en)_{0.5}$] has also been analyzed in powder form.[290] The phonon spectrum of this compound is calculated using a linear response theory. The calculation results reveal that a number of transverse and transverse–longitudinal (mixed) modes can be excited in a temperature range between 4 and 400 K. The frequencies are in the similar region of the transverse modes found in other NTE materials.[291,292] In addition, Raman analysis has verified that the frequencies experience red shifts upon cooling (a signature of the transverse mode).

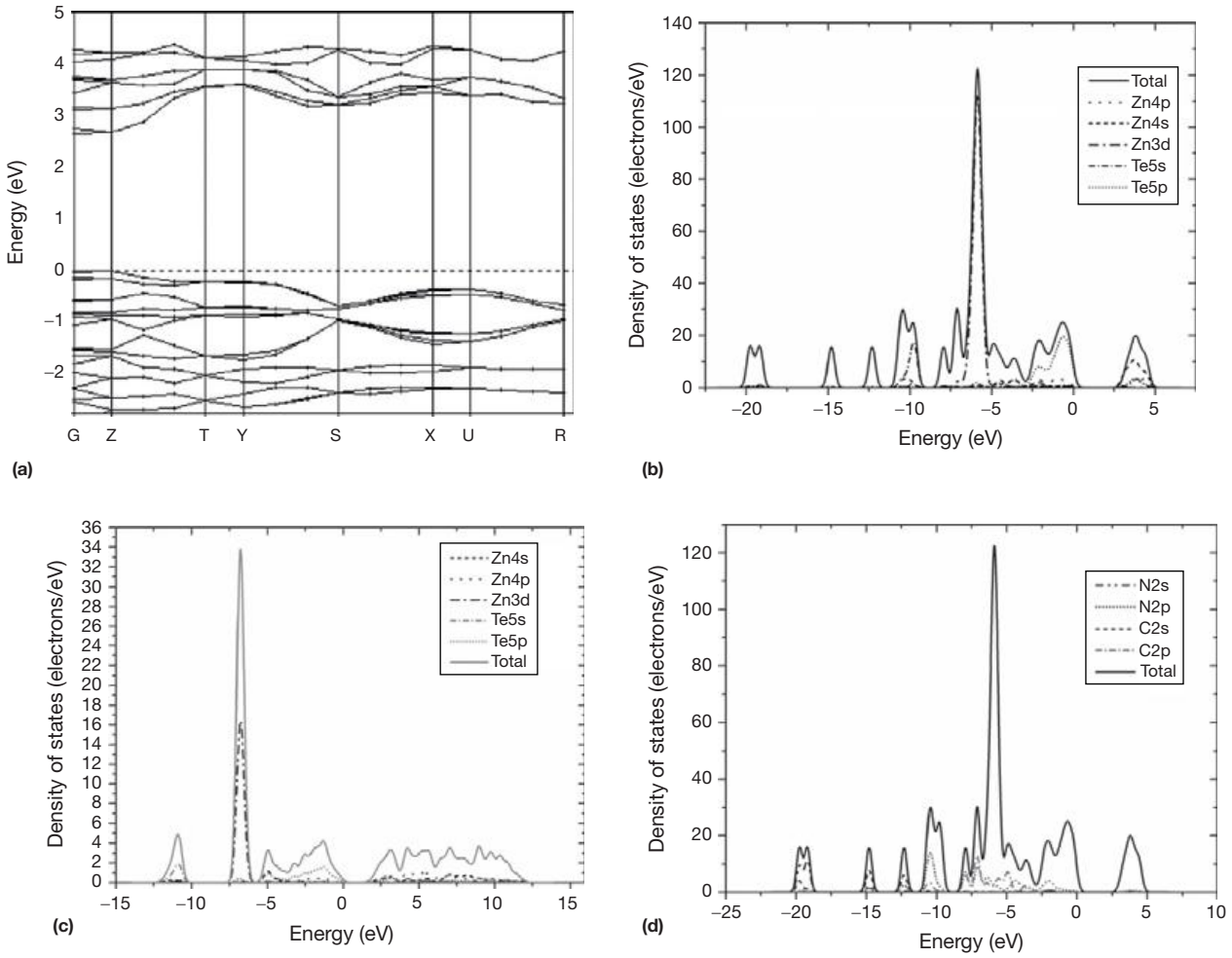

Figure 26 (a) Band structure of 3D-α-[ZnTe(en)$_{0.5}$]. (b) and (c) Total and partial DOS of 3D-α-[ZnTe(en)$_{0.5}$]. (d) Total and partial DOS of würtzite ZnTe.

2.14.2.3.6 Photoluminescence and white-light emission

As one of the most promising energy-saving lighting technologies, solid-state lighting (SSL) is evolving very rapidly during recent years. By utilizing semiconductor materials, SSL devices have a higher efficiency in converting electricity to light and they last for a longer time than conventional lighting sources. It has been estimated that by 2020, SSL applications would contribute up to 50% reduction of global energy consumption for lighting.[293] Additionally, as it can make direct use of solar power, a renewable energy source, SSL technology will considerably reduce the greenhouse gas accumulation and contribute to a cleaner environment.

Two main branches of SSL technology are light-emitting diode (LED) and organic light-emitting diode (OLED), both of which have attracted tremendous research attention in recent decades. White-light LEDs (or OLEDs) are most demanding for conventional lighting applications. Generally, they are fabricated by phosphor conversion,[294] in which white light is generated by a blue or near-UV LED coated with a yellow or a multichromatic phosphor. Another approach is by the combination of monochromatic LEDs (i.e., red, green, and blue LEDs). However, both fabrication methods involve complicated mixing and doping processes that are associated with problems such as self-absorption, nonradiative carrier loss, and low light-capture efficiency.[295–297] Such problems will significantly reduce the lighting efficiency of the device and thus hinder the widespread utility of SSL technology.

An interesting discovery in 2005 showed that the very small CdSe nanocrystals could directly emit white light without involving a doping process.[154] The emission of these CdSe nanocrystals (~1.5 nm) is very broad and covers the entire visible spectrum. This phenomenon is owing to the very high surface-to-volume ratio of the CdSe nanocrystals. In such a case, a large number of midgap surface sites are generated and the photogenerated holes are trapped in these midgap states and combined with electrons before returning back to the ground state through a nonradiative pathway.[154] However, due to the weak correlations between the nanoparticles, these nanocrystals are practically unable to achieve high conductivity and mobility required for LEDs.

The II–VI-based hybrid semiconductors may have potential for use in white-light LEDs.[298,299] In 2008, we reported the first semiconductor bulk material 2D-[Cd_2S_2(ba)] (**Figure 35(a)**)

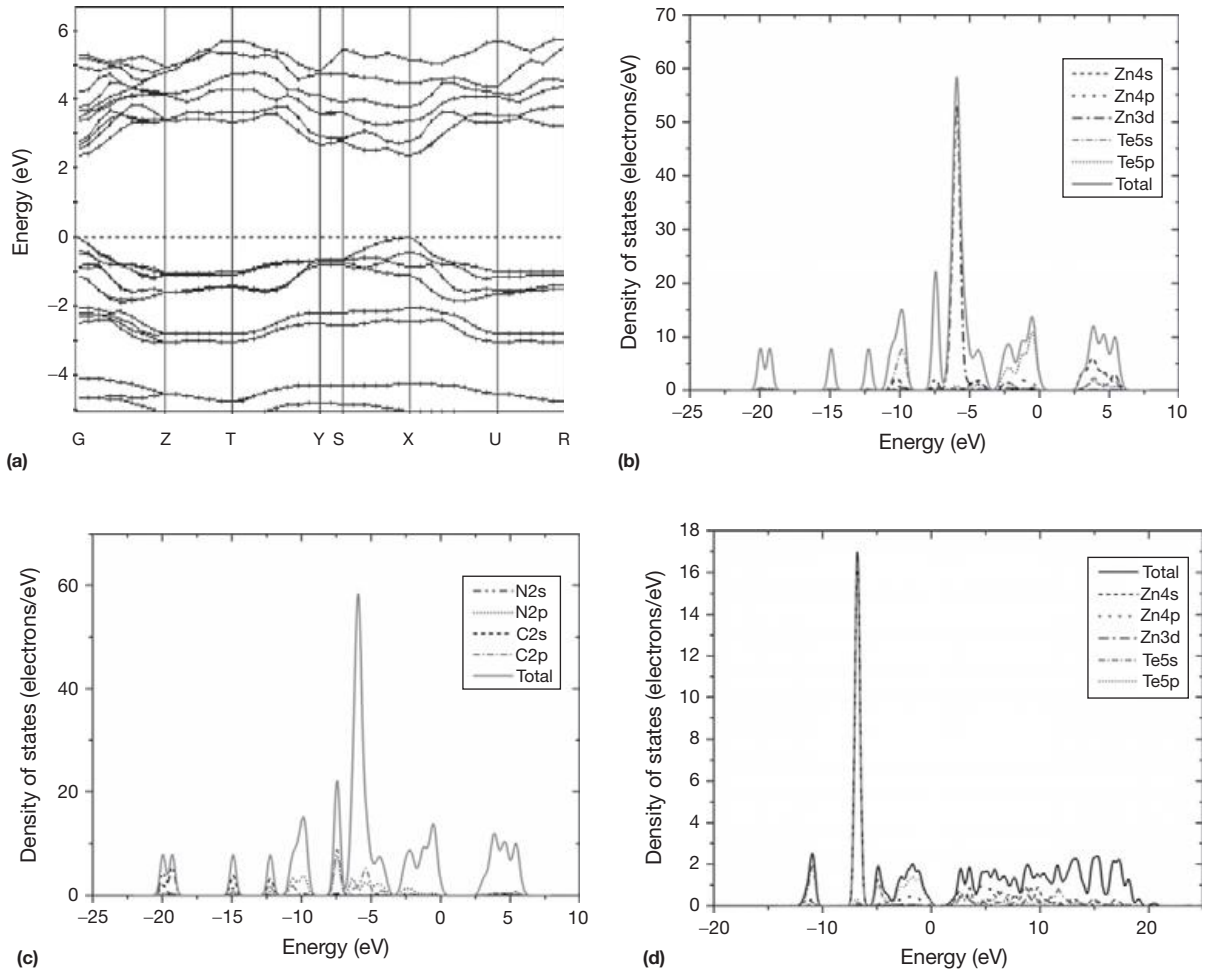

Figure 27 (a) Band structure of 3D-β-[ZnTe(en)$_{0.5}$]. (b) and (c) Total and partial DOS of 3D-β-[ZnTe(en)$_{0.5}$]. (d) Total and partial DOS of zinc blende ZnTe.

that generates white light directly.[298] The photoluminescent emission of this material spans over the full region of the visible spectrum (**Figure 35(b)**), which makes it a characteristic and well-balanced white-light emission. As a well-known strong luminescent center, Mn^{2+} ions are also used to further enhance the emission intensity.[266,300,301] Showing in **Figure 36** are white-light LEDs fabricated by using 2D-[Cd_2S_2(ba)] and Mn-doped 2D-[Cd_2S_2(ba)] samples as phosphors. The chromaticity coordinates of these white-light LEDs are located well within the white region of the International Commission on Illumination (CIE) 1931 color space chromaticity diagram.[298,302] The internal quantum yield (QY) of 2D-[Cd_2S_2(ba)] type structures is ~4–5%.[298] Much higher QY (~25%) has been achieved for 2D-[Zn_2S_2(L)] type compounds.[303]

Although the white-light emission found in II–VI hybrids is similar to what has been elucidated for CdSe nanocrystals,[304] the hybrid materials possess some exclusive advantages that make them more promising. First of all, because they comprise infinite and perfectly ordered II–VI modules, high carrier conductivity and mobility are anticipated in hybrid structures and they may become suitable candidates for single-material-based active layer in high-efficiency white-light LED chips. Second, the hybrid materials are free of issues related to the particle size or size distribution that must be addressed in the cases of nanocrystals. Furthermore, the structures and optical properties of the hybrids can be tuned systematically. Finally, since the hybrid materials can be readily processed in bulk form, they are likely more favorable in industrial device-fabrication processes.

2.14.2.3.7 Mechanical properties

Despite the fact that organic molecules in II–VI hybrid compounds make little effect on the bandgap and related electronic and optical properties, they play a crucial role in other functionality and behaviors. One of the most attractive features of the hybrid structure is that by combination of two distinct components into a single-crystal lattice, multiple important and useful properties pertinent to each of the two components can be integrated into the resultant material. Thus, the II–VI hybrid compounds are substantially lighter and more flexible than their parent II–VI binaries because of the incorporation of organic molecules. Such properties would profoundly contribute to the mechanical behavior of the II–VI hybrids.

The mechanic strength of some selected II–VI hybrid compounds is tested by typical stress–strain measurements, performed on pellet samples prepared from polycrystalline

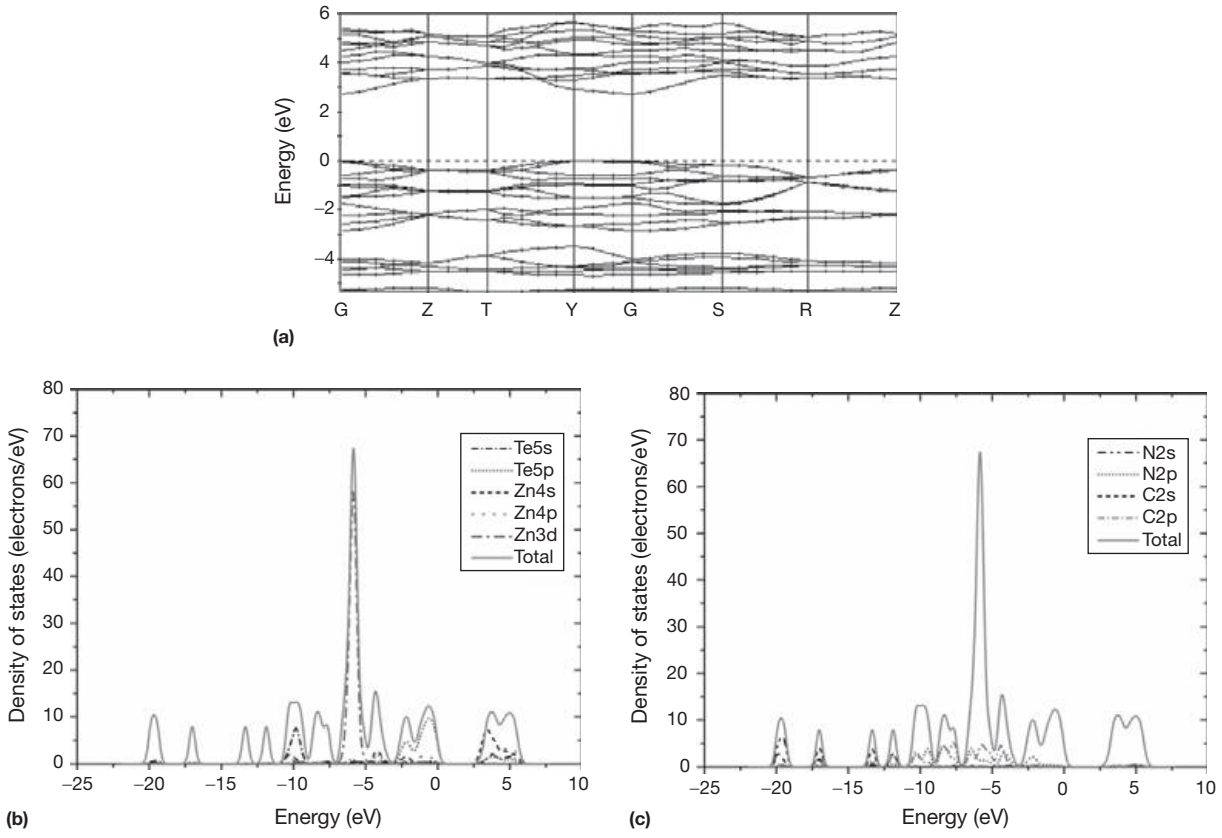

Figure 28 (a) Band structure of 3D-[ZnTe(pda)$_{0.5}$]. (b) and (c) Total and partial DOS of 3D-[ZnTe(pda)$_{0.5}$].

powders.[206] The stress–strain profiles of 3D-α-[ZnTe(L)$_{0.5}$] (L = N_2H_4, en, pda, bda, and hda) and three reference materials prepared in the same manner (ZnTe, pentacene, and polystyrene) are shown in Figure 37. The data at the low-pressure region show that the hybrids with shorter organic molecules exhibit similar mechanical behavior to that of pentacene, while those containing longer organic amines are analogous to polystyrene. 3D-α-[ZnTe(hda)$_{0.5}$], having the longest organic amine molecule (i.e., hda), possesses a larger strain than that of polystyrene under the same stress force. Furthermore, the relatively high flexibility of the hybrid materials is evidenced by its capability of 'bending,' as shown in the image of freestanding film sample (Figure 38).

2.14.2.3.8 Thermal conductivity

Another interesting property of II–VI hybrids is their thermal conductivity.[206] The results of thermal conductivity measurements for the 3D-α-[ZnTe(L)$_{0.5}$] (L = N_2H_4, en, and pda) structures and the reference material ZnTe are plotted in Figure 39. Based on the thermal conductivity data, it is clear that the thermal conductivity of all these hybrids is reduced to a large extent in comparison with that of the parent compound ZnTe. When the length of the organic molecules increases from N_2H_4 to pda, the unit cell of the hybrid compounds expands accordingly. A monotonic increase in the specific heat capacity is observed in Figure 39. Such an increase is coupled with a slight decrease in the thermal diffusivity, which leads to a net increase in the thermal conductivity as the temperature rises.

2.14.2.3.9 Magnetic properties

Magnetically substituted hybrid semiconductors are obtained by incorporating magnetic elements (e.g., Mn, Fe, and Co) into the host lattices of nonmagnetic hybrids (such as 3D-[ZnSe(L)$_{0.5}$], 3D-[CdSe(L)$_{0.5}$], 2D-[ZnSe(ba)], and 2D-[Zn_2Se_2(ba)]) without changing their crystal structures.[200,266,305–308] Analogues to the host hybrids, the magnetically substituted hybrids also manifest a large blue shift in their absorption spectra, and the shift extent depends on the amount of magnetic substituents.[200]

Substitution of magnetic elements into nonmagnetic hybrids introduces large enhancement in the magnetic moments. The magnetic behavior of these substituted hybrids is characteristic of paramagnetism with antiferromagnetic coupling between the Mn^{2+} cations, evident from the continuous decrease of χT values as temperature is lowered. More interestingly, these values decrease as the concentration of Mn^{2+} increases over the entire temperature range selected in the study (Figure 40). In addition, the antiferromagnetic interaction between the Mn^{2+} ions decreases as the length of organic diamines increases. Such an interaction is also affected by the inorganic II–VI arrays. This is supported by the fact that Mn–Mn interaction in the single atomic-layered 2D-[$Zn_{1-x}Mn_xSe$(ba)] is stronger than that found in the double-layered structure 2D-[$Zn_{2-2x}Mn_{2x}Se_2$(ba)].[308]

2.14.2.3.10 Other properties

In addition to the findings described above, studies have also been carried out to investigate a number of other properties for the hybrid materials. For example, II–VI hybrid structures have

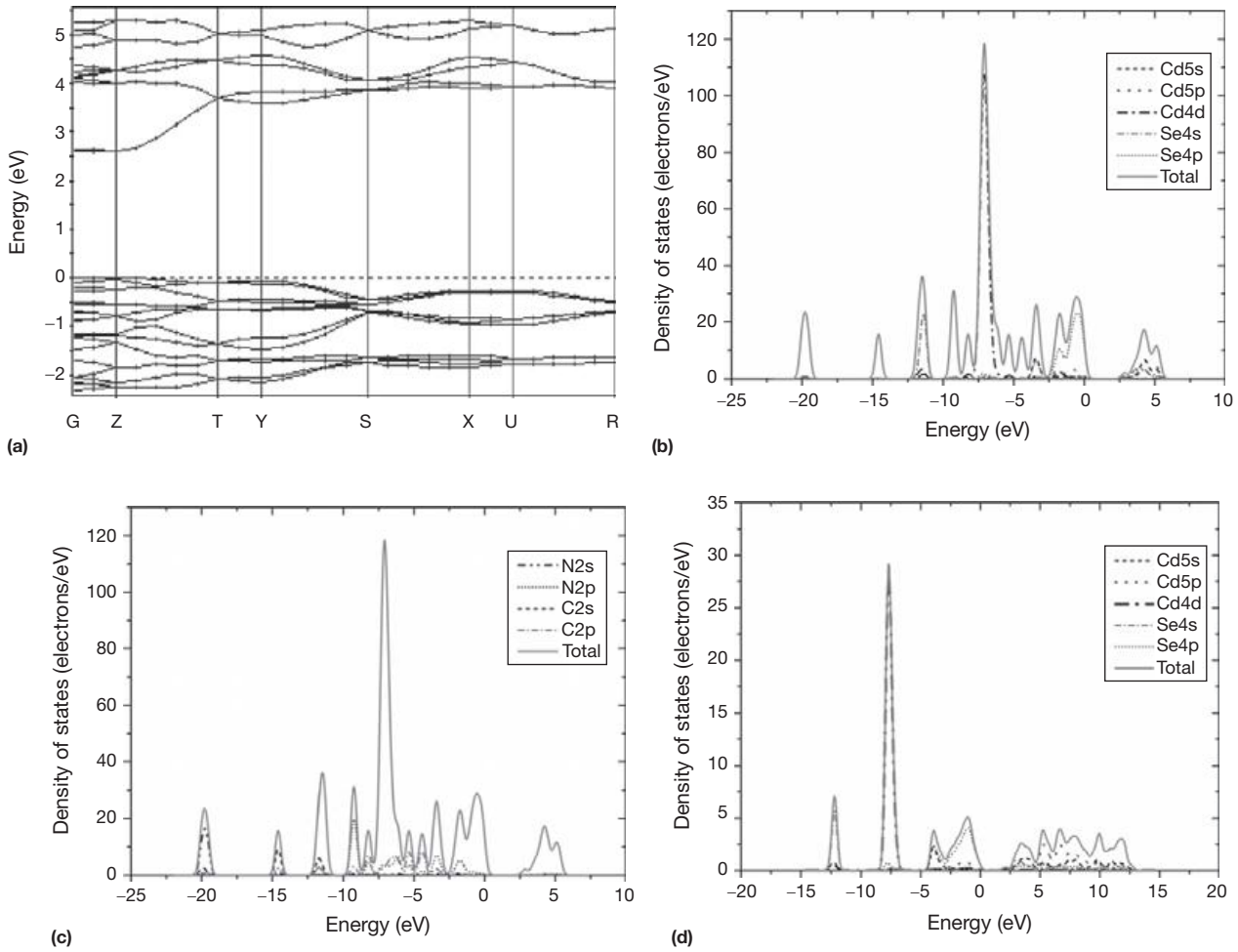

Figure 29 (a) Band structure of 3D-[CdSe(en)$_{0.5}$]. (b) and (c) Total and partial DOS of 3D-[CdSe(en)$_{0.5}$]. (d) Total and partial DOS of würtzite CdSe.

commonly been used as precursors to synthesize inorganic II–VI nanomaterials with appropriate morphology and size. There are a number of publications exemplifying the research progress in this area.[265,309–318] Through the thermolysis of 3D-[ZnS(en)$_{0.5}$], Yu and coworkers[319] fabricated the nanosheets of würtzite ZnS, while the würtzite ZnS nanorods were also obtained by Wu et al.[312] In addition, Li and coworkers[320] synthesized the nanofibers of würtzite ZnS and ZnSe through solvothermal decomposition of [ZnQ(N$_2$H$_4$)$_x$] (Q = S, Se) in ethanol solution. Apart from the II–VI inorganic phases, the hybrids themselves could be fabricated into nanomaterials with different morphology and size.[226,314,316–318,321–323] For instance, uniform 3D-[ZnSe(dien)$_{0.5}$] nanobelts were produced by Yao et al.[324] through the control of the solvent composition. Mitzi and coworkers[267,325,326] reported that the low-dimensional ZnTe-based hybrids which can be dissolved in hydrazine are promising alternative precursors to fabricate thin films via a solution-deposition process. This approach has a great potential to afford low-cost and high-efficiency devices for the PV industry.

The absorption and emission spectra of polycrystalline 3D-[CdSe(hda)$_{0.5}$] and 3D-[CdSe(en)$_{0.5}$] have been studied by Qian et al.[266] at room temperature. For 3D-[CdSe(hda)$_{0.5}$], it has a sharp emission at 362 nm (3.43 eV) with full width at half-maximum of 0.177 eV while absorbing strongly at 354 nm (3.5 eV). The Stokes shift is 0.07 eV. These findings verified that for II–VI hybrids, the band-edge absorption and emission are originated from the inorganic II–VI components and are irrelevant to the length of amine molecules. In addition to these compounds, photoluminescence studies are also carried out for several 2D and 3D sulfur- or selenium-based hybrid structures.[229,319,323,324] Notably, some hybrid structures may be good candidates for photocatalysis. For instance, both 3D-[ZnS(en)$_{0.5}$] and 3D-[ZnS(pda)$_{0.5}$] have been used in the photocatalytic degradation of selected dyes.[327]

Fu and coworkers[328] investigated the behavior of 3D-[ZnSe(en)$_{0.5}$] under hydrostatic pressure by using a first-principles pseudopotential method with mixed-basis set. Surprisingly different from the general assumption, the bonds of inorganic {ZnSe}$_n$ layers rather than organic linkers are predominantly and highly compressed under the pressure. Moreover, the bandgap as well as other properties of the hybrid structures exhibit unusual pressure dependence. Moon and coworkers[329] also employed the first-principles method in the study of structural stability, electronic properties, and total energy differences of en-based hybrids. The calculation results show that en molecules with different conformations give rise to two

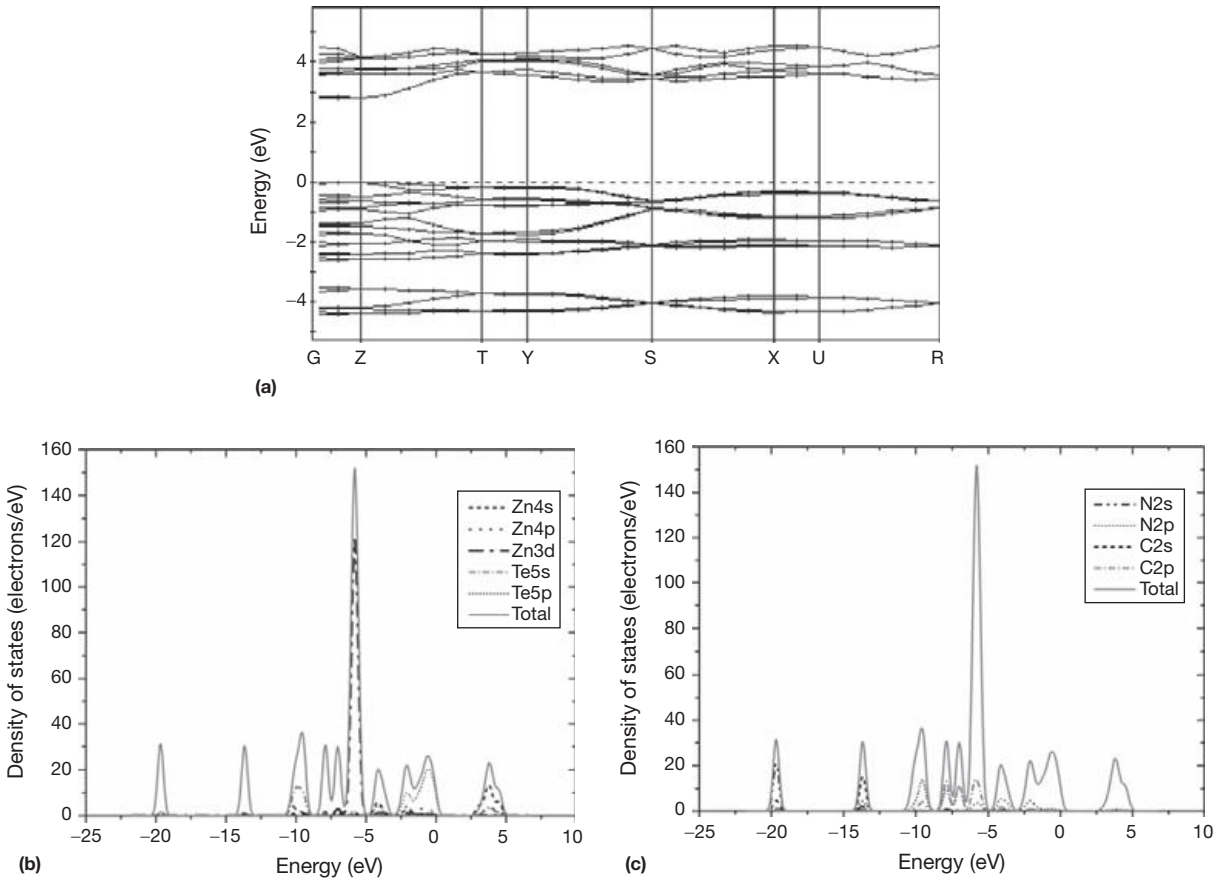

Figure 30 (a) Band structure of 2D-[ZnTe(ma)]. (b) and (c) Total and partial DOS of 2D-[ZnTe(ma)].

polymorphs for hybrid structures, that is, α_I-phase and α_{II}-phase. The en molecules adopt the GTG conformation for the latter and TTT conformation for the former, respectively (T = *trans*, G = *gauche*). In addition, it has been found that the α_I-phase is the most stable phase while the stability of the α_{II}-phase goes down as the lattice constants of the hybrids decrease. The theoretical study also reveals that the kinetic effect plays a very important role in the formation of different hybrid phases.

Under appropriate reaction conditions, single crystals of ZnTe-based hybrids can be produced in fairly large size (1–2 mm), which allows the measurement of polarization dependence directly performed on single-crystal samples. Therefore, Raman analysis has been carried out on single crystal samples of ZnTe-based hybrids at room temperature.[204] The obtained spectra show multiple sharp phonon modes at frequencies that are different from those of the bulk ZnTe, which would be probably ascribed to the band folding of the semiconductor-related modes. By varying the structural dimensionality of ZnTe-based hybrids (i.e., from 3D to 1D), different vibrational signatures are clearly observed in their Raman spectra. In addition, Raman analysis also demonstrates that the ZnTe-based hybrids possess high surface quality and high crystallinity. Furthermore, polarized photoluminescence, absorption, and reflectance properties are also investigated at different temperatures on single crystals of 1D-ZnTe(pda) and 3D-β-[ZnTe(en)$_{0.5}$]. The experimental results indicate that at both low temperature and room temperature, these hybrid materials show significantly enhanced band-edge absorption, huge confinement effect, strong exciton binding energy, and large anisotropic refractive index.[278,330] For 3D-β-[ZnTe(en)$_{0.5}$], the free exciton–polariton emission at the fundamental band edge has been observed for the first time at both low temperature and room temperature.

2.14.3 III–VI-Based Inorganic–Organic Hybrid Semiconductor Nanostructures

Most of the II–VI hybrid semiconductors possess large bandgaps (>3.0 eV, see **Table 9**) and are therefore not suitable for utilization as active layers in PV devices. To reduce the bandgaps, new hybrid nanostructures based on III–VI semiconductors are being developed. The III–VI compounds are generally direct bandgap semiconductors and have much lower bandgaps than those of II–VI binaries. Among all the III–VI semiconductors, In_2Te_3 has the smallest direct bandgap (~1.0 eV) so that it could be an excellent candidate for PV applications. By applying the design strategy similar to the construction of II–VI hybrids, an unprecedented zero-dimensional (0D) hybrid structure $In_8Te_{12}(trien)_4$ (trien = triethylenetetramine) has been successfully prepared through a solvothermal synthesis.[331]

0D-[$In_8Te_{12}(trien)_4$] crystallizes in the *C*2/*c* space group. The structure comprises a {In_8Te_{12}} cluster coordinated to

Table 10 TGA data of selected II–VI hybrid semiconductors

Compound	*Exp. weight loss (%)*	*Calcd. weight loss (%)*	T_s[a] *(°C)*	T_f[b] *(°C)*	T_d[c] *(°C)*	*Residual*
3D-α-[ZnS(en)$_{0.5}$]	22.9	23.6	260	>400	359	ZnS(W[d])
3D-[ZnS(pda)$_{0.5}$]	30.3	27.6	180	420	348	ZnS(W)
3D-[ZnS(bda)$_{0.5}$]	31.0	31.1	200	420	352	ZnS(W)
3D-[ZnS(ptda)$_{0.5}$]	36.2	34.4	100	420	314	ZnS(W)
3D-[ZnS(hda)$_{0.5}$]	37.9	37.4	220	420	344	ZnS(W)
3D-α-[ZnSe(en)$_{0.5}$]	17.7	17.2	250	410	326	ZnSe(W)
3D-α-[ZnSe(pda)$_{0.5}$]	22.0	20.4	250	410	326	ZnSe(W)
3D-α-[ZnSe(bda)$_{0.5}$]	24.2	23.4	230	420	353	ZnSe(W)
3D-α-[ZnSe(ptda)$_{0.5}$]	28.1	26.1	200	420	312	ZnSe(W)
3D-α-[ZnSe(hda)$_{0.5}$]	26.8	28.7	120	410	353	ZnSe(W)
3D-α-[ZnSe(hpda)$_{0.5}$]	32.0	31.1	200	420	325	ZnSe(W)
3D-α-[ZnTe(en)$_{0.5}$]	13.7	13.5	200	400	299	ZnTe(ZB[e] + W) + Te
3D-β-[ZnTe(en)$_{0.5}$]	13.9	13.5	200	400	290	ZnTe(ZB)
3D-α-[ZnTe(pda)$_{0.5}$]	14.4	16.1	200	400	318	ZnTe(W) + Te
3D-[CdSe(en)$_{0.5}$]	14.3	13.6	180	320	244	CdSe(W)
3D-[CdSe(pda)$_{0.5}$]	16.5	16.2	150	350	247	CdSe(W)
3D-[CdTe(en)$_{0.5}$]	9.1	11.1	180	>420	238	CdTe(ZB) ≫ Te
2D-[ZnS(pa)]	34.7	37.76	80	400	174	ZnS(W)
2D-[ZnS(ba)]	43.82	42.87	50	420	173	ZnS(W)
2D-[ZnS(ha)]	53.15	50.90	50	400	182	ZnS(W)
2D-[ZnSe(ma)]	18.14	17.7	130	360	200	ZnSe(W)
2D-[ZnSe(ea)]	23.45	23.80	130	360	197	ZnSe(W)
2D-[ZnSe(pa)]	29.32	29.05	130	360	194	ZnSe(W)
2D-[ZnSe(ba)]	32.88	33.63	130	360	200	ZnSe(W)
2D-[ZnSe(ha)]	40.73	41.17	130	400	215	ZnSe(W)
2D-[Zn_2S_2(pa)]	26.93	23.26	RT	420	156/263	ZnS(W)
2D-[Zn_2S_2(ba)]	27.35	27.28	RT	420	187/248	ZnS(W)
2D-[Zn_2S_2(ha)]	35.58	34.14	RT	420	145/238	ZnS(W)
2D-[Zn_2Se_2(pa)]	18.68	16.99	100	400	180.562	ZnSe(W)
2D-[Zn_2Se_2(ba)]	21.43	20.21	100	400	180/257/315	ZnSe(W)
2D-[Cd_2S_2(pa)]	18.49	16.98	80	420	201	CdS(W)
2D-[Cd_2Se_2(pa)]	12.55	13.38	100	300	181	CdSe(W)
2D-[Cd_2Se_2(ba)]	16.23	16.03	100	300	193	CdSe(W)
2D-[Cd_2Se_2(ha)]	22.15	20.69	100	300	214	CdSe(W)
1D-[ZnSe(pda)]	32.90	33.9	120	410	240/314	ZnSe(W)
1D-[ZnTe(pda)]	27.83	27.8	150	360	223/300	ZnTe(ZB ≫ W)

[a] T_s is the temperature at which the hybrid compound begins the weight loss.
[b] T_f is the temperature at which the hybrid compound completes the weight loss.
[c] T_d is the decomposition temperature.
[d] W, würtzite.
[e] ZB, zinc blende.

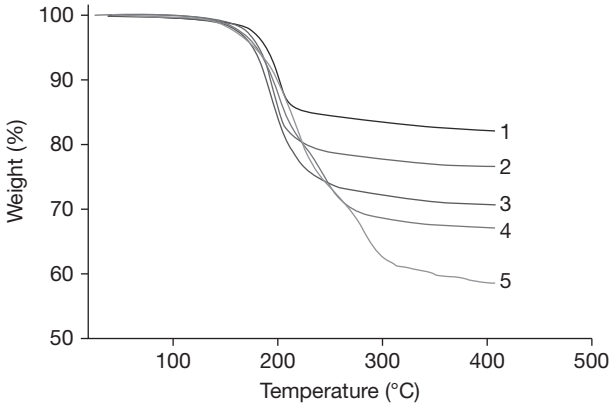

Figure 31 TGA profiles of 2D-[ZnSe(ma)] (**1**), 2D-[ZnSe(ea)] (**2**) 2D-[ZnSe(pa)] (**3**), 2D-[ZnSe(ba)] (**4**), and 2D-[ZnSe(ha)] (**5**).

four trien molecules (Figure 41). Half of the indium sites have a four-coordinated tetrahedral {$InTe_4$} geometry and another half adopts a distorted square-pyramidal {InN_3Te_2} coordination. The overall packing structure is shown in Figure 41(b) as viewed down the *b*-axis. In this structure, the {In_8Te_{12}} cluster can be described as a small building unit cut from the In_2Te_3 parent structure (α-phase) with its composition, bonds, charge, and crystal structure little perturbed. Thus, the semiconductor properties of the parent In_2Te_3 can be well retained in this hybrid structure, and this has been confirmed by the theoretical calculations using CASTEP.[331] Similar to the II–VI hybrid semiconductors, the insulating organic molecules in 0D-[In_8Te_{12}(trien)$_4$] are also dual functional. They act as passivating as well as structure-directing agents. Structure-induced QCE is, therefore, anticipated in the resultant crystalline hybrid structure 0D-[In_8Te_{12}(trien)$_4$]. The system can be

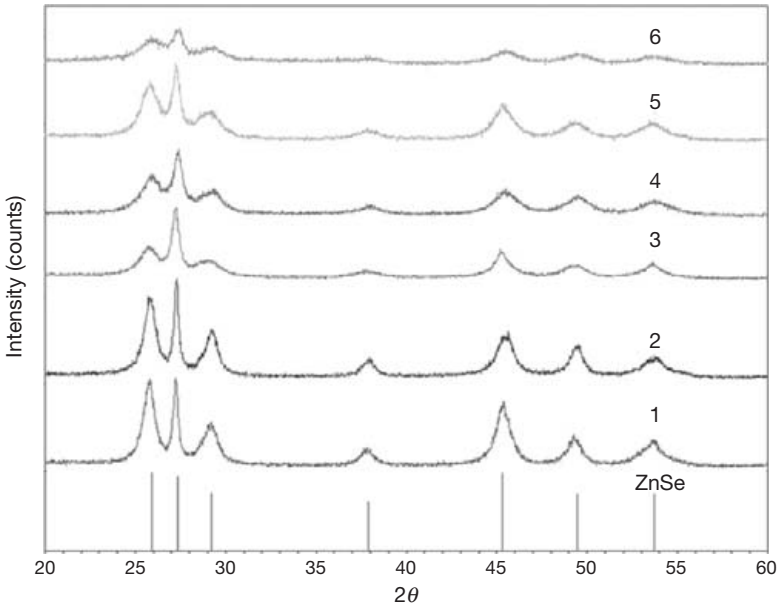

Figure 32 PXRD patterns of post-TGA residuals for 3D-$[ZnSe(en)_{0.5}]$ (**1**), 3D-$[ZnSe(pda)_{0.5}]$ (**2**), 3D-$[ZnSe(bda)_{0.5}]$ (**3**), 3D-$[ZnSe(ptda)_{0.5}]$ (**4**), 3D-$[ZnSe(hda)_{0.5}]$ (**5**), and 3D-$[ZnSe(hpda)_{0.5}]$ (**6**). Simulated PXRD pattern of bulk ZnSe (würtzite type) is also included for comparison.

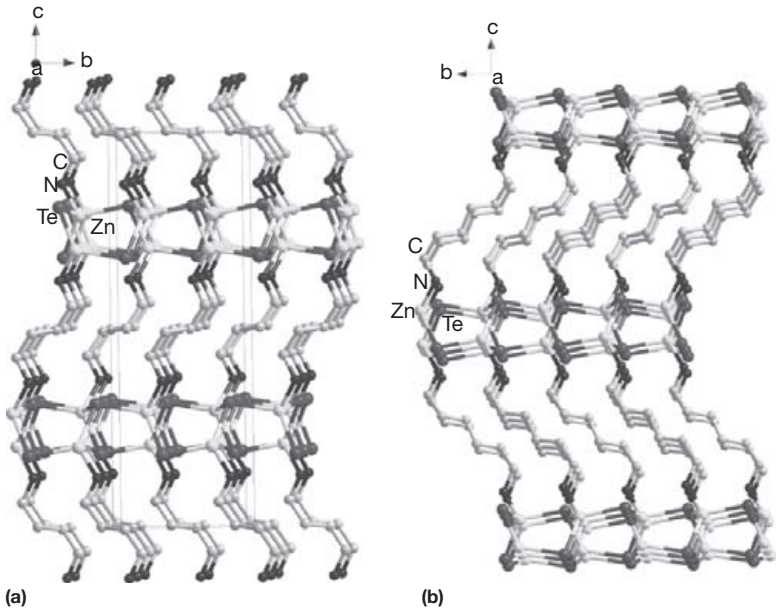

Figure 33 Views of 3D-γ-$[ZnTe(L)_{0.5}]$ structures: (a) L = bda and (b) L = hda.

regarded as perfectly ordered QDs made of In_2Te_3 semiconductor clusters. To the best of our knowledge, this is the first example of colloidal QDs that crystallize into a periodic crystal lattice.

The optical absorption spectra of 0D-$[In_8Te_{12}(trien)_4]$ and inorganic In_2Te_3 (α-phase) are shown in Figure 42. Comparing with In_2Te_3, the absorption edge of 0D-$[In_8Te_{12}(trien)_4]$ exhibits a large blue shift (~2.2 eV), and its absorption intensity is significantly increased. The size of the $\{In_8Te_{12}\}$ cluster is $\sim 1.02 \times 1.02 \times 0.71$ nm, which is much smaller than the average dimensions of known colloidal QDs. Therefore, the extent of QCE of this hybrid nanostructure is evidently much stronger than that of the smallest QDs (~1 eV) reported to date.[154,207–210] In comparison with the perfectly ordered quantum wells (i.e., 2D MQ layers) and quantum wires (i.e., 1D MQ chains) of II–VI hybrids confined in one and two dimension (s), it is clear that In_8Te_{12} QDs in 0D-$[In_8Te_{12}(trien)_4]$ are confined in all three dimensions. As a result, 0D-$[In_8Te_{12}(trien)_4]$ offers a larger blue shift than its II–VI counterparts (~0.7–2.0 eV).

Moreover, this compound has a relatively high thermal stability (up to 180 °C) and can be readily dispersed into suspendable nanoparticles through an ultrasonication

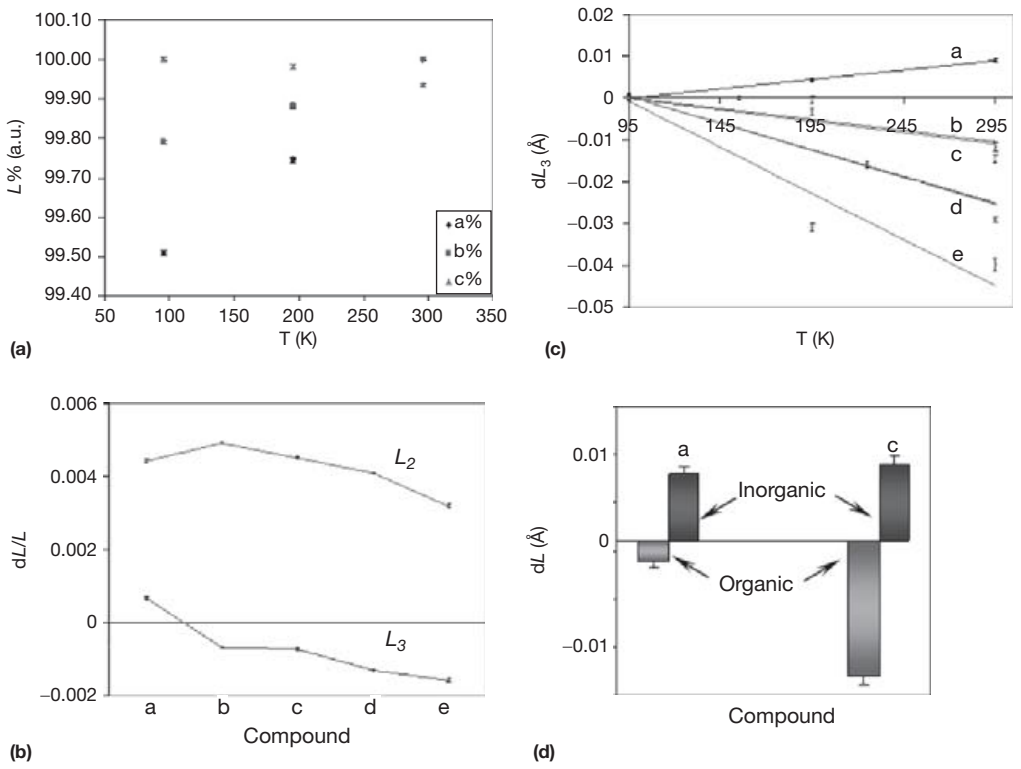

Figure 34 (a) Relative changes of the unit cell lengths for compound **b** (a = L_2, b = L_1, c = L_3) from 95 to 295 K. (b) Normalized changes in L_2 and L_3 for **a–e**; (c) changes in L_3 as a function of temperature for **a** and **b**. (d) Individual contributions of inorganic and organic components to L_3 for **a** and **c** between 95 and 295 K.

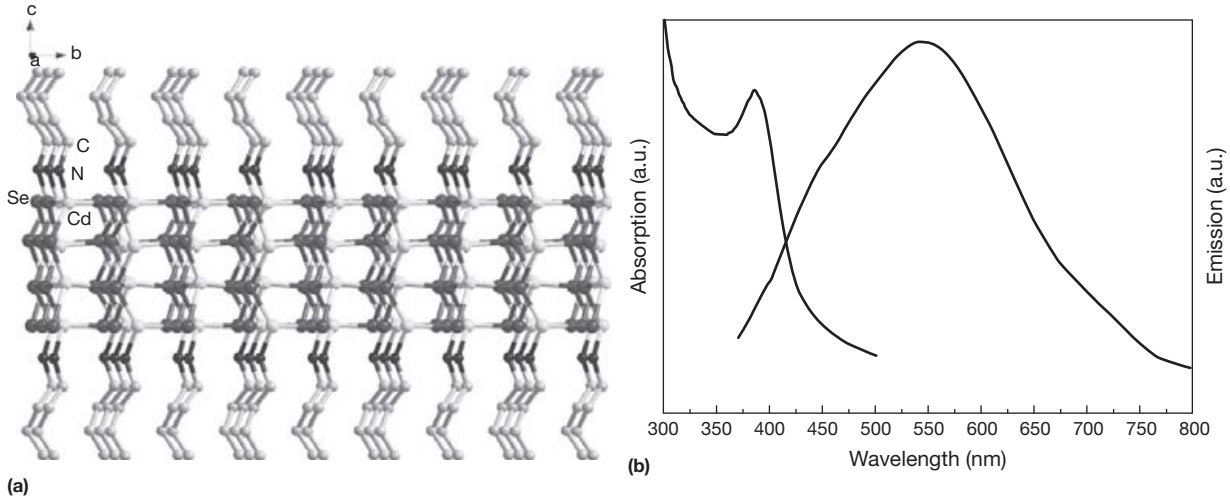

Figure 35 (a) Structure view of 2D-[Cd_2S_2(ba)]. (b) Absorption (λ_{ex} = 360 nm) and emission spectra of 2D-[Cd_2S_2(ba)] at room temperature.

process. The suspendable 0D-[$In_8Te_{12}(trien)_4$] can be used as a molecular-based precursor of In_2Te_3, and employed to deposit high-quality PV thin films containing the targeted material with appropriate stoichiometry. Along with other advantages such as one-pot synthesis, higher materials utilization efficiency, fewer processing steps, and ease in structure characterization, this hybrid QDs-based deposition method may enable a promising alternative approach to produce low-cost and high-efficiency PV and other optoelectronic devices.

2.14.4 Other Types of Metal Group-VI-Based Hybrid Semiconductor Nanostructures

Another strategy to prepare hybrid semiconductors is by making use of molecule-based extended solids that are analogous to known inorganic semiconductors. For example, the compound [$Pb(SC_6H_4S)]_n$ may be considered another type of PbS-based hybrid material where the semiconductor properties of the bulk PbS are largely retained in the hybrid phase. Based on

this strategy, sulfur-based ligands are explored as components of inorganic modules to construct hybrid materials.[332–337] However, most materials made through this way are actually molecular species or coordination polymers, possessing low conductivity or being insulating.

In 2008, Vaid et al.[338] reported a semiconducting PbS-based hybrid compound 3D-[$Pb_3(C_6S_6)$], which was prepared by reaction of $Pb(OAc)_2$ with benzenehexathiol in en solvent. This compound crystallized in a hexagonal space group *P6/mmm*, with each Pb coordinated by eight S atoms and each S bonding to four Pb atoms and one C atom.[338] The overall structure of this hybrid compound can be best described as a 3D Pb_3S_6 network periodically embedded with sulfur-terminated neutral hexagonal rings. Recently, Aron Walsh[339] investigated the electronic structure of 3D-[$Pb_3(C_6S_6)$] through DFT calculations. Based on the calculation results, it is confirmed that such a PbS-based hybrid maintains many of the key characteristics of PbS, and its electronic bandgap is also increased comparable to quantum-confined PbS nanoparticles. The optical bandgap of this hybrid material is 1.7 eV, ideal for harvesting the visible spectrum for photocatalytic and PV applications.

As a derivative of the II–VI hybrid system, Yao et al.[316] prepared the nanofiber bundle of a new type of hybrid semiconductors [$Cd(TeO_3)(L)$] (L = en, dien). The formula for this type of hybrid materials was proposed based on the evidences obtained from the PXRD, SEM, TEM, XPS, and FTIR analyses. In addition, element analysis (EA), TGA, and energy dispersive spectra (EDS) also verified that the experimental compositions of [$Cd(TeO_3)(L)$] are in good agreement with the calculated values based on the proposed formula. Inorganic $\{Cd(TeO_3)\}_n$ layers are assumed to exist in the structures and these layers are inter-connected by the diamine molecules through the coordination bonds between nitrogen atoms and cadmium ions. In $\{Cd(TeO_3)\}_n$ layers, the Cd atom is coordinated by four O and two N atoms while Te coordinates to three O atoms to form $[TeO_3]^{2-}$. Therefore, the overall structure of [$Cd(TeO_3)(L)$] is very similar to the 3D II–VI hybrid structure 3D-[$MQ(L)_{0.5}$], with its MQ layer replaced by $CdTeO_3$ and accordingly reducing the number of L by half. The thermal stabilities and optical properties of these nanofibre bundles have also been investigated. Thermal decomposition of [$Cd(TeO_3)(en)$] at 450 °C afforded a mixture of CdTe and $CdTeO_3$ phases, while for [$Cd(TeO_3)(dien)$] a pure CdTe phase was obtained. Furthermore, both of these two hybrids emit blue light and the emission intensity is strongly dependent on the acidity of the solutions. Such properties make them potentially useful as acid sensors.

Sofos et al.[167] recently reported a lamellar hybrid material containing periodic and alternating polycrystalline ZnO sheets (~1 nm thick) separated by conjugated organic molecules (~2–3-nm layers). This material is attained through a one-step self-assembly process by electrodeposition directly onto an electrode. Notably, the organic conjugated molecules not only serve as structural linkers, but also introduce opto-electronic functionality to the hybrid architecture. The π–π interactions among the conjugated molecules synergistically

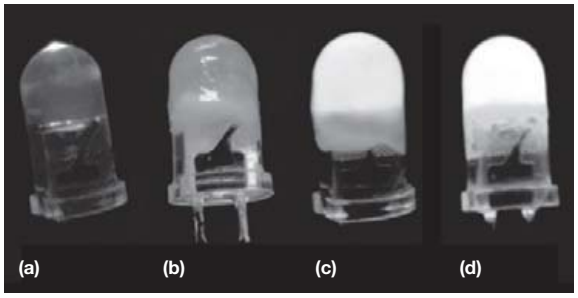

Figure 36 (a) A reference UV LED (360 nm)-emitting blue light (commercially available). (b) Image of the same LED coated with 2D-[Cd_2S_2(ba)] before illuminating. (c) Coated LED illuminating white light. (d) Coated LED illuminating white light after Mn^{2+} doping (0.1 mol%).

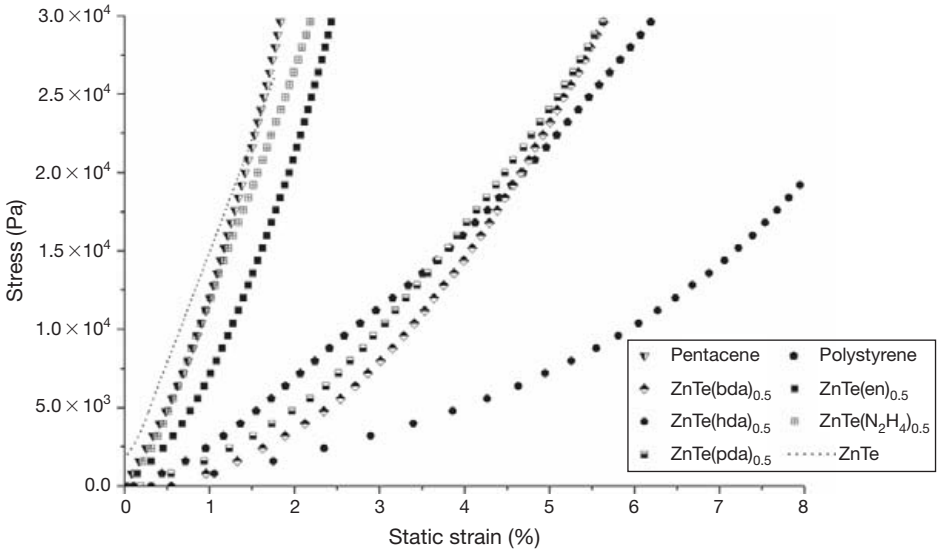

Figure 37 Stress–strain profiles of 3D-α-[$ZnTe(L)_{0.5}$] (L = N_2H_4, en, pda, bda, and hda) comparing with three reference materials ZnTe, pentacene, and polystyrene.

stabilize the hybrid nanostructure by converting the initially electrodeposited $Zn(OH)_2$ (insulator) into ZnO (semiconductor) at 150 °C. It is interesting to note that some optoelectronic properties of this hybrid nanostructure, such as photocurrent gains, normalized detectivities, and dynamic ranges, are among the best values measured for amorphous silicon, hybrid heterojunction, and photoconductive organic molecules reported to date. Therefore, this method offers a promising approach for the synthesis and device integration of high-efficient, flexible, wavelength-tunable, and environmentally benign photoconductors.

Another hybrid system is inorganic–organic copper chalcogenoantimonates. These materials can be synthesized by solvothermal reactions, and a total of four compounds (i.e., 2D-$[Cu_2SbSe_3(en)_{0.5}]$,[340] 2D-$[Cu_2SbSe_3(en)]$,[340] 2D-$[Cu_2SbSe_3(pda)_{0.5}]$,[341] and 2D-$[Cu_2SbS_3(en)_{0.5}]$[342]) have been reported to date. These hybrid structures consist of 2D $\{Cu_2SbQ_3\}_n$ (Q = S, Se) slabs separated (and hydrogen bonded) by neutral organic molecules residing between the slabs. All four compounds contain mixed-valent copper atoms Cu(I) and Cu(II), which has been confirmed by the magnetic susceptibility data.[342] The $\{Cu_2SbQ_3\}_n$ layers in 2D-$[Cu_2SbSe_3(en)_{0.5}]$ and 2D-$[Cu_2SbSe_3(en)]$ are very similar, while the orientations of the en molecules are different in the two structures. As both compounds have a bandgap of 1.6 eV and are earth-abundant, they are potentially suitable for use as absorber materials for PV applications.

Based on a similar strategy of incorporating transition metals into thioantimonate(III) networks, Bensch et al.[343–350] and other groups[351,352] synthesized a series of layered hybrid structures containing charge-neutral $Mn_2Sb_2S_5$ motifs. This hybrid family can be formulated as $[Mn_2Sb_2S_5(L)]$ (L = N_2H_4, en, pda, ptda, ma, ea, dien, and phen, respectively). Most compounds of this family possess a layered 2D structure analogous to their inorganic neutral layers $\{Mn_2Sb_2S_5\}_n$ stacked in a manner that the amine molecules fill the interlayer space and also partially the holes. An exception among these is $[Mn_2Sb_2S_5(N_2H_4)_3]$,[352] in which the neighboring $\{Mn_2Sb_2S_5\}_n$ layers are bridged by hydrazine molecules to afford a 3D structure. The magnetic properties of this series of hybrids are characteristic of frustrated magnetic systems, that is, although very large negative values of the Weiss constant are observed, no long-range order is found above 4 K.[345]

More recently, Bensch et al.[353] reported another type of Mn-thioantimonate-based hybrid structure, $Mn_3Sb_2S_6(L)$. In this structure, the neutral inorganic motifs $\{Mn_3Sb_2S_6\}_n$ are 1D chains, which are inter-connected by the diamine molecules in a bidentate manner, thus affording a 2D layered structure for $Mn_3Sb_2S_6(L)$. In addition, the magnetic properties of this compound are essentially determined by the 1D feature of $\{Mn_3Sb_2S_6\}_n$ chains, which has been confirmed by both the magnetic and the heat-capacity studies.

Several other hybrid ternary phases, for instance $[Mn_2SnS_4(N_2H_4)_2]$ and $[Mn_2SnS_4(N_2H_4)_5]$, were synthesized by Kanatzidis et al.[354] and Yuan et al.[355] As the inorganic phase Mn_2SnS_4 is known,[356] the hybrid compounds $[Mn_2SnS_4(N_2H_4)_x]$ can be regarded as insertion of N_2H_4 molecules into the neutral framework of Mn_2SnS_4. In doing so, the dense 3D network of Mn_2SnS_4 is expanded to offer a lower-density architecture. Although $[Mn_2SnS_4(N_2H_4)_2]$ and $[Mn_2SnS_4(N_2H_4)_5]$ possess the similar 3D frameworks, their local structural features are different.[354] Furthermore,

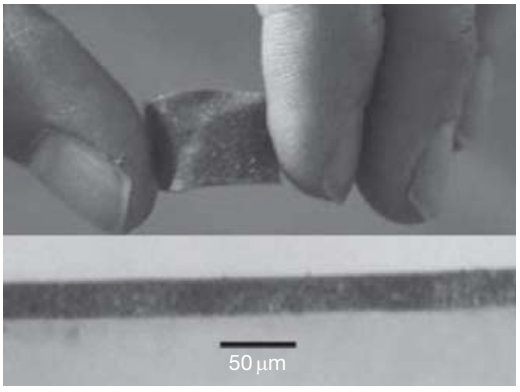

Figure 38 Top: A freestanding film sample made from 3D-α [ZnTe(hda)$_{0.5}$]; bottom: Cross-sectional view of the film showing the thickness (~25 μm).

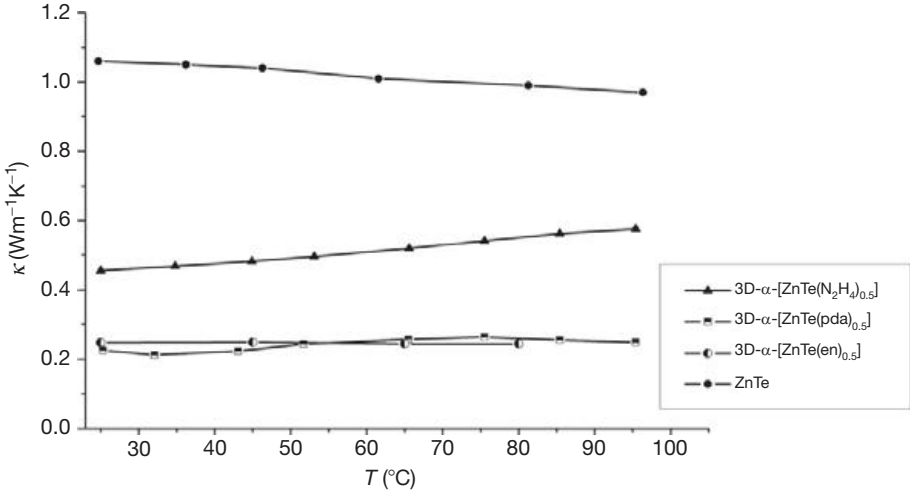

Figure 39 Thermal conductivity plots of ZnTe and selected hybrid compounds.

the 3D network of $[Mn_2SnS_4(N_2H_4)_5]$ is less dense than $[Mn_2SnS_4(N_2H_4)_2]$, and that is because the former incorporates more N_2H_4 molecules into its crystal lattice. For $[Mn_2SnS_4(N_2H_4)_2]$, it has been found that the strong antiferromagnetic interactions exist between the Mn^{2+} centers which exhibit ordering at ~41 K.[354]

As representative examples for VI–VI hybrid semiconductors, a number of MoO_3- and WO_3-based hybrid structures, such as 3D-$[MoO_3(L)_{0.5}]$ (L=4,4′-bpy, pyz),[357,358] 3D-$[WO_3(L)_{0.5}]$ (L=4,4′-bpy, pyz),[359] 2D-$[MoO_3(trz)_{0.5}]$,[357] and 1D-$[MoO_3(2,2'\text{-bpy})]$,[360] have been produced by hydrothermal reactions. These hybrid structures are constructed through the neutral metal oxide motifs (2D layers or 1D chains) linked or separated by organic molecules. Further, these metal oxide motifs can be considered as a slice (or thread) cut from the parent bulk materials (i.e., MoO_3 or WO_3) with the structure little perturbed. The analogy is apparent with regard to the II–VI hybrid systems. For 3D-$[MoO_3(4,4'\text{-bpy})_{0.5}]$, the MoO_3 layers are stacked in an 'ABAB…' sequence; hence, its structure can be described as composed of alternating arrays of inorganic metal oxide layers and organic tethers. Particularly, Zubieta et al.[357] found that partial reduction of $[MoO_3(4,4'\text{-bpy})_{0.5}]$ could produce a mixed-valence material $[H_xMoO_3(4,4'\text{-bpy})_{0.5}]$ ($x \approx 0.5$). This phase preserves the main structural features of the parent $[MoO_3(4,4'\text{-bpy})_{0.5}]$, and calculation has predicted it to be metallic, as found for H_x-MoO_3.[357]

The VI–VI hybrid material $[WO_x(en)]$ has been prepared as nanobelts by Hu et al.[361] via a mild solvothermal process. The nanobelts are ~50 nm wide with lengths up to several tens of micrometers. They exhibit promising responses for photoswitches and may have potential for applications in optoelectronics.

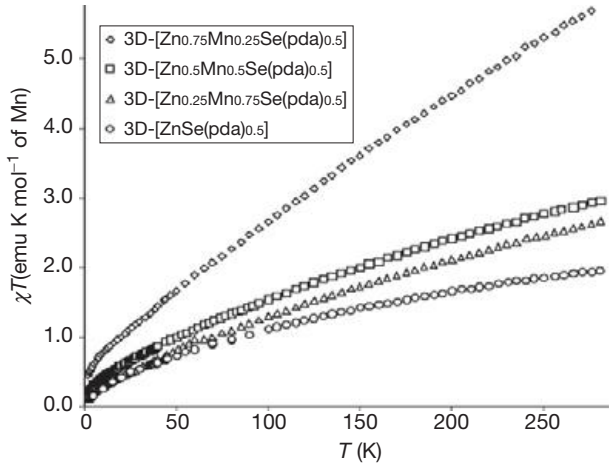

Figure 40 χT versus T plots for Mn-doped 3D-$[ZnSe(pda)_{0.5}]$ compounds.

2.14.5 Conclusion

In conclusion, this chapter presents an overview on the recent development of nanostructured inorganic–organic hybrid materials built on metal chalcogenide (M_xQ_y, M=metal, Q=group-VI chalcogen) semiconductors. By incorporating inorganic and organic components (modules) into a single crystal lattice, an unprecedented class of semiconductor nanostructures comprised of periodically ordered arrays of zero-, one-, two-, and three-dimensions is constructed. The inorganic component in these hybrid structures can be regarded as a sub-nanometer-sized M_xQ_y segment (i.e., cluster, chain, or layer) cut from its parent semiconductor. Therefore, its composition, coordination, structure, and charge remain intact or practically unchanged. The organic component, on the other hand, serves both as a passivating agent to confine the inorganic nanostructures and as a structure-directing agent to guide the inorganic segments into a perfectly ordered arrangement. As a result, the semiconductor properties of the parent materials are well retained in their hybrid phases. In addition, such a unique and modular combination of two distinctively different components into a single crystal structure not only leads to significantly enhanced and integrated properties, but also introduces new phenomena and appealing features that are impossible with either individual component alone, for example, nearly zero thermal expansion and direct white-light emission observed in the single- and double-layered structures, respectively.

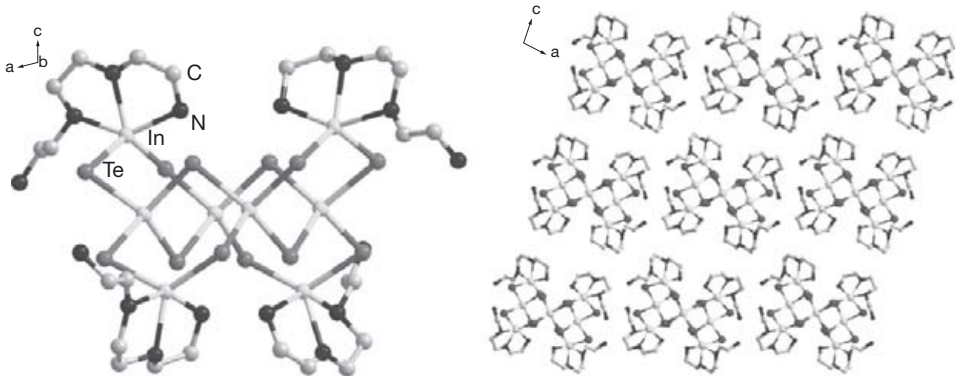

Figure 41 Views of the 0D-$[In_8Te_{12}(trien)_4]$ structure: (a) $\{In_8Te_{12}(trien)_4\}$ cluster and (b) the overall packing structure viewing down the *b*-axis. Hydrogen atoms are omitted for clarity.

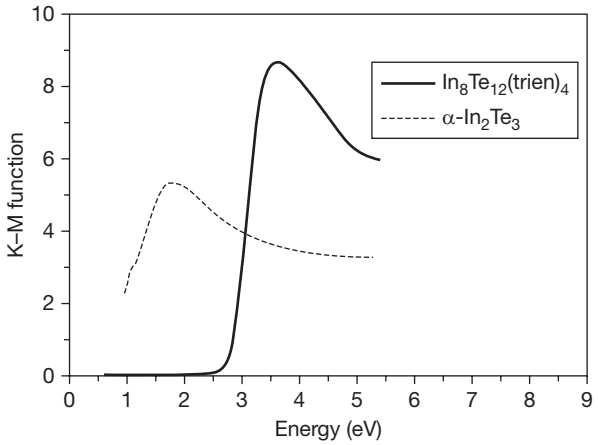

Figure 42 Optical absorption spectra of 0D-[$In_8Te_{12}(trien)_4$] (solid line) and α-In_2Te_3 (dashed line).

Most of these hybrid materials exhibit large blue shifts in their optical absorption edge, due to a very strong structure-induced QCE. Such a confinement originates from their inherent crystal structures, rather than the reduction of their physical dimensions, and is therefore conceptually different from the size-induced QCE found in conventional QDs. This allows a complete elimination of the particle-size requirement and the extent of such confinement can be tuned systematically by controlling structural topology, dimensionality, as well as material composition. Because the blending of inorganic and organic nano-modules in these hybrid structures takes place at the atomic/molecular level and through strong chemical bonds, materials of this type may be free of certain interface issues that are inevitable for other nanoparticles and composite materials. Compared to the conventional ways for the preparation of hybrid nanocomposite materials, the synthesis of the crystalline M_xQ_y hybrid nanostructures offers a feasible and effective approach to avoid structural fluctuations and phase inhomogeneity.

The discovery of the M_xQ_y-based hybrid inorganic–organic semiconductors opens a new direction in the development of functional materials and contributes to better understanding of structure–property relationships in complex materials. Continued advancement in nanostructured hybrid material research will be very important for both fundamental science and technological applications.

Acknowledgments

Financial support from National Science Foundation (NSF) (Grants DMR-0094872, DMR-0422932, DMR-0769069) is gratefully acknowledged. We thank Dr. Xiaoying Huang, Dr. Wooseok Ki, Mojgan Roushan, Dr. Wenhua Bi, Dr. Xiaoming Fang, Xiao Zhang, Harry R. Heulings IV, Vina Le, Srihari Reddy, and Jessica Strong for their direct contributions to this chapter. We are grateful to our collaborators, Prof. Yong Zhang, Prof. Huaxiong Fu, Prof. Tan Yuen, Prof. Ronggui Yang, Prof. Shuhong Yu, Dr. Brian Fluegel, and Dr. Chang-Youn Moon, for their contributions and helpful discussions. We also thank Dr. Thomas J. Emge for his assistance with crystal-structure analysis.

References

1. Alivisatos, A. P. *J. Phys. Chem.* **1996**, *100*, 13226–13239.
2. Setter, N.; Waser, R. *Acta Mater.* **2000**, *48*, 151–178.
3. Eychmuller, A. *J. Phys. Chem. B* **2000**, *104*, 6514–6528.
4. Efros, A. L.; Rosen, M. *Annu. Rev. Mater. Sci.* **2000**, *30*, 475–521.
5. Murray, C. B.; Kagan, C. R.; Bawendi, M. G. *Annu. Rev. Mater. Sci.* **2000**, *30*, 545–610.
6. Bent, S. F. *Surf. Sci.* **2002**, *500*, 879–903.
7. Cozzoli, P. D.; Pellegrino, T.; Manna, L. *Chem. Soc. Rev.* **2006**, *35*, 1195–1208.
8. Ozgur, U.; Alivov, Y. I.; Liu, C.; Teke, A.; Reshchikov, M. A.; Dogan, S.; Avrutin, V.; Cho, S. J.; Morkoc, H. *J. Appl. Phys.* **2005**, *98*, 041301.
9. Huber, A. J.; Kazantsev, D.; Keilmann, F.; Wittborn, J.; Hillenbrand, R. *Adv. Mater.* **2007**, *19*, 2209–2212.
10. Bardeen, J.; Brattain, W. H. *Phys. Rev.* **1948**, *74*, 230–231.
11. Shockley, W.; Bardeen, J.; Brattain, W. H. *Science* **1948**, *108*, 678–679.
12. Kilby, J. S. *IEEE Trans. Electron Devices* **1976**, *23*, 648–654.
13. Hoffmann, M. R.; Martin, S. T.; Choi, W. Y.; Bahnemann, D. W. *Chem. Rev.* **1995**, *95*, 69–96.
14. Joachim, C.; Gimzewski, J. K.; Aviram, A. *Nature* **2000**, *408*, 541–548.
15. Casady, J. B.; Johnson, R. W. *Solid State Electron.* **1996**, *39*, 1409–1422.
16. Castro Neto, A. H.; Guinea, F.; Peres, N. M. R.; Novoselov, K. S.; Geim, A. K. *Rev. Mod. Phys.* **2009**, *81*, 109–162.
17. Ponce, F. A.; Bour, D. P. *Nature* **1997**, *386*, 351–359.
18. Briseno, A. L.; Yang, P. D. *Nat. Mater.* **2009**, *8*, 7–8.
19. Schoning, M. J.; Ronkel, F.; Crott, M.; Thust, M.; Schultze, J. W.; Kordos, P.; Luth, H. *Electrochim. Acta* **1997**, *42*, 3185–3193.
20. Ito, T.; Okazaki, S. *Nature* **2000**, *406*, 1027–1031.
21. Huang, Y.; Duan, X. F.; Cui, Y.; Lauhon, L. J.; Kim, K. H.; Lieber, C. M. *Science* **2001**, *294*, 1313–1317.
22. Keyes, R. W. *Rep. Prog. Phys.* **2005**, *68*, 2701–2746.
23. Finkelstein, H.; Hsu, M. J.; Zlatanovic, S.; Esener, S. *Rev. Sci. Instrum.* **2007**, *78*, 103103.
24. Yang, S. M.; Lee, T.; Cong, M. *Sens. Actuator A: Phys.* **2010**, *157*, 258–266.
25. Kurd, N. A.; Bhamidipati, S.; Mozak, C.; Miller, J. L.; Mosalikanti, P.; Wilson, T. M.; El-Husseini, A. M.; Neidengard, M.; Aly, R. E.; Nemani, M.; Chowdhury, M.; Kumar, R. *IEEE J. Solid-State Circuit* **2011**, *46*, 119–130.
26. Awschalom, D. D.; Flatte, M. E. *Nat. Phys.* **2007**, *3*, 153–159.
27. Klostranec, J. M.; Chan, W. C. W. *Adv. Mater.* **2006**, *18*, 1953–1964.
28. Phillips, J. M.; Coltrin, M. E.; Crawford, M. H.; Fischer, A. J.; Krames, M. R.; Mueller-Mach, R.; Mueller, G. O.; Ohno, Y.; Rohwer, L. E. S.; Simmons, J. A.; Tsao, J. Y. *Laser Photon. Rev.* **2007**, *1*, 307–333.
29. Pichler, P.; Burenkov, A.; Lorenz, J.; Kampen, C.; Frey, L. *Thin Solid Films* **2010**, *518*, 2478–2484.
30. Berger, L. I. *Semiconductor Materials*. CRC Press: New York, 1997.
31. Huang, M. H.; Mao, S.; Feick, H.; Yan, H. Q.; Wu, Y. Y.; Kind, H.; Weber, E.; Russo, R.; Yang, P. D. *Science* **2001**, *292*, 1897–1899.
32. Hoffman, R. L.; Norris, B. J.; Wager, J. F. *Appl. Phys. Lett.* **2003**, *82*, 733–735.
33. Tian, Z. R. R.; Voigt, J. A.; Liu, J.; McKenzie, B.; McDermott, M. J.; Rodriguez, M. A.; Konishi, H.; Xu, H. F. *Nat. Mater.* **2003**, *2*, 821–826.
34. Yang, P. D.; Yan, H. Q.; Mao, S.; Russo, R.; Johnson, J.; Saykally, R.; Morris, N.; Pham, J.; He, R. R.; Choi, H. J. *Adv. Funct. Mater.* **2002**, *12*, 323–331.
35. Djurisic, A. B.; Leung, Y. H. *Small* **2006**, *2*, 944–961.
36. Klingshirn, C. *ChemPhysChem* **2007**, *8*, 782–803.
37. Ma, C.; Moore, D.; Li, J.; Wang, Z. L. *Adv. Mater.* **2003**, *15*, 228–231.
38. Wang, Z. W.; Daemen, L. L.; Zhao, Y. S.; Zha, C. S.; Downs, R. T.; Wang, X. D.; Wang, Z. L.; Hemley, R. J. *Nat. Mater.* **2005**, *4*, 922–927.
39. Steckel, J. S.; Zimmer, J. P.; Coe-Sullivan, S.; Stott, N. E.; Bulovic, V.; Bawendi, M. G. *Angew. Chem. Int. Ed.* **2004**, *43*, 2154–2158.
40. Ramanathan, K.; Contreras, M. A.; Perkins, C. L.; Asher, S.; Hasoon, F. S.; Keane, J.; Young, D.; Romero, M.; Metzger, W.; Noufi, R.; Ward, J.; Duda, A. *Prog. Photovoltaics* **2003**, *11*, 225–230.
41. Sun, W. T.; Yu, Y.; Pan, H. Y.; Gao, X. F.; Chen, Q.; Peng, L. M. *J. Am. Chem. Soc.* **2008**, *130*, 1124–1125.
42. Fang, X. S.; Bando, Y.; Gautam, U. K.; Zhai, T. Y.; Zeng, H. B.; Xu, X. J.; Liao, M. Y.; Golberg, D. *Crit. Rev. Solid State Mater. Sci.* **2009**, *34*, 190–223.
43. Li, Y. B.; Bando, Y.; Golberg, D. *Appl. Phys. Lett.* **2004**, *84*, 3603–3605.
44. Wang, R. C.; Liu, C. P.; Huang, J. L.; Chen, S. J.; Tseng, Y. K.; Kung, S. C. *Appl. Phys. Lett.* **2005**, *87*, 013110.
45. Zhu, Y. W.; Zhang, H. Z.; Sun, X. C.; Feng, S. Q.; Xu, J.; Zhao, Q.; Xiang, B.; Wang, R. M.; Yu, D. P. *Appl. Phys. Lett.* **2003**, *83*, 144–146.
46. Bosio, A.; Romeo, N.; Mazzamuto, S.; Canevari, V. *Prog. Cryst. Growth Charact. Mater.* **2006**, *52*, 247–279.

47. Nozik, A. J.; Beard, M. C.; Luther, J. M.; Law, M.; Ellingson, R. J.; Johnson, J. C. *Chem. Rev.* **2010**, *110*, 6873–6890.
48. Zhai, T. Y.; Fang, X. S.; Li, L.; Golberg, D. *Nanoscale* **2010**, *2*, 168–187.
49. Birkmire, R. W.; McCandless, B. E. *Curr. Opin. Solid State Mater. Sci.* **2010**, *14*, 139–142.
50. Chopra, K. L.; Paulson, P. D.; Dutta, V. *Prog. Photovoltaics* **2004**, *12*, 69–92.
51. Janowitz, C.; Orlowski, N.; Manzke, R.; Golacki, Z. *J. Alloys Compd.* **2001**, *328*, 84–89.
52. Rogach, A.; Kershaw, S.; Burt, M.; Harrison, M.; Kornowski, A.; Eychmuller, A.; Weller, H. *Adv. Mater.* **1999**, *11*, 552–555.
53. Rogach, A. L.; Eychmuller, A.; Hickey, S. G.; Kershaw, S. V. *Small* **2007**, *3*, 536–557.
54. Madelung, O. *Semiconductors: Data Handbook*, 3rd ed.; Springer: Berlin, 2004.
55. Julien, C. M.; Balkanski, M. *Mater. Sci. Eng. B: Solid State Mater. Adv. Technol.* **2003**, *100*, 263–270.
56. Peng, H. L.; Zhang, X. F.; Twesten, R. D.; Cui, Y. *Nano Res.* **2009**, *2*, 327–335.
57. Gordillo, G.; Calderon, C. *Sol. Energy Mater. Sol. Cells* **2003**, *77*, 163–173.
58. Afzaal, M.; O'Brien, P. *J. Mater. Chem.* **2006**, *16*, 1597–1602.
59. Lee, H.; Kim, Y. K.; Kim, D.; Kang, D. H. *IEEE Trans. Magn.* **2005**, *41*, 1034–1036.
60. Gibson, G. A.; Chaiken, A.; Nauka, K.; Yang, C. C.; Davidson, R.; Holden, A.; Bicknell, R.; Yeh, B. S.; Chen, J.; Liao, H.; Subramanian, S.; Schut, D.; Jasinski, J.; Liliental-Weber, Z. *Appl. Phys. Lett.* **2005**, *86*, 051902.
61. Sun, X. H.; Yu, B.; Ng, G.; Nguyen, T. D.; Meyyappan, M. *Appl. Phys. Lett.* **2006**, *89*, 233121.
62. Rhyee, J. S.; Cho, E.; Lee, K. H.; Lee, S. M.; Kim, S. I.; Kim, H. S.; Kwon, Y. S.; Kim, S. J. *Appl. Phys. Lett.* **2009**, *95*, 212106.
63. Hariskos, D.; Spiering, S.; Powalla, M. *Thin Solid Films* **2005**, *480*, 99–109.
64. Naghavi, N.; Spiering, S.; Powalla, M.; Cavana, B.; Lincot, D. *Prog. Photovoltaics* **2003**, *11*, 437–443.
65. Barreau, N.; Marsillac, S.; Bernede, J. C.; Barreau, A. *Appl. Surf. Sci.* **2000**, *161*, 20–26.
66. Barreau, N. *Sol. Energy* **2009**, *83*, 363–371.
67. Krimmel, A.; Seidov, Z.; Guseinov, G. G.; Najafov, A. I.; von Nidda, H. A. K.; Loidl, A.; Tobbens, D. M. *J. Phys.: Condens. Matter* **2005**, *17*, 3611–3618.
68. Bodnar, I. V.; Ilchuk, G. A.; Petrus, R. Y.; Rud, V. Y.; Rud, Y. V.; Serginov, M. *Semiconductors* **2009**, *43*, 1138–1141.
69. Yang, M. D.; Hu, C. H.; Shen, J. L.; Lan, S. M.; Huang, P. J.; Chi, G. C.; Chen, K. H.; Chen, L. C.; Lin, T. Y. *Nanoscale Res. Lett.* **2008**, *3*, 427–430.
70. Peng, H. L.; Schoen, D. T.; Meister, S.; Zhang, X. F.; Cui, Y. *J. Am. Chem. Soc.* **2007**, *129*, 34–35.
71. Desai, R. R.; Lakshminarayana, D.; Patel, P. B.; Panchal, C. J. *J. Mater. Sci.* **2006**, *41*, 2019–2023.
72. Lakshminarayana, D.; Patel, P. B.; Desai, R. R.; Panchal, C. J. *J. Mater. Sci.: Mater. Electron.* **2002**, *13*, 27–30.
73. Pei, Y. Z.; Morelli, D. T. *Appl. Phys. Lett.* **2009**, *94*, 122112.
74. Desai, R. R.; Lakshminarayana, D.; Patel, P. B.; Panchal, C. J. *Sens. Actuator B: Chem.* **2005**, *107*, 523–527.
75. Desai, R. R.; Lakshminarayana, D.; Patel, P. B.; Panchal, C. J. *Sens. Actuator A: Phys.* **2005**, *121*, 405–409.
76. Zhu, H.; Chen, K.; Ge, Z. Y.; Xu, H. N.; Su, Y.; Yin, J.; Xia, Y. D.; Liu, Z. G. *J. Mater. Sci.* **2010**, *45*, 3569–3574.
77. Kurum, U.; Yuksek, M.; Yaglioglu, H. G.; Elmali, A.; Ates, A.; Karabulut, M.; Mamedov, G. M. *J. Appl. Phys.* **2010**, *108*, 063102.
78. Yuksek, M.; Kurum, U.; Yaglioglu, H. G.; Elmali, A.; Ates, A. *J. Appl. Phys.* **2010**, *107*, 033115.
79. Feng, Z. S.; Kang, Z. H.; Wu, F. G.; Gao, J. Y.; Jiang, Y.; Zhang, H. Z.; Andreev, Y. M.; Lanskii, G. V.; Atuchin, V. V.; Gavrilova, T. A. *Opt. Express* **2008**, *16*, 9978–9985.
80. Jamshidi-Ghaleh, K.; Karimi, M. *Opt. Commun.* **2008**, *281*, 5561–5565.
81. Kovalenko, M. V.; Heiss, W.; Shevchenko, E. V.; Lee, J. S.; Schwinghammer, H.; Alivisatos, A. P.; Talapin, D. V. *J. Am. Chem. Soc.* **2007**, *129*, 11354–11355.
82. Littlewood, P. B.; Mihaila, B.; Schulze, R. K.; Safarik, D. J.; Gubernatis, J. E.; Bostwick, A.; Rotenberg, E.; Opeil, C. P.; Durakiewicz, T.; Smith, J. L.; Lashley, J. C. *Phys. Rev. Lett.* **2010**, *105*, 086404.
83. Shaltaf, R.; Durgun, E.; Raty, J. Y.; Ghosez, P.; Gonze, X. *Phys. Rev. B* **2008**, *78*, 205203.
84. Sivabharathy, M.; Sankar, N.; Saravanan, R.; Ramachandran, K. *Bull. Mater. Sci.* **2005**, *28*, 675–679.
85. Akola, J.; Jones, R. O. *Phys. Rev. B* **2007**, *76*, 235201.
86. Lee, S. H.; Ko, D. K.; Jung, Y.; Agarwal, R. *Appl. Phys. Lett.* **2006**, *89*, 223116.
87. Parenteau, M.; Carlone, C. *Phys. Rev. B* **1990**, *41*, 5227–5234.
88. Johnson, J. B.; Jones, H.; Latham, B. S.; Parker, J. D.; Engelken, R. D.; Barber, C. *Semicond. Sci. Technol.* **1999**, *14*, 501–507.
89. Reddy, N. K.; Hahn, Y. B.; Devika, M.; Sumana, H. R.; Gunasekhar, K. R. *J. Appl. Phys.* **2007**, *101*, 093522.
90. Hickey, S. G.; Waurisch, C.; Rellinghaus, B.; Eychmuller, A. *J. Am. Chem. Soc.* **2008**, *130*, 14978–14980.
91. Devika, M.; Reddy, N. K.; Ramesh, K.; Sumana, H. R.; Gunasekhar, K. R.; Gopal, E. S. R.; Reddy, K. T. R. *Semicond. Sci. Technol.* **2006**, *21*, 1495–1501.
92. Rogalski, A. *Prog. Quant. Electron.* **2003**, *27*, 59–210.
93. Zogg, H.; Alchalabi, K.; Zimin, D.; Kellermann, K. *IEEE Trans. Electron Devices* **2003**, *50*, 209–214.
94. Arnold, M.; Zimin, D.; Alchalabi, K.; Zogg, H. *J. Cryst. Growth* **2005**, *278*, 739–742.
95. Zhuravlev, K. K.; Pietryga, J. M.; Sander, R. K.; Schaller, R. D. *Appl. Phys. Lett.* **2007**, *90*, 043110.
96. Heremans, J. P.; Jovovic, V.; Toberer, E. S.; Saramat, A.; Kurosaki, K.; Charoenphakdee, A.; Yamanaka, S.; Snyder, G. J. *Science* **2008**, *321*, 554–557.
97. Heremans, J. P.; Thrush, C. M.; Morelli, D. T. *J. Appl. Phys.* **2005**, *98*, 063703.
98. Heremans, J. P.; Thrush, C. M.; Morelli, D. T. *Phys. Rev. B* **2004**, *70*, 115334.
99. Sootsman, J. R.; Chung, D. Y.; Kanatzidis, M. G. *Angew. Chem. Int. Ed.* **2009**, *48*, 8616–8639.
100. Venkatasubramanian, R.; Siivola, E.; Colpitts, T.; O'Quinn, B. *Nature* **2001**, *413*, 597–602.
101. Bottner, H.; Nurnus, J.; Gavrikov, A.; Kuhner, G.; Jagle, M.; Kunzel, C.; Eberhard, D.; Plescher, G.; Schubert, A.; Schlereth, K. H. *J. Microelectromech. Syst.* **2004**, *13*, 414–420.
102. Boulouz, A.; Chakraborty, S.; Giani, A.; Delannoy, F. P.; Boyer, A.; Schumann, J. *J. Appl. Phys.* **2001**, *89*, 5009–5014.
103. Martin-Gonzalez, M.; Prieto, A. L.; Gronsky, R.; Sands, T.; Stacy, A. M. *J. Electrochem. Soc.* **2002**, *149*, C546–C554.
104. Kanatzidis, M. G. *Chem. Mater.* **2010**, *22*, 648–659.
105. Xiao, F.; Hangarter, C.; Yoo, B.; Rheem, Y.; Lee, K. H.; Myung, N. V. *Electrochim. Acta* **2008**, *53*, 8103–8117.
106. Peranio, N.; Eibl, O. *J. Appl. Phys.* **2008**, *103*, 024314.
107. Poudel, B.; Hao, Q.; Ma, Y.; Lan, Y. C.; Minnich, A.; Yu, B.; Yan, X. A.; Wang, D. Z.; Muto, A.; Vashaee, D.; Chen, X. Y.; Liu, J. M.; Dresselhaus, M. S.; Chen, G.; Ren, Z. F. *Science* **2008**, *320*, 634–638.
108. Bernevig, B. A.; Hughes, T. L.; Zhang, S. C. *Science* **2006**, *314*, 1757–1761.
109. Zhang, S. C.; Qi, X. L. *Phys. Today* **2010**, *63*, 12.
110. Hasan, M. Z.; Kane, C. L. *Rev. Mod. Phys.* **2010**, *82*, 3045–3067.
111. Zhang, H. J.; Liu, C. X.; Qi, X. L.; Dai, X.; Fang, Z.; Zhang, S. C. *Nat. Phys.* **2009**, *5*, 438–442.
112. Delley, B.; Steigmeier, E. F. *Phys. Rev. B* **1993**, *47*, 1397–1400.
113. Ogut, S.; Chelikowsky, J. R.; Louie, S. G. *Phys. Rev. Lett.* **1997**, *79*, 1770–1773.
114. Yu, H.; Li, J. B.; Loomis, R. A.; Wang, L. W.; Buhro, W. E. *Nat. Mater.* **2003**, *2*, 517–520.
115. Bryant, G. W. *Phys. Rev. B* **1988**, *37*, 8763–8772.
116. Merz, J. L.; Lee, S.; Furdyna, J. K. *J. Cryst. Growth* **1998**, *184*, 228–236.
117. Xie, H. Y.; Liang, J. G.; Liu, Y.; Zhang, Z. L.; Pang, D. W.; He, Z. K.; Lu, Z. X.; Huang, W. H. *J. Nanosci. Nanotechnol.* **2005**, *5*, 880–886.
118. Hu, J. T.; Li, L. S.; Yang, W. D.; Manna, L.; Wang, L. W.; Alivisatos, A. P. *Science* **2001**, *292*, 2060–2063.
119. Qu, L. H.; Peng, X. G. *J. Am. Chem. Soc.* **2002**, *124*, 2049–2055.
120. Bailey, R. E.; Strausburg, J. B.; Nie, S. M. *J. Nanosci. Nanotechnol.* **2004**, *4*, 569–574.
121. Sundar, V. C.; Eisler, H. J.; Bawendi, M. G. *Adv. Mater.* **2002**, *14*, 739–743.
122. Li, J. J.; Wang, Y. A.; Guo, W. Z.; Keay, J. C.; Mishima, T. D.; Johnson, M. B.; Peng, X. G. *J. Am. Chem. Soc.* **2003**, *125*, 12567–12575.
123. Peng, X. G.; Manna, L.; Yang, W. D.; Wickham, J.; Scher, E.; Kadavanich, A.; Alivisatos, A. P. *Nature* **2000**, *404*, 59–61.
124. Chen, J.; Song, J. L.; Sun, X. W.; Deng, W. Q.; Jiang, C. Y.; Lei, W.; Huang, J. H.; Liu, R. S. *Appl. Phys. Lett.* **2009**, *94*, 153115.
125. Koppens, F. H. L.; Buizert, C.; Tielrooij, K. J.; Vink, I. T.; Nowack, K. C.; Meunier, T.; Kouwenhoven, L. P.; Vandersypen, L. M. K. *Nature* **2006**, *442*, 766–771.
126. Loss, D.; DiVincenzo, D. P. *Phys. Rev. A* **1998**, *57*, 120–126.
127. Petta, J. R.; Johnson, A. C.; Taylor, J. M.; Laird, E. A.; Yacoby, A.; Lukin, M. D.; Marcus, C. M.; Hanson, M. P.; Gossard, A. C. *Science* **2005**, *309*, 2180–2184.
128. Barrett, S. D.; Kok, P. *Phys. Rev. A* **2005**, *71*, 060310.
129. Golovach, V. N.; Borhani, M.; Loss, D. *Phys. Rev. A* **2010**, *81*, 022315.
130. Wang, Q.; Pan, D. C.; Jiang, S. C.; Ji, X. L.; An, L. J.; Jiang, B. Z. *Chem. Eur. J.* **2005**, *11*, 3843–3848.

131. Tan, Z. N.; Zhang, F.; Zhu, T.; Xu, J.; Wang, A. Y.; Dixon, D.; Li, L. S.; Zhang, Q.; Mohney, S. E.; Ruzyllo, J. *Nano Lett.* **2007**, *7*, 3803–3807.
132. Stouwdam, J. W.; Janssen, R. A. J. *Adv. Mater.* **2009**, *21*, 2916–2920.
133. Shen, C. C.; Tseng, W. L. *Inorg. Chem.* **2009**, *48*, 8689–8694.
134. Cheng, G.; Mazzeo, M.; Rizzo, A.; Li, Y. Q.; Duan, Y.; Gigli, G. *Appl. Phys. Lett.* **2009**, *94*, 243506.
135. Loffler, W.; Hopcke, N.; Kalt, H.; Li, S. F.; Grun, M.; Hetterich, M. *Appl. Phys. Lett.* **2010**, *96*, 052113.
136. Lohmeyer, H.; Sebald, K.; Kruse, C.; Kroger, R.; Gutowski, J.; Hommel, D.; Wiersig, J.; Baer, N.; Jahnke, F. *Appl. Phys. Lett.* **2006**, *88*, 051101.
137. Kazes, M.; Lewis, D. Y.; Ebenstein, Y.; Mokari, T.; Banin, U. *Adv. Mater.* **2002**, *14*, 317–321.
138. Snee, P. T.; Chan, Y. H.; Nocera, D. G.; Bawendi, M. G. *Adv. Mater.* **2005**, *17*, 1131–1136.
139. Schafer, J.; Mondia, J. P.; Sharma, R.; Lu, Z. H.; Susha, A. S.; Rogach, A. L.; Wang, L. J. *Nano Lett.* **2008**, *8*, 1709–1712.
140. Bailey, R. E.; Nie, S. M. *J. Am. Chem. Soc.* **2003**, *125*, 7100–7106.
141. Yoffe, A. D. *Adv. Phys.* **2001**, *50*, 1–208.
142. Gerdova, I.; Hache, A. *Opt. Commun.* **2005**, *246*, 205–212.
143. Sen, S.; Chakrabarti, S. *Phys. Rev. B* **2006**, *74*, 205435.
144. Zielinski, M.; Oron, D.; Chauvat, D.; Zyss, J. *Small* **2009**, *5*, 2835–2840.
145. Karthikeyan, B.; Sandeep, C. S. S.; Pandiyarajan, T.; Venkatesan, P.; Philip, R. *Appl. Phys. Lett.* **2009**, *95*, 023118.
146. Chattopadhyay, M.; Kumbhakar, P.; Tiwary, C. S.; Mitra, A. K.; Chatterjee, U.; Kobayashi, T. *Opt. Lett.* **2009**, *34*, 3644–3646.
147. Weng, J. F.; Ren, J. C. *Curr. Med. Chem.* **2006**, *13*, 897–909.
148. Liu, P.; Wang, Q. S.; Li, X. *J. Phys. Chem. C* **2009**, *113*, 7670–7676.
149. Kumar, R.; Ding, H.; Hu, R.; Yong, K. T.; Roy, I.; Bergey, E. J.; Prasad, P. N. *Chem. Mater.* **2010**, *22*, 2261–2267.
150. Prabakar, S.; Shiohara, A.; Hanada, S.; Fujioka, K.; Yamamoto, K.; Tilley, R. D. *Chem. Mater.* **2010**, *22*, 482–486.
151. Alivisatos, A. P. *Science* **1996**, *271*, 933–937.
152. Yu, W. W.; Chang, E.; Drezek, R.; Colvin, V. L. *Biochem. Biophys. Res. Commun.* **2006**, *348*, 781–786.
153. Azzazy, H. M. E.; Mansour, M. M. H.; Kazinierczak, S. C. *Clin. Biochem.* **2007**, *40*, 917–927.
154. Bowers, M. J.; McBride, J. R.; Rosenthal, S. J. *J. Am. Chem. Soc.* **2005**, *127*, 15378–15379.
155. Schreuder, M. A.; Gosnell, J. D.; Smith, N. J.; Warnement, M. R.; Weiss, S. M.; Rosenthal, S. J. *J. Mater. Chem.* **2008**, *18*, 970–975.
156. Gaul, D. A.; Rees, W. S. *Adv. Mater.* **2000**, *12*, 935–946.
157. Miki, K.; Abe, T.; Naruse, J.; Ikumi, K.; Yamaguchi, T.; Kasada, H.; Ando, K. *Phys. Status Solidi B: Basic Solid State Phys.* **2006**, *243*, 950–954.
158. JoseYacaman, M.; Rendon, L.; Arenas, J.; Puche, M. C. S. *Science* **1996**, *273*, 223–225.
159. Mitzi, D. B. *Prog. Inorg. Chem.* **1999**, *48*, 1–121.
160. Chesnut, D. J.; Hagrman, D.; Zapf, P. J.; Hammond, R. P.; LaDuca, R.; Haushalter, R. C.; Zubieta, J. *Coord. Chem. Rev.* **1999**, *192*, 737–769.
161. Asefa, T.; MacLachlan, M. J.; Coombs, N.; Ozin, G. A. *Nature* **1999**, *402*, 867–871.
162. Voss, D. *Nature* **2000**, *407*, 442–444.
163. Coe, S.; Woo, W. K.; Bawendi, M.; Bulovic, V. *Nature* **2002**, *420*, 800–803.
164. Elhamzaoui, H.; Jousseaume, B.; Riague, H.; Toupance, T.; Dieudonne, P.; Zakri, C.; Maugey, M.; Allouchi, H. *J. Am. Chem. Soc.* **2004**, *126*, 8130–8131.
165. Jaroniec, M. *Nature* **2006**, *442*, 638–640.
166. Gur, I.; Fromer, N. A.; Chen, C. P.; Kanaras, A. G.; Alivisatos, A. P. *Nano Lett.* **2007**, *7*, 409–414.
167. Sofos, M.; Goldberger, J.; Stone, D. A.; Allen, J. E.; Ma, Q.; Herman, D. J.; Tsai, W. W.; Lauhon, L. J.; Stupp, S. I. *Nat. Mater.* **2009**, *8*, 68–75.
168. Li, J.; Huang, X. Y. *Nanostructured Crystals: An Unprecedented Class of Hybrid Semiconductors Exhibiting Structure-induced Quantum Confinement Effect and Systematically Tunable Properties*. Narlikar, A. V., Fu, Y. Y., Eds.; *Oxford Handbook of Nanoscience and Technology*; Oxford University Press: USA, 2010; Vol. 2.
169. Kagan, C. R.; Mitzi, D. B.; Dimitrakopoulos, C. D. *Science* **1999**, *286*, 945–947.
170. Mitzi, D. B.; Feild, C. A.; Harrison, W. T. A.; Guloy, A. M. *Nature* **1994**, *369*, 467–469.
171. Mitzi, D. B.; Wang, S.; Feild, C. A.; Chess, C. A.; Guloy, A. M. *Science* **1995**, *267*, 1473–1476.
172. Li, J.; Zhang, R. B. *A New Class of Nanostructured Inorganic–Organic Hybrid Semiconductors Based on II–VI Binary Compounds*. Karlin, K. D., Ed.; John Wiley & Sons: New York, 2010.
173. Kojima, N.; Okubo, M.; Shimizu, H.; Enomoto, M. *Coord. Chem. Rev.* **2007**, *251*, 2665–2673.
174. Kundys, B.; Lappas, A.; Viret, M.; Kapustianyk, V.; Rudyk, V.; Semak, S.; Simon, C.; Bakaimi, I. *Phys. Rev. B* **2010**, *81*, 224434.
175. Kitazawa, N.; Aono, M.; Watanabe, Y. *Thin Solid Films* **2010**, *518*, 3199–3203.
176. Gauthron, K.; Lauret, J. S.; Doyennette, L.; Lanty, G.; Al Choueiry, A.; Zhang, S. J.; Brehier, A.; Largeau, L.; Mauguin, O.; Bloch, J.; Deleporte, E. *Opt. Express* **2010**, *18*, 5912–5919.
177. Lemmerer, A.; Billing, D. G. *CrystEngComm* **2010**, *12*, 1290–1301.
178. Sanchez-Andujar, M.; Presedo, S.; Yanez-Vilar, S.; Castro-Garcia, S.; Shamir, J.; Senaris-Rodriguez, M. A. *Inorg. Chem.* **2010**, *49*, 1510–1516.
179. Jain, P.; Dalal, N. S.; Toby, B. H.; Kroto, H. W.; Cheetham, A. K. *J. Am. Chem. Soc.* **2008**, *130*, 10450–10451.
180. Zhang, S. J.; Lanty, G.; Lauret, J. S.; Deleporte, E.; Audebert, P.; Galmiche, L. *Acta Mater.* **2009**, *57*, 3301–3309.
181. Huang, G.; Sun, Y. Q.; Xu, Z. T.; Zeller, M.; Hunter, A. D. *Dalton Trans.* **2009**, 5083–5093.
182. Guloy, A. M.; Tang, Z. J.; Miranda, P. B.; Srdanov, V. I. *Adv. Mater.* **2001**, *13*, 833–837.
183. Lu, C. Z.; Wu, C. D.; Lu, S. F.; Liu, J. C.; Wu, Q. J.; Zhuang, H. H.; Huang, J. S. *Chem. Commun.* **2002**, 152–153.
184. Mercier, N.; Poiroux, S.; Riou, A.; Batail, P. *Inorg. Chem.* **2004**, *43*, 8361–8366.
185. Mitzi, D. B. *J. Chem. Soc. Dalton* **2001**, 1–12.
186. Mitzi, D. B. *J. Mater. Chem.* **2004**, *14*, 2355–2365.
187. Shi, Y. J.; Xu, Y.; Zhang, Y.; Huang, B.; Zhu, D. R.; Jin, C. M.; Zhu, H. G.; Yu, Z.; Chen, X. T.; You, X. Z. *Chem. Lett.* **2001**, 678–679.
188. Mercier, N.; Riou, A. *Chem. Commun.* **2004**, 844–845.
189. Sourisseau, S.; Louvain, N.; Bi, W. H.; Mercier, N.; Rondeau, D.; Boucher, F.; Buzare, J. Y.; Legein, C. *Chem. Mater.* **2007**, *19*, 600–607.
190. Pradeesh, K.; Baumberg, J. J.; Prakash, G. V. *Appl. Phys. Lett.* **2009**, *95*, 033309.
191. Ema, K.; Inomata, M.; Kato, Y.; Kunugita, H. *Phys. Rev. Lett.* **2008**, *100*, 257401.
192. Dammak, T.; Fourati, N.; Boughzala, H.; Mlayah, A.; Abid, Y. *J. Lumin.* **2007**, *127*, 404–408.
193. Eustis, S.; El-Sayed, M. A. *Chem. Soc. Rev.* **2006**, *35*, 209–217.
194. Kongkanand, A.; Tvrdy, K.; Takechi, K.; Kuno, M.; Kamat, P. V. *J. Am. Chem. Soc.* **2008**, *130*, 4007–4015.
195. Park, J.; Joo, J.; Kwon, S. G.; Jang, Y.; Hyeon, T. *Angew. Chem. Int. Ed.* **2007**, *46*, 4630–4660.
196. Kamat, P. V. *J. Phys. Chem. C* **2008**, *112*, 18737–18753.
197. Gill, R.; Zayats, M.; Willner, I. *Angew. Chem. Int. Ed.* **2008**, *47*, 7602–7625.
198. Reiss, P.; Protiere, M.; Li, L. *Small* **2009**, *5*, 154–168.
199. Huang, X. Y.; Li, J.; Fu, H. X. *J. Am. Chem. Soc.* **2000**, *122*, 8789–8790.
200. Heulings, H. R.; Huang, X. Y.; Li, J.; Yuen, T.; Lin, C. L. *Nano Lett.* **2001**, *1*, 521–525.
201. Huang, X. Y.; Heulings, H. R.; Le, V.; Li, J. *Chem. Mater.* **2001**, *13*, 3754–3759.
202. Huang, X. Y.; Li, J. *Mater. Res. Soc. Symp. Proc.* **2002**, *728*, S1.7.1–S1.7.6.
203. Huang, X. Y.; Li, J. *J. Am. Chem. Soc.* **2007**, *129*, 3157–3162.
204. Huang, X. Y.; Li, J.; Zhang, Y.; Mascarenhas, A. *J. Am. Chem. Soc.* **2003**, *125*, 7049–7055.
205. Li, J.; Bi, W. H.; Ki, W.; Huang, X. Y.; Reddy, S. *J. Am. Chem. Soc.* **2007**, *129*, 14140–14141.
206. Huang, X. Y.; Roushan, M.; Emge, T. J.; Bi, W. H.; Thiagarajan, S.; Cheng, J. H.; Yang, R. G.; Li, J. *Angew. Chem. Int. Ed.* **2009**, *48*, 7871–7874.
207. Hsiao, H. L.; Yang, A. B.; Hwang, H. L. *J. Phys. Chem. Solids* **2008**, *69*, 278–283.
208. Deng, Z. T.; Schulz, O.; Lin, S.; Ding, B. Q.; Liu, X. W.; Wei, X. X.; Ros, R.; Yan, H.; Liu, Y. *J. Am. Chem. Soc.* **2010**, *132*, 5592–5593.
209. Riehle, F. S.; Bienert, R.; Thomann, R.; Urban, G. A.; Krugert, M. *Nano Lett.* **2009**, *9*, 514–518.
210. Evans, C. M.; Guo, L.; Peterson, J. J.; Maccagnano-Zacher, S.; Krauss, T. D. *Nano Lett.* **2008**, *8*, 2896–2899.
211. Neeraj, R. C. N. R. *J. Mater. Chem.* **1998**, *8*, 279–280.
212. Li, J.; Chen, Z.; Wang, R. J.; Proserpio, D. M. *Coord. Chem. Rev.* **1999**, *192*, 707–735.
213. Rabenau, A. *Angew. Chem. Int. Ed.* **1985**, *24*, 1026–1040.
214. Barrer, R. M. *Hydrothermal Chemistry of Zeolites*. Academic Press: London, 1982.
215. Laudise, R. A. *Progress in Inorganic Chemistry* Interscience: New York, 1962; vol. III.
216. Farha, O. K.; Hupp, J. T. *Acc. Chem. Res.* **2010**, *43*, 1166–1175.
217. Zhou, J.; Dai, J.; Bian, G. Q.; Li, C. Y. *Coord. Chem. Rev.* **2009**, *253*, 1221–1247.
218. Chen, X. M.; Tong, M. L. *Acc. Chem. Res.* **2007**, *40*, 162–170.
219. Michailovski, A.; Patzke, G. R. *Chem. Eur. J.* **2006**, *12*, 9122–9134.
220. Walton, R. I. *Chem. Soc. Rev.* **2002**, *31*, 230–238.

221. Kumar, S.; Nann, T. *Small* **2006**, *2*, 316–329.
222. Patzke, G. R.; Krumeich, F.; Nesper, R. *Angew. Chem. Int. Ed.* **2002**, *41*, 2446–2461.
223. Su, C. Y.; Goforth, A. M.; Smith, M. D.; Pellechia, P. J.; zur Loye, H. C. *J. Am. Chem. Soc.* **2004**, *126*, 3576–3586.
224. Tian, B. Z.; Liu, X. Y.; Solovyov, L. A.; Liu, Z.; Yang, H. F.; Zhang, Z. D.; Xie, S. H.; Zhang, F. Q.; Tu, B.; Yu, C. Z.; Terasaki, O.; Zhao, D. Y. *J. Am. Chem. Soc.* **2004**, *126*, 865–875.
225. Laye, R. H.; McInnes, E. J. L. *Eur. J. Inorg. Chem.* **2004**, 2811–2818.
226. Yao, W. T.; Yu, S. H. *Adv. Funct. Mater.* **2008**, *18*, 3357–3366.
227. Rao, C. N. R.; Govindaraj, A. *Adv. Mater.* **2009**, *21*, 4208–4233.
228. Yang, J.; Xue, C.; Yu, S. H.; Zeng, J. H.; Qian, Y. T. *Angew. Chem. Int. Ed.* **2002**, *41*, 4697–4700.
229. Yu, S. H.; Yoshimura, M. *Adv. Mater.* **2002**, *14*, 296–300.
230. Li, Y. D.; Liao, H. W.; Ding, Y.; Fan, Y.; Zhang, Y.; Qian, Y. T. *Inorg. Chem.* **1999**, *38*, 1382–1387.
231. Xie, Y.; Qian, Y. T.; Wang, W. Z.; Zhang, S. Y.; Zhang, Y. H. *Science* **1996**, *272*, 1926–1927.
232. Sardar, K.; Dan, M.; Schwenzer, B.; Rao, C. N. R. *J. Mater. Chem.* **2005**, *15*, 2175–2177.
233. Wang, B. G.; Callahan, M. J. *Cryst. Growth Des.* **2006**, *6*, 1227–1246.
234. Demazeau, G. *J. Mater. Sci.* **2008**, *43*, 2104–2114.
235. Brock, S. L.; Perera, S. C.; Stamm, K. L. *Chem. Eur. J.* **2004**, *10*, 3364–3371.
236. Qian, Y. T. *Adv. Mater.* **1999**, *11*, 1101–1102.
237. Cheetham, A. K.; Rao, C. N. R.; Feller, R. K. *Chem. Commun.* **2006**, 4780–4795.
238. Parnham, E. R.; Morris, R. E. *Acc. Chem. Res.* **2007**, *40*, 1005–1013.
239. Murugavel, R.; Walawalkar, M. G.; Dan, M.; Roesky, H. W.; Rao, C. N. R. *Acc. Chem. Res.* **2004**, *37*, 763–774.
240. Mao, J. G. *Coord. Chem. Rev.* **2007**, *251*, 1493–1520.
241. Zhao, J. W.; Jia, H. P.; Zhang, J.; Zheng, S. T.; Yang, G. Y. *Chem. Eur. J.* **2007**, *13*, 10030–10045.
242. Rao, C. N. R.; Behera, J. N.; Dan, M. *Chem. Soc. Rev.* **2006**, *35*, 375–387.
243. Matczak-Jon, E.; Videnova-Adrabinska, V. *Coord. Chem. Rev.* **2005**, *249*, 2458–2488.
244. Demazeau, G. *J. Mater. Chem.* **1999**, *9*, 15–18.
245. Morris, R. E.; Weigel, S. J. *Chem. Soc. Rev.* **1997**, *26*, 309–317.
246. Tarascon, J. M.; Recham, N.; Armand, M.; Chotard, J. N.; Barpanda, P.; Walker, W.; Dupont, L. *Chem. Mater.* **2010**, *22*, 724–739.
247. Lu, J. Y. *Coord. Chem. Rev.* **2003**, *246*, 327–347.
248. Lei, S. J.; Tang, K. B.; Yang, Q.; Zheng, H. G. *Eur. J. Inorg. Chem.* **2005**, 4124–4128.
249. Hosokawa, S.; Jeon, H. J.; Iwamoto, S.; Inoue, M. *J. Am. Ceram. Soc.* **2009**, *92*, 2847–2853.
250. Corr, S. A.; Grossman, M.; Shi, Y. F.; Heier, K. R.; Stucky, G. D.; Seshadri, R. *J. Mater. Chem.* **2009**, *19*, 4362–4367.
251. Feng, S. H.; Xu, R. R. *Acc. Chem. Res.* **2001**, *34*, 239–247.
252. Sheldrick, W. S.; Wachhold, M. *Angew. Chem. Int. Ed.* **1997**, *36*, 207–224.
253. Stein, A.; Keller, S. W.; Mallouk, T. E. *Science* **1993**, *259*, 1558–1564.
254. Shimizu, G. K. H.; Vaidhyanathan, R.; Taylor, J. M. *Chem. Soc. Rev.* **2009**, *38*, 1430–1449.
255. Feng, W.; Sun, L. D.; Zhang, Y. W.; Yan, C. H. *Coord. Chem. Rev.* **2010**, *254*, 1038–1053.
256. Suh, M. P.; Cheon, Y. E.; Lee, E. Y. *Coord. Chem. Rev.* **2008**, *252*, 1007–1026.
257. Zhao, Y. G.; Li, K. H.; Li, J. *Z. Naturforsch. B* **2010**, *65*, 976–998.
258. Laudise, R. A. *Chem. Eng. News* **1987**, *65*, 30–43.
259. Fan, L. B.; Song, H. W.; Zhao, H. F.; Pan, G. H.; Liu, L.; Dong, B.; Wang, F.; Bai, X.; Qin, R. F.; Kong, X. G.; Ren, X. G. *J. Nanosci. Nanotechnol.* **2008**, *8*, 3914–3920.
260. Fan, L. B.; Song, H. W.; Zhao, H. F.; Pan, G. H.; Yu, H. Q.; Bai, X.; Li, S. W.; Lei, Y. Q.; Dai, Q. L.; Qin, R. F.; Wang, T.; Dong, B.; Zheng, Z. H.; Ren, X. G. *J. Phys. Chem. B* **2006**, *110*, 12948–12953.
261. Gawel, B.; Lasocha, W.; Zieba, M. *J. Alloys Compd.* **2007**, *442*, 77–79.
262. Jang, J. W.; Choi, S. H.; Jang, J. S.; Lee, J. S.; Cho, S.; Lee, K. H. *J. Phys. Chem. C* **2009**, *113*, 20445–20451.
263. http://www.alfa.com, http://www.acros.com, www.sigmaaldrich.com.
264. Ouyang, X.; Tsai, T. Y.; Chen, D. H.; Huang, Q. J.; Cheng, W. H.; Clearfield, A. *Chem. Commun.* **2003**, 886–887.
265. Deng, Z. X.; Li, L. B.; Li, Y. D. *Inorg. Chem.* **2003**, *42*, 2331–2341.
266. Lu, J.; Wei, S.; Yu, W. C.; Zhang, H. B.; Qian, Y. T. *Chem. Mater.* **2005**, *17*, 1698–1703.
267. Mitzi, D. B. *Inorg. Chem.* **2005**, *44*, 7078–7086.
268. Rebilly, J. N.; Gardner, P. W.; Darling, G. R.; Bacsa, J.; Rosseinsky, M. J. *Inorg. Chem.* **2008**, *47*, 9390–9399.
269. Milman, V.; Winkler, B.; White, J. A.; Pickard, C. J.; Payne, M. C.; Akhmatskaya, E. V.; Nobes, R. H. *Int. J. Quantum Chem.* **2000**, *77*, 895–910.
270. Segall, M. D.; Lindan, P. J. D.; Probert, M. J.; Pickard, C. J.; Hasnip, P. J.; Clark, S. J.; Payne, M. C. *J. Phys.: Condens. Matter* **2002**, *14*, 2717–2744.
271. Clark, S. J.; Segall, M. D.; Pickard, C. J.; Hasnip, P. J.; Probert, M. J.; Refson, K.; Payne, M. C. *Z. Kristallogr.* **2005**, *220*, 567–570.
272. Perdew, J. P.; Burke, K.; Ernzerhof, M. *Phys. Rev. Lett.* **1996**, *77*, 3865–3868.
273. Kresse, G.; Joubert, D. *Phys. Rev. B* **1999**, *59*, 1758–1775.
274. Godby, R. W.; Schluter, M.; Sham, L. J. *Phys. Rev. B* **1988**, *37*, 10159–10175.
275. Jones, R. O.; Gunnarsson, O. *Rev. Mod. Phys.* **1989**, *61*, 689–746.
276. Godby, R. W.; Schluter, M.; Sham, L. J. *Phys. Rev. B* **1987**, *36*, 6497–6500.
277. Fu, H. X.; Li, J. *J. Chem. Phys.* **2004**, *120*, 6721–6725.
278. Zhang, Y.; Dalpian, G. M.; Fluegel, B.; Wei, S. H.; Mascarenhas, A.; Huang, X. Y.; Li, J.; Wang, L. W. *Phys. Rev. Lett.* **2006**, *96*, 026405.
279. Evans, J. S. O.; Hu, Z.; Jorgensen, J. D.; Argyriou, D. N.; Short, S.; Sleight, A. W. *Science* **1997**, *275*, 61–65.
280. Margadonna, S.; Prassides, K.; Fitch, A. N. *J. Am. Chem. Soc.* **2004**, *126*, 15390–15391.
281. Roy, R.; Agrawal, D. K.; Mckinstry, H. A. *Annu. Rev. Mater. Sci.* **1989**, *19*, 59–81.
282. Salvador, J. R.; Gu, F.; Hogan, T.; Kanatzidis, M. G. *Nature* **2003**, *425*, 702–705.
283. Sleight, A. *Nature* **2003**, *425*, 674–676.
284. Mary, T. A.; Evans, J. S. O.; Vogt, T.; Sleight, A. W. *Science* **1996**, *272*, 90–92.
285. Evans, J. S. O.; Hanson, P. A.; Ibberson, R. M.; Duan, N.; Kameswari, U.; Sleight, A. W. *J. Am. Chem. Soc.* **2000**, *122*, 8694–8699.
286. Villaescusa, L. A.; Lightfoot, P.; Teat, S. J.; Morris, R. E. *J. Am. Chem. Soc.* **2001**, *123*, 5453–5459.
287. Barrera, G. D.; Bruno, J. A. O.; Barron, T. H. K.; Allan, N. L. *J. Phys.: Condens. Matter* **2005**, *17*, R217–R252.
288. Babu, A. M.; Weakley, T. J. R.; Murthy, M. R. N. *Z. Krist-New Cryst. Struct.* **1998**, *213*, 321–322.
289. Vaidhyanathan, R.; Natarajan, S.; Rao, C. N. R. *J. Mol. Struct.* **2002**, *608*, 123–133.
290. Zhang, Y.; Islam, Z.; Ren, Y.; Parilla, P. A.; Ahrenkiel, S. P.; Lee, P. L.; Mascarenhas, A.; McNevin, M. J.; Naumov, I.; Fu, H. X.; Huang, X. Y.; Li, J. *Phys. Rev. Lett.* **2007**, *99*, 215901.
291. Hancock, J. N.; Turpen, C.; Schlesinger, Z.; Kowach, G. R.; Ramirez, A. P. *Phys. Rev. Lett.* **2004**, *93*, 225501.
292. Chapman, K. W.; Hagen, M.; Kepert, C. J.; Manuel, P. *Phys. B: Condens. Matter.* **2006**, *385*, 60–62.
293. Bergh, A.; Craford, G.; Duggal, A.; Haitz, R. *Phys. Today* **2001**, *54*, 42–47.
294. Uchida, Y.; Taguchi, T. *Opt. Eng.* **2005**, *44*, 124003.
295. Wu, H. B.; Ying, L.; Yang, W.; Cao, Y. *Chem. Soc. Rev.* **2009**, *38*, 3391–3400.
296. Mueller, A. H.; Petruska, M. A.; Achermann, M.; Werder, D. J.; Akhadov, E. A.; Koleske, D. D.; Hoffbauer, M. A.; Klimov, V. I. *Nano Lett.* **2005**, *5*, 1039–1044.
297. Yang, W. J.; Luo, L. Y.; Chen, T. M.; Wang, N. S. *Chem. Mater.* **2005**, *17*, 3883–3888.
298. Ki, W.; Li, J. *J. Am. Chem. Soc.* **2008**, *130*, 8114–8115.
299. Ki, W.; Li, J.; Eda, G.; Chhowalla, M. *J. Mater. Chem.* **2010**, *20*, 10676–10679.
300. Nag, A.; Sarma, D. D. *J. Phys. Chem. C* **2007**, *111*, 13641–13644.
301. Norris, D. J.; Yao, N.; Charnock, F. T.; Kennedy, T. A. *Nano Lett.* **2001**, *1*, 3–7.
302. CIE. *Commission Internationale de l'Eclairage Proceedings*. Cambridge University Press: Cambridge, 1931.
303. Roushan, M.; Zhang, X.; Li, *J. Angew. Chem. Int. Ed.* **2012**, *51*, 436–439.
304. Underwood, D. F.; Kippeny, T.; Rosenthal, S. J. *J. Phys. Chem. B* **2001**, *105*, 436–443.
305. Huang, X. Y.; Heulings, H. R.; Li, J.; Yuen, T.; Lin, C. L. *J. Nanosci. Nanotechnol.* **2005**, *5*, 1487–1491.
306. Jang, J. S.; Choi, S. H.; Kim, E. S.; Lee, J. S.; Shin, N.; Lee, D. R. *Chem. Phys. Lett.* **2009**, *468*, 253–256.
307. Zhang, M.; Shi, C.; Zhang, T.-K.; Feng, M.; Chang, L.; Yao, W.-T.; Yu, S.-H. *Chem. Mater.* **2009**, *21*, 5485–5490.
308. Li, J.; Huang, X. Y.; Yuen, T. *Towards Dilute Magnetic Semiconductors: Doped Inorganic–Organic Hybrid Nanostructured Materials Based on II–VI Semiconductors. In Doped Nanomaterials and Nanodevices*; American Scientific Publishers: Stevenson Ranch, CA, 2008.
309. Yao, W. T.; Yu, S. H.; Wu, Q. S. *Adv. Funct. Mater.* **2007**, *17*, 623–631.
310. Lu, F.; Cai, W. P.; Zhang, Y. G.; Li, Y.; Sun, F. Q.; Heo, S. H.; Cho, S. O. *Appl. Phys. Lett.* **2006**, *89*, 231928.
311. Li, L. B.; Li, Y. D. *Mater. Chem. Phys.* **2005**, *94*, 1–6.
312. Chen, X. J.; Xu, H. F.; Xu, N. S.; Zhao, F. H.; Lin, W. J.; Lin, G.; Fu, Y. L.; Huang, Z. L.; Wang, H. Z.; Wu, M. M. *Inorg. Chem.* **2003**, *42*, 3100–3106.
313. Zhou, G. T.; Wang, X. C.; Yu, J. C. *Cryst. Growth Des.* **2005**, *5*, 1761–1765.
314. Yao, W. T.; Yu, S. H.; Jiang, J.; Zhang, L. *Chem. Eur. J.* **2006**, *12*, 2066–2072.

315. Yao, W. T.; Yu, S. H.; Liu, S. J.; Chen, J. P.; Liu, X. M.; Li, F. Q. *J. Phys. Chem. B* **2006**, *110*, 11704–11710.
316. Yao, H. B.; Li, X. B.; Yu, S. H. *Chem. Eur. J.* **2009**, *15*, 7611–7618.
317. Liu, L. N.; Song, H. W.; Fan, L. B.; Wang, F.; Qin, R. F.; Dong, B. A.; Zhao, H. F.; Ren, X. G.; Pan, G. H.; Bai, X.; Dai, Q. L. *Mater. Res. Bull* **2009**, *44*, 1385–1391.
318. Yao, H. B.; Zhang, X. A.; Wang, X. H.; Yu, S. H.; Li, J. *Dalton Trans.* **2011**, *40*, 3191–3197.
319. Yu, S. H.; Yang, J.; Qian, Y. T.; Yoshimura, M. *Chem. Phys. Lett.* **2002**, *361*, 362–366.
320. Dong, Y. J.; Peng, Q.; Li, Y. D. *Inorg. Chem. Commun.* **2004**, *7*, 370–373.
321. Cerveau, G.; Corriu, R. J. P.; Framery, E. *Chem. Mater.* **2001**, *13*, 3373–3388.
322. Pellegrino, T.; Kudera, S.; Liedl, T.; Javier, A. M.; Manna, L.; Parak, W. J. *Small* **2005**, *1*, 48–63.
323. Yao, W. T.; Yu, S. H.; Pan, L.; Li, J.; Wu, Q. S.; Zhang, L.; Jiang, H. *Small* **2005**, *1*, 320–325.
324. Yao, W. T.; Yu, S. H.; Huang, X. Y.; Jiang, J.; Zhao, L. Q.; Pan, L.; Li, J. *Adv. Mater.* **2005**, *17*, 2799–2802.
325. Mitzi, D. B. *Adv. Mater.* **2009**, *21*, 3141–3158.
326. Todorov, T. K.; Reuter, K. B.; Mitzi, D. B. *Adv. Mater.* **2010**, *22*, E156–E159.
327. Dai, J.; Jiang, Z. J.; Li, W. G.; Bian, G. Q.; Zhu, Q. Y. *Mater. Lett.* **2002**, *55*, 383–387.
328. Nazzal, A.; Fu, H. X. *Phys. Rev. B* **2005**, *72*, 075202.
329. Moon, C. Y.; Dalpian, G. M.; Zhang, Y.; Wei, S. H. *Chem. Mater.* **2006**, *18*, 2805–2809.
330. Fluegel, B.; Zhang, Y.; Mascarenhas, A.; Huang, X.; Li, J. *Phys. Rev. B* **2004**, *70*, 205308.
331. Zhang, R.; Emge, T. J.; Zheng, C.; Li, J. *J. Mater. Chem.* submitted for publication.
332. Li, K. H.; Xu, Z. T.; Xu, H. H.; Ryan, J. M. *Chem. Mater.* **2005**, *17*, 4426–4437.
333. Li, K. H.; Xu, H. H.; Xu, Z. T.; Zeller, M.; Hunter, A. D. *Inorg. Chem.* **2005**, *44*, 8855–8860.
334. Neofotistou, E.; Malliakas, C. D.; Trikalitis, P. N. *Inorg. Chem.* **2007**, *46*, 8487–8489.
335. Kapre, R. R.; Bothe, E.; Weyhermuller, T.; George, S. D.; Wieghardt, K. *Inorg. Chem.* **2007**, *46*, 5642–5650.
336. Su, W. P.; Hong, M. C.; Weng, J. B.; Cao, R.; Lu, S. F. *Angew. Chem. Int. Ed.* **2000**, *39*, 2911–2914.
337. Zhao, Y. J.; Hong, M. C.; Liang, Y. C.; Cao, R.; Li, W. J.; Weng, J. B.; Lu, S. F. *Chem. Commun.* **2001**, 1020–1021.
338. Turner, D. L.; Vaid, T. P.; Stephens, P. W.; Stone, K. H.; DiPasquale, A. G.; Rheingold, A. L. *J. Am. Chem. Soc.* **2008**, *130*, 14–15.
339. Walsh, A. *J. Phys. Chem. Lett.* **2010**, *1*, 1284–1287.
340. Chen, Z.; Dilks, R. E.; Wang, R. J.; Lu, J. Y.; Li, J. *Chem. Mater.* **1998**, *10*, 3184–3188.
341. Chen, Y.C.; Yao, H. B.; Thiagarajan, S.; Wu, M.; Emge, T.J.; Yang, R.G.; Yu, S.H.; Li, J. Z. *Anorg. Allg: Chem*, 2012.
342. Powell, A. V.; Boissiere, S.; Chippindale, A. M. *J. Chem. Soc. Dalton* **2000**, 4192–4195.
343. Bensch, W.; Schur, M. *Eur. J. Solid State Inorg. Chem.* **1996**, *33*, 1149–1160.
344. Bensch, W.; Schur, M. *Z. Naturforsch. B* **1997**, *52*, 405–409.
345. Engelke, L.; Stahler, R.; Schur, M.; Nather, C.; Bensch, W.; Pottgen, R.; Moller, M. H. *Z. Naturforsch. B* **2004**, *59*, 869–876.
346. Schur, M.; Bensch, W. *Z. Naturforsch. B* **2002**, *57*, 1–7.
347. Schur, M.; Nather, C.; Bensch, W. *Z. Naturforsch. B* **2001**, *56*, 79–84.
348. Puls, A.; Nather, C.; Bensch, W. *Z. Anorg. Allg. Chem.* **2006**, *632*, 1239–1243.
349. Engelke, L.; Schaefer, M.; Porsch, F.; Bensch, W. *Eur. J. Inorg. Chem.* **2003**, 506–513.
350. Engelke, L.; Schaefer, M.; Schur, M.; Bensch, W. *Chem. Mater.* **2001**, *13*, 1383–1390.
351. Wang, X.; Sheng, T. L.; Hu, S. M.; Fu, R. B.; Wu, X. T. *Inorg. Chem. Commun.* **2009**, *12*, 399–401.
352. Liu, Y.; Kanhere, P. D.; Wong, C. L.; Tian, Y. F.; Feng, Y. H.; Boey, F.; Wu, T.; Chen, H. Y.; White, T. J.; Chen, Z.; Zhang, Q. C. *J. Solid State Chem.* **2010**, *183*, 2644–2649.
353. Rejai, Z.; Luhmann, H.; Nather, C.; Kremer, R. K.; Bensch, W. *Inorg. Chem.* **2010**, *49*, 1651–1657.
354. Manolis, M. J.; Kanatzidis, M. G. *Inorg. Chem.* **2009**, *48*, 4658–4660.
355. Yuan, M.; Dirmyer, M.; Badding, J.; Sen, A.; Dahlberg, M.; Schiffer, P. *Inorg. Chem.* **2007**, *46*, 7238–7240.
356. Partik, M.; Stingl, T.; Lutz, H. D.; Sabrowsky, H.; Vogt, P. *Z. Anorg. Allg. Chem.* **1995**, *621*, 1600–1604.
357. Hagrman, P. J.; LaDuca, R. L.; Koo, H. J.; Rarig, R.; Haushalter, R. C.; Whangbo, M. H.; Zubieta, J. *Inorg. Chem.* **2000**, *39*, 4311–4317.
358. Xu, Y.; Lu, J. J.; Goh, N. K. *J. Mater. Chem.* **1999**, *9*, 1599–1602.
359. Yan, B. B.; Xu, Y.; Goh, N. K.; Chia, L. S. *Chem. Commun.* **2000**, 2169–2170.
360. Zapf, P. J.; Haushalter, R. C.; Zubieta, J. *Chem. Mater.* **1997**, *9*, 2019–2024.
361. Hu, X. L.; Ji, Q. M.; Hill, J. P.; Ariga, K. *CrystEngComm* **2011**, *13*, 2237–2241.

This page intentionally left blank